Univerzita Karlova v Praze
Matematicko-fyzikální fakulta

DIPLOMOVÁ PRÁCE

Vojtěch Sidorin

Infračervené, optické a rentgenovské protějšky H I obálek v Mléčné dráze

Astronomický ústav Univerzity Karlovy v Praze

Vedoucí diplomové práce: **Prof. RNDr. Jan Palouš, DrSc.**
Konzultant: **RNDr. Soňa Ehlerová, PhD**

Studijní program: **Fyzika**
Studijní obor: **astronomie a astrofyzika**

Charles University in Prague
Faculty of Mathematics and Physics

DIPLOMA THESIS

Vojtěch Sidorin

IR, optical and X-ray counterparts of H I shells in the Milky Way

Astronomical Institute of the Charles University in Prague

Supervisor: **Prof. RNDr. Jan Palouš, DrSc.**
Consultant: **RNDr. Soňa Ehlerová, PhD**

Study program: **Physics**
Branch of study: **Astronomy and Astrophysics**

Rád bych poděkoval *Janu Paloušovi* za poskytnutí prostředků k práci, za návrhy, jakým směrem se ve výzkumu ubírat a za podnětnou kritiku mé práce. Také bych rád poděkoval *Soně Ehlerové* za poskytnutá data. Poděkování patří také *Lise Deharveng*, *Annie Zavagno* a *Mélanie Pomarès* z institutu *Le Laboratoire d'Astrophysique de Marseille* za předání bohatých zkušeností s mezihvězdnou hmotou a za lekce v užívání softwaru pro analýzu dat. Velice děkuji *Jimovi Daleovi* za pročištění mého anglického textu i za poznámky k jeho obsahu.

I would like to thank to *Jan Palouš* for providing me the resources for my work, for supplying me with suggestions in which way should I aim my research and for constructive criticism. I would also like to thank to *Soňa Ehlerová* for supplying me the data. Acknowledgement also belongs to *Lise Deharveng*, *Annie Zavagno* and *Mélanie Pomarès* from *Le Laboratoire d'Astrophysique de Marseille* for offering me their rich experiences with interstellar medium and for teaching me how to use software for data analysis. I would like to thank to *Jim Dale* for clarifying my english text and for valuable remarks to its contents.

Prohlašuji, že jsem svou diplomovou práci napsal samostatně a výhradně s použitím citovaných pramenů. Souhlasím se zapůjčováním práce.

I hereby declare that I have written this diploma thesis on my own, just with the cited resources. I agree with borrowing of this work.

V Praze dne In Prague	*Vojtěch Sidorin*

Contents

Název práce: *Infračervené, optické a rentgenovské protějšky H* I *obálek v Mléčné dráze*
Autor: *Vojtěch Sidorin* (*vojtech.sidorin@gmail.com*)
Katedra (ústav): *Astronomický ústav Univerzity Karlovy v Praze*
Vedoucí diplomové práce: *Prof. RNDr. Jan Palouš, DrSc.* (*palous@ig.cas.cz*),
Astronomický ústav AV ČR, v. v. i.
Datum poslední úpravy práce: *14.4.2008*

Abstrakt. **Kontext.** H I obálky jsou expandující struktury pozorované v mezihvězdném neutrálním vodíku. Nejvíce jich je známo v Mléčné dráze; pozorují se však i v jiných galaxiích. Přestože byly objeveny již na počátku druhé poloviny dvacátého století, jejich vztah k jednotlivým fázím mezihvězdné hmoty není stále plně pochopen. **Cíl.** U vybraných H I obálek identifikovat protějšky a diskutovat jejich vzájemný vztah; zvláště možnost hvězdné tvorby indukované obálkami. **Metody.** (1) Rozbor snímků H I obálek v různých oborech vlnových délek. (2) Sdružení odpovídajících si objektů z katalogu H I obálek a z katalogu infračervených smyček. (3) Hledání mladých hvězdných objektů v blízkosti H I obálek pomocí databáze SIMBAD. **Výsledky.** Z 628 katalogizovaných H I obálek má 52 potencionální protějšky v katalogu infračervených smyček. Podrobnější studium dvanácti H I obálek ukázalo, že (i) emise prachu v jejich blízkosti je rozložena velmi podobně jako emise neutrálního vodíku, (ii) H II oblasti se vyskytují zpravidla mimo H I obálky či zdánlivě v jejich stěnách, (iii) molekulární vodík se vyskytuje zpravidla ve fragmentech v okolí H I obálek nebo zdánlivě v jejich stěnách. Studium také potvrdilo, že emise horkého plynu v rentgenovém oboru je záporně korelována s emisí prachu a neutrálního vodíku. **Interpretace.** Výsledky podporují teorii hvězdné tvorby spuštěné expandujícími H I obálkami.

Klíčová slova. ISM: struktura—hvězdy: tvorba—ISM: HI obálky—ISM: IR smyčky

Title: *IR, optical and X-ray counterparts of H* I *shells in the Milky Way*
Author: *Vojtěch Sidorin* (*vojtech.sidorin@gmail.com*)
Department: *Astronomical Institute of the Charles University in Prague*
Supervisor: *Prof. RNDr. Jan Palouš, DrSc.* (*palous@ig.cas.cz*),
Astronomical Institute, Academy of Sciences of the Czech Republic, v. v. i.
Date of the last edit: *April 14, 2008*

Abstract. **Context.** H I shells are expanding structures observed in the interstellar neutral hydrogen. They have been found mostly in the Milky Way, but also in several external galaxies. Although they have been observed since the second half of the twentieth century, their relation to other phases of interstellar medium is still not fully understood. **Aims.** For selected H I shells, to identify counterparts and discuss their mutual relation; especially the possibility of star formation triggered by the shells. **Methods.** (1) Analyzing multiwavelength images of H I shells. (2) Joining the corresponding catalogued H I shells with catalogued far-infrared loops. (3) Searching for young stellar objects in the SIMBAD database. **Results.** From the 628 catalogued H I shells, 52 have a potentional counterpart in the catalogue of far-infrared loops. Multiwavelength study of twelve selected H I shells has revealed that (i) the dust emission in their vicinity is distributed like the neutral hydrogen emission, (ii) H II regions are generally found outside the H I shells or apparently in their walls, (iii) molecular hydrogen is generally found in fragments in the neighbourhood of H I shells or apparently in their walls. The study has also verified that the X-ray emission from hot gas is negatively correlated with the emission from dust. **Interpretation.** The results support the theory of star formation triggered by expanding H I shells.

Keywords. ISM: structure—stars: formation—ISM: HI shells—ISM: IR loops

Chapter 1

Introduction

The Milky Way is a barred spiral galaxy containing abundance of dust and gas, a prerequisite for star formation. But even though the medium is distributed throghout the Galaxy, star formation takes place only in certain regions—in giant molecular clouds. These clouds consist of cold and dense molecular hydrogen mixed up with dust. When the density in such a cloud surpasses a critical value, the cloud begins to collapse and creates a ball of plasma—a protostar.

But observations show that molecular clouds are in a state of virial equilibrium, indicating that the spontaneous collapse itself would not keep the observed star-forming rate so high. Therefore some triggering mechanisms are needed. Often considered mechamisms are shock waves passing through these clouds. The shockwaves are generally driven by supernova explosions and stellar winds of massive stars, but they can be also created by collisions of two or more clouds, or by some other violent event appearing in the interstellar medium.

Triggered star formation on scales up to a few tens of parsecs is observed in variety of regions—for example in the Orion Molecular Cloud Complex. One of the most challenging task today is to observe a large-scale propagating star formation.

Candidate objects for regions of large-scale propagating star formation are expanding shells of neutral hydrogen—H I shells—most likely old remnants of former star formation. They are thought to trigger or at least to support star formation in their vicinity. The aim of this work is to explore the connection between observed H I shells in the Milky Way Galaxy and other constituents of interstellar medium, and to verify the theory they may support star formation.

1.1 Observation of Neutral Hydrogen

1.1.1 21 cm Emission Line

Neutral hydrogen emits due to the forbidden transition of the proton-electron spin orientation. The difference between the higher energy level—parallel spins—and the lower energy level—antiparallel spins—is 9.4×10^{-25} J or equivalently 5.9×10^{-6} eV. The jump from the higher energy level to the lower energy level generates a photon with the wavelength of 21 cm, or equivalently the frequency of 1420 MHz.

Because this transition is forbidden, its probability is very small—only 2.9×10^{-15} s^{-1}—with the mean lifetime of about 10 Myr. Thus, for observing the 21 cm line, a large amount of hydrogen atoms is needed. Also, the transition probability can be increased by collisions of hydrogen atoms. However, as these conditions are met in most parts of the Galaxy, the emission line is detected in all directions in the sky.

The first observations of the 21 cm line were made by Ewen & Purcell (1951) and by Muller & Oort (1951), who have besides used the measurements to estimate the rotational velocity of the Galaxy[1]. Many further studies have used the H I radio emission to explore the structure of the Galaxy and, probably, many will.

1.1.2 Brightness Temperature and Column Density

Note This section is mainly based on the lecture notes of de Boer (2007) and Palouš (2008).

Planck's law, describing the spectral radiance—I_ν—of a black body, is written as a function of frequency—ν—as:

$$I_\nu = \frac{2h\nu^3}{c^2} \frac{1}{\mathrm{e}^{\frac{h\nu}{kT}} - 1}, \tag{1.1}$$

where h is the Planck constant, c is the speed of light in vacuum, k is Boltzmann's constant and T is the thermodynamic temperature.

The long-wavelength approximation, called the *Rayleigh-Jeans law*, has the form:

$$I_\nu = \frac{2\nu^2}{c^2} kT. \tag{1.2}$$

Propagation of radiation through a medium that does not scatter light is described by the radiative transfer equation:

$$\frac{\mathrm{d}I_\nu}{\mathrm{d}l} = -\varkappa_\nu\, I_\nu + \varepsilon_\nu, \tag{1.3}$$

---

[1] They have derived the rotational velocity near the Sun of about 270 km/s.

where l is the travelling distance of the beam, $\varkappa_\nu$ is the absorption coefficient and ε_ν is the emission coefficient. Defining the *optical depth*—τ_ν—and the *source function*—S_ν—as

$$\tau_\nu \overset{\text{def}}{=} \int\limits_0^{l_0} \varkappa_\nu\left(l\right)\,\mathrm{d}l, \qquad S_\nu \overset{\text{def}}{=} \frac{\varepsilon_\nu}{\varkappa_\nu}, \tag{1.4}$$

we can express a general solution of the radiative transfer equation in the form

$$I_\nu = I_{\nu,0}\,\mathrm{e}^{-\tau_\nu} + S_\nu \int\limits_0^{\tau_\nu} \mathrm{e}^{-\tau'_\nu}\,\mathrm{d}\tau'_\nu, \tag{1.5}$$

where $I_{\nu,0}$ is the background emission (coming from extragalactic sources). Assuming that the source function does not depend on the optical depth—τ_ν—we get:

$$I_\nu = I_{\nu,0}\,\mathrm{e}^{-\tau_\nu} + S_\nu\left(1 - \mathrm{e}^{-\tau_\nu}\right). \tag{1.6}$$

Consider now the emission of the Galactic neutral hydrogen at the 21 cm (1420 MHz) line.

Because the background emission is much fainter than the Galactic foreground, we can neglect the first term—$I_{\nu,0}$—on the right-hand side of the equation $1.6_{(3)}$. Then we substitute the spectral radiance—I_ν—and the source function—S_ν—using the Rayleigh-Jeans law (equation $1.2_{(2)}$):

$$S_{\mathrm{H\,I}} = \frac{2\nu_{\mathrm{H\,I}}^2}{c^2} k\,T_{\mathrm{S}}, \qquad I_{\mathrm{H\,I}} = \frac{2\nu_{\mathrm{H\,I}}^2}{c^2} k\,T_{\mathrm{B}}, \tag{1.7}$$

where T_{S} is the *spin temperature* of neutral hydrogen and T_{B} is the *brightness temperature* of neutral hydrogen. The spin temperature is connected to the population of two energetic levels of neutral hydrogen through *Maxwell-Boltzmann statistics*:

$$\frac{n_{\uparrow\uparrow}}{n_{\downarrow\uparrow}} = \frac{g_{\uparrow\uparrow}}{g_{\downarrow\uparrow}} \exp\left(-\frac{h\nu_{21\,\mathrm{cm}}}{kT_{\mathrm{S}}}\right), \tag{1.8}$$

where $n_{\uparrow\uparrow}$ is the density of H I atoms in the higher energy state (parallel spins), $n_{\downarrow\uparrow}$ is the density of H I atoms in the lower energy state (antiparallel spins), $g_{\uparrow\uparrow}$ is the degeneracy of the higher energy state and $g_{\downarrow\uparrow}$ that of the lower energy state. Note that the dominant factor for the hyperfine excitation of neutral hydrogen is the pervasive cosmic background radiation field with a temperature of about 3 K.

After the substitution of equation $1.7_{(3)}$ in the radiative transfer solution (equation $1.5_{(3)}$) and changing frequency for *radial velocity*—v—we can write

$$T_{\mathrm{B}}\left(v\right) = \int\limits_0^{\tau_0(v)} T_{\mathrm{S}}\left(\tau\left(v\right)\right)\mathrm{d}\tau\left(v\right) = \int\limits_0^{l_0} T_{\mathrm{S}}\left(v,l\right)\,\varkappa\left(v,l\right)\,\mathrm{d}l. \tag{1.9}$$

Assuming that

$$\varkappa\left(v,l\right)=\text{const.}\,\frac{n\left(v,l\right)}{T_{\mathrm{S}}\left(v,l\right)},\tag{1.10}$$

where n is the particle density of neutral hydrogen atoms, we can express the brightness temperature as

$$T_{\mathrm{B}}\left(v\right)=1.69\int\limits_{0}^{l_0}n\left(v,s\right)\,\mathrm{d}s.\tag{1.11}$$

This equation connects the brightness temperature—T_{B}—to the particle density—n—for an optically thin environment ($\tau \ll 1$).

The *particle column density* of neutral hydrogen atoms—N—can be expressed as

$$N=\int\limits_{-\infty}^{+\infty}N\left(v\right)\,\mathrm{d}v=\int\limits_{-\infty}^{+\infty}\int\limits_{0}^{l_0}n\left(v,l\right)\mathrm{d}l\,\mathrm{d}v.\tag{1.12}$$

Combining the expression for brightness temperature (equation $1.11_{(4)}$) and the expression for particle column density (equation $1.12_{(4)}$), we can write

$$\boxed{N=1.823\cdot10^{18}\int\limits_{-\infty}^{+\infty}T_{\mathrm{B}}\left(v\right)\mathrm{d}v\qquad\left[\mathrm{cm}^{-2}\right]}\,.\tag{1.13}$$

This final equation allows us to determine the particle column density of neutral hydrogen atoms from measurements of the brightness temperature.

1.1.3 Radial Velocity

The change in frequency and wavelength as perceived by an observer, caused by the radial velocity of the source, valid for velocities much smaller than the speed of light is described by the *Doppler effect*:

$$\nu_{\mathrm{obs}}=\left(1-\frac{v}{c}\right)\nu_{\mathrm{em}},\qquad\lambda_{\mathrm{em}}=\left(1-\frac{v}{c}\right)\lambda_{\mathrm{obs}},\tag{1.14}$$

where ν_{obs} is the observed frequency, λ_{obs} is the observed wavelength, v is the radial velocity of the source, c is the speed of light, ν_{em} is the emission frequency in the rest frame of the source and λ_{em} is the emission wavelength in the rest frame of the source. Differentiation of the formulas gives:

$$\mathrm{d}\nu_{\mathrm{obs}}=-\frac{\mathrm{d}v}{c}\,\nu_{\mathrm{em}},\qquad\mathrm{d}\lambda_{\mathrm{obs}}\approx\frac{\mathrm{d}v}{c}\,\lambda_{\mathrm{em}},\tag{1.15}$$

what yields that for the 21 cm (1420 MHz) emission line, one velocity channel 1 km/s wide will receive wavelengths from the interval of the width of 703.8 nm, or equivalently frequencies from the interval of the width of 4.736 kHz.

For example, suppose a broad velocity channel between 200 and 400 km/s. It will receive frequencies from 1418.511 to 1419.459 MHz, or equivalently wavelengths from 211.2019 to 211.3427 mm.

1.2 H I Shells

1.2.1 Basic Properties of H I Shells

H I shells[2] are expanding structures observed in the interstellar neutral hydrogen. They have been found mainly in the Milky Way Galaxy, but also in several nearby galaxies within 10 Mpc that can be observed in sufficient spatial resolution.

H I shells in the Milky Way were discovered, for example, by Ehlerová & Palouš (2005); Daigle et al. (2003); Heiles (1984, 1979, 1976); Hu (1981); Katgert (1969); in the Magellanic Clouds by Stanimirovic et al. (1999); Thilker et al. (1998), and in other galaxies by Walter & Brinks (1999); Thilker et al. (1998).

Their basic characteristics are:

- central hole—rarified medium—surrounded by a thin dense wall,
- diameter from 10 pc up to more than 1 kpc,
- expansion velocity up to about 40 km/s,
- age of several Myr to several tens of Myr,
- and embedded energy of about 10^{50} to 10^{54} erg.

Although the shells have been observed since the second half of the twentieth century, their relation to other components of matter in galaxies (dust, gas, stars) is still not fully understood. One of the first observers, Heiles (1979), has noted that “The H I shells do not seem to be significantly correlated with any other type of astronomical objects, . . . ”. This statement was later confirmed in a more detailed study by Hu (1981).

Today, the following theories of the origin of H I shells are considered: They may have been created by energy released by

1. stellar winds of OB stars in associations and explosions of corresponding supernovae,
2. infall of high-velocity clouds into the galactic disc, or
3. events that produce gamma-ray bursts.

---

[2] The symbol for neutral hydrogen—H I—is used, traditionally, by astronomers. It symbolizes the lowest level of “ionization”—no ionization. Ionized hydrogen is then written as H II. Note that chemists would use H for neutral hydrogen and H^+ for ionized hydrogen.

An overview of these theories is presented further in this paper—section 1.2.2$_{(6)}$.

Another possibility is that they are just random fluctuations in the turbulent interstellar medium. However, this process is regarded as highly improbable since it is unlikely to produce a coherent shell expanding with velocities of tens of km/s as a random fluctuation in turbulent medium.

An open question is what is the impact of expanding H I shells on the ambient interstellar medium. The idea of induced star formation states that H I shells may trigger formation of new, often massive, stars. However, it is difficult to prove this theory by observations, but numerical simulations, like that of Ehlerová & Palouš (2002), show that H I shells may trigger star formation via fragmentation of their borders. Alternatively, the expanding shells may trigger star formation via the shock wave interacting with a preexisting molecular cloud. An overview of the impact of shells on their surroundings is presented further in this paper—section 1.2.4$_{(11)}$.

In this work, I am going to address the following questions:

1. Is it possible, with current instruments and data archives, to find counterparts of H I shells?
2. If we find some counterparts, what do they indicate about the relation of H I shells to other components of interstellar matter (stars and medium)?
3. And, are there any signs of star formation triggered by H I shells?

1.2.2 Origin of H I shells

Stellar Winds of OB Stars and Supernovae

Energetic analysis by Tenorio-Tagle & Bodenheimer (1988) has shown that the combined energy of H II regions, stellar winds and supernova remnants from OB associations can be sufficient to create an expanding shell of size up to 400 pc in radius and with embedded energy up to 10^{52} erg. The statistical analysis by Ehlerová & Palouš (1996) has shown that most observed shells with the radius up to several parsecs are probably old remnants of OB associations and their supernovae. The analysis has also determined the mean shell lifetime of 50 Myr. Assuming that OB associations live less than about 10 Myr, H I shells as their remnants can archive the history of former star formation in the Galaxy.

A more detailed study of the supershell GS061+00+51 by Ehlerová et al. (2001) has supported this theory. The study has revealed that there are small, young shells around some H II regions. These minishells represent the very early stage of shell's evolution.

Supershells with energies in the rage of 10^{53} to 10^{54} erg are probably not created only by these processes, as there is not enough massive stars present in OB associations to create such a large structure (Tenorio-Tagle & Bodenheimer, 1988). Thus, several different sources of energy are most likely acting to build up the largest shells.

Collisions of High-Velocity Clouds With the Galactic Disc

The infall of a high-velocity cloud into the Galactic disc is a phenomenon in many respects similar to the fall of a drop of water on the water surface. High-velocity clouds are clumps of interstellar medium travelling at LSR[3] velocities more than 100 km/s. When they hit the Galactic disc, their kinetic energy can be transformed into an expanding shell (like waves on the water).

High-velocity clouds were observed, for example, by Hulsbosch & Raimond (1966); Giovanelli (1980) and reviewed by Hulsbosch (1975); Verschuur (1975). Their dimensions are equal or more than 300 pc in diameter and masses from 10^4 to 10^7 $M_\odot$.

Numerical calculations of Tenorio-Tagle (1980, 1981) have shown that collisions of high-velocity clouds with the Galactic disc can create expanding structures. An observational evidence was later given by Heiles (1984). Subsequent hydrodynamical simulations by Tenorio-Tagle et al. (1986, 1987) have also shown that the released energy can be rather large—from 5×10^{51} to 3×10^{54} erg—and that the cloud-Galaxy interaction may be responsible for some of the most energetic H I supershells. These supershells would be in all cases missing some part of the remnant, creating open structures. This could be an useful characteristic indicating the origin of observed shells.

The final statement of this theory may be that the energy injected per collision of high-velocity cloud with the Galactic disc can be rather large compared to the total energy produced by an OB association.

Gamma-Ray Bursts

Gamma-ray bursts are the most intensive events observed in the universe with very short duration—only about a few seconds. The total energy of an event producing such a burst is thought to be 10^{51} erg or more (Frail et al., 2001), depending on the beaming factor. The first observations of gamma-ray bursts were published by Klebesadel et al. (1973).

In the 1990s there were two notable theories about the location of bursts. First—the Galactic hypothese—has stated that gamma-ray bursts originate in the distant Galactic corona, containing high-velocity neutron stars that have escaped from the Galaxy. These neutron stars were thought to produce the observed gamma-ray burst. The Galactic theory was supported, for example, by Lamb (1995).

Second theory—the extragalactic hypothese—has stated that gamma-ray bursts originate in cosmological distances. This theory was supported, for example, by Paczynski (1995). Further study by Waxman (1997) has also supported this theory. The study was based upon the observations of gamma-ray bursts afterglows and revealed that bursts originate in densities typical for galactic interstellar medium (≈ 1 cm^{-3}).

Finally, the extragalactic hypothese was confirmed by observation of the burst GRB 050904 with high redshift published by Haislip et al. (2006).

The theory that H I shells may be remnants of gamma-ray bursts explosions were studied

---

[3] LSR = **L**ocal **S**tandard of **R**est

by (Efremov et al., 1998; Loeb & Perna, 1998). It was shown that gamma-ray bursts may create a supershell with the radius larger than ≈ 1 kpc. The total kinetic energy injected into the surrounding medium was assumed to be more than $\approx 10^{52}$ erg.

1.2.3 Evolution of H I Shells

Numerical simulations by Efremov et al. (1999) show that not only the total energy injected into the interstellar medium but also the continuity of energy input determine the sheel radius and expansion velocity. Figure **1.1**$_{(9)}$ shows results of simulations for shells expanding in a homogenous medium with density of 1.4 cm^{-3} and with either continuous or abrupt energy input of 10^{52}, 10^{53} and 10^{54} erg. The abrupt energy input may represents a gamma-ray burst event or single supernova explosion, while the continuous energy input represents the energy released by an OB association.

The most distinct results are that shells driven by an gamma-ray burst event would reach lower expansion velocities and smaller radii that shells driven by an OB association. This is a result of processes of energy transformation. Shells with continuous energy input will finally transform more available energy into their kinetic energy, thus creating a larger remnants expanding with higher velocities.

This conclusion confirms preceeding hydrodynamical simulations by Bodenheimer et al. (1984) that has shown that two spatially close supernovae exploding successively at different times will create a larger remnant than a single supernova exploding with the combined energies. This is also a direct consequence of the energy transform efficiency.

Another important factor affecting both the shape of shells and their final evolutionary phase is their location in the Galaxy. While shells expanding in a homogenous non-rotating medium remains spherical, real shells expands in the rotating Galaxy with stratified medium.

Simulations by Ehlerova et al. (1997) show that a shell expanding in stratified medium in a differentially rotating galaxy may develope a strongly non-spherical shape. Figure **1.2**$_{(10)}$ shows the shape of such a shell for three different half-thickness of the Gaussian disc—500, 200 and 100 pc—after expanding for a time of 20 Myr. The assumed Gaussian stratification of the interstellar medium in the direction z, perpendicular to the galactic disc, was:

$$n\left(z\right) = n_0 \exp\left(-\frac{z^2}{\sigma_z^2}\right), \tag{1.16}$$

where n is the particle density, n_0 is the particle density in the middle of the galactic disc and σ_z is the Gaussian half-thickness of the disc.

These simulations show that shells expanding near the edge of the Galactic disc can burst and blow out its content. If the shell is large enough with respect to the disc thickness, it can also create a hole through the disc. Consequences of these phenomena is discussed in the next section—1.2.4$_{(11)}$—Impact of H I Shells on The Ambient Interstellar Medium.

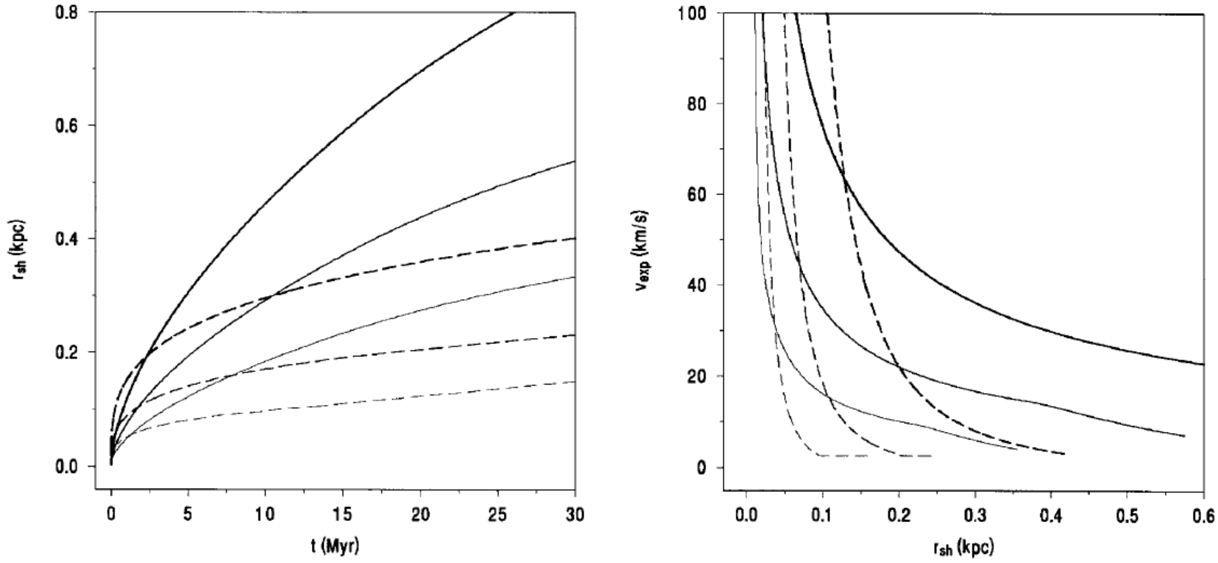

Figure 1.1: Evolution of expanding shells obtained from numerical simulations. The shells were supplied with the energies of 10^{52} erg (thin lines), 10^{53} erg (medium lines) and 10^{54} erg (thick lines). Solid lines denote continuous energy input, while dashed lines denote abrupt energy input. The density of surrounding medium was choosen to be 1.4 cm^{-3}. **Left:** The shell radius r_{sh} in kpc as a function of time. **Right:** The shell expansion velocity v_{exp} in km/s as a function of the shell radius. (Efremov et al., 1999, Fig. 1)

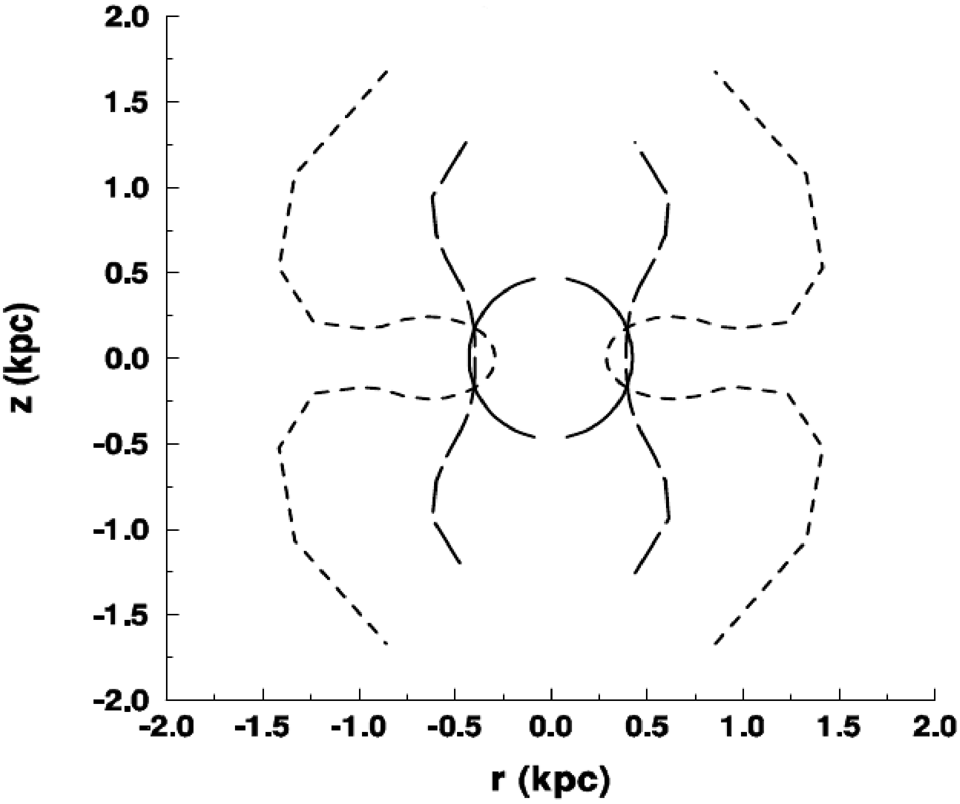

Figure 1.2: Shape of a shell expanding in medium stratified in the direction z (see equation $1.16_{(8)}$), perpendicular to the galactic plane, after expanding for a time of 20 Myr. Solid line is for $\sigma_z = 500$ pc, long-dashed line is for $\sigma_z = 200$ pc and short-dashed line is for $\sigma_z = 100$ pc. (Ehlerova et al., 1997, Fig. 4d)

1.2.4 Impact of H I Shells on the Ambient Interstellar Medium

H I shells may be responsible for supplying hot gas into the Galactic halo or even into intergalactic space. As most shells are created by OB associations, corresponding supernovae explosions heat the sparse gas inside them to temperatures $\propto 10^6$ K, besides they enrich the gas with heavy elements. A shell expanding near the edge of the Galactic disc may reach a region of steep pressure gradient which results in breakout of shell's border allowing hot gas to escape to the Galactic halo.

The Galactic fountain model by Shapiro & Field (1976) states that heated gas in the halo will later cool down and condensate, resulting in creation of a high-velocity cloud, falling back to the disc. Thus, H I shells may be respondible not only for replenishment of the Galactic halo but also for creating high-velocity clouds.

Furthermore, H I shells play an important role in triggered star formation. The borders consist of collected interstellar medium ploughed from the central hole, offering a suitable environment for star formation. As shell expands the mass of medium collected in a thin surrounding layer increases, which can result in the collapse caused by medium self-gravity.

The Jeans instability in a homogenous medium occurs, when (Bonnor, 1957)

$$L_{\mathrm{J}} > \left(\frac{\pi}{G\varrho} \frac{\mathrm{d}p}{\mathrm{d}\varrho} \right)^{1/2}, \tag{1.17}$$

where L_{J} is the characteristic linear dimension of the cloud—Jeans length, G is the Newtonian constant of gravitation, ϱ is the density of the cloud and p is the pressure. This condition may be reformulated in the situation of expanding shell which keeps the density of the collected medium increasing. This process was proposed by Elmegreen & Lada (1977) for expanding H II regions. An analytical formula for the instability of expanding layer was derived later by Whitworth et al. (1994) and Elmegreen (1994). The simulations of expanding H II regions were performed, for example, by Hosokawa & Inutsuka (2007); Dale et al. (2007); Hosokawa & Inutsuka (2006, 2005).

Studies of the collect and collapse scenario by Whitworth et al. (1994); Elmegreen & Lada (1977) show that this process can create more massive stars than spontaneous collapse. As the H II region expands it collects medium in a thin layer between the shock front and the ionization front. Cores of these fragments then collapse and create massive protostars of future OB stars. Later, these massive stars create secondary expanding H II regions.

Note that the necessary condition for shell to keep the density of the collected medium increasing is that the density of ambient medium does not decrease too fast—$\varrho \geq \mathrm{const.}\, r^{-2}$.

Triggered star formation has been observationally confirmed, for example in recent papers by Deharveng et al. (2007); Maheswar et al. (2007); Zavagno et al. (2007); Karr & Martin (2003).

Analytical studies and numerical simulations of expanding H I shells by Ehlerová & Palouš (2002); Palouš & Ehlerová (2002); Ehlerova et al. (1997) have shown that a large-scale variant of the collect and collapse process can be applicable to these shells tool. But there is a lack of observational evidences.

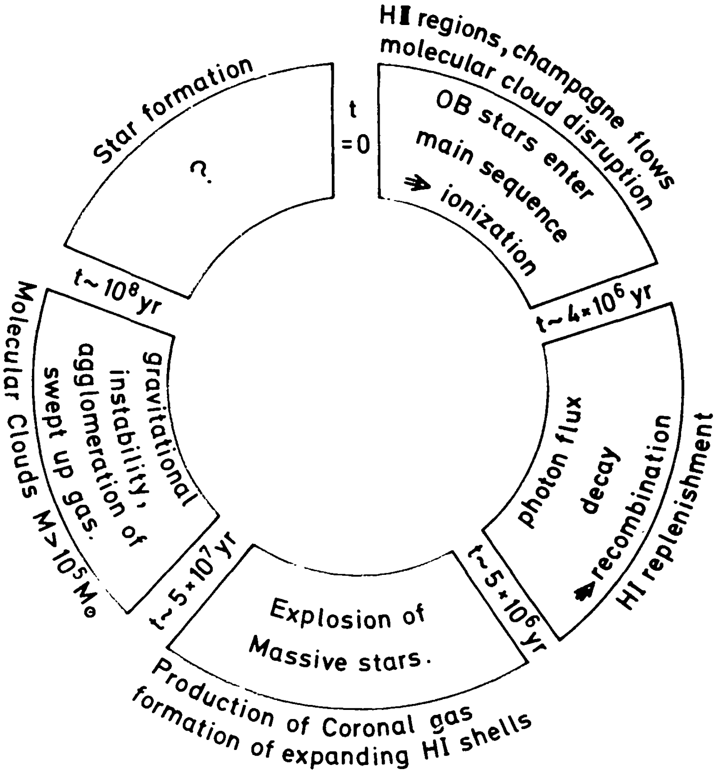

Figure 1.3: Concept of the closed circle of stellar evolution ("stellar ouroboros"). Note the position of H I shells in the lower segment. (Tenorio-Tagle & Bodenheimer, 1988)

Next way for H I shells to trigger star formation is via their collisions. This interaction compresses the interstellar medium making a better conditions for gravitational collapse resulting in faster and more intensive star formation. Because expanding H I shells are abundant structures in galaxies, their collisions may be common events.

Another possible way for H I shells to trigger star formation is via compression of some preexisting molecular cloud. Giant molecular clouds are observed to be in virial equilibrium, thus some shock wave passing through them may induce their collapse and trigger star formation—see review by Elmegreen (1998).

The role of H I shells in stellar evolution is shown on figure **1.3**$_{(12)}$ by Tenorio-Tagle & Bodenheimer (1988).

1.2.5 Measuring the Properties of H I Shells

Since H I shells are observed in the line emission of neutral hydrogen in radio domain, the used unit of intensity is Kelvin. The line spectrum also allows us to measure the Doppler shifts of the interstellar medium lines (see section $1.1.3_{(4)}$) to get the radial velocity of the medium.

H I data were traditionally available in the form of velocity spectra for particular direction in the sky. Today, they are available in the form of data cubes, with two spatial dimension—e.g. the galactic longitude and latitude—and one radial velocity dimension. If we want to derive some not directly observed properties of the medium, we can use equations presented in the section $1.1_{(2)}$. Because the longitude, the latitude and the radial velocity dimensions are separated into a set of discrete channels—pixels—we need to change integration for summation in these equations.

Particle Column Density

Let there be an ideal H I shell, discovered in the data cube, that has evacuated its interior completely. Then the particle density in the vicinity of this shell—n_{local}—can be derived as

$$n_{\mathrm{local}} \approx \frac{\Delta N}{\Delta s}, \tag{1.18}$$

where ΔN is the difference between the particle column density of the central hole and the ambient medium, Δs is the characteristic length of the shell. The characteristic length can be derived from the shell's angular dimension as

$$\Delta s = 2r_{\mathrm{sh}} = 2\sqrt{\frac{S}{\pi}} = 2d\sqrt{\frac{\Omega}{\pi}}, \tag{1.19}$$

where r_{sh} is the shell radius, S is the shell area, Ω is the shell angular area and d is the shell distance. Adjusting the formula $1.13_{(4)}$, describing the relation of brightness temperature with column density, we obtain

$$\Delta N = 1.823 \times 10^{18} \sum_{i=1}^{k} \delta T_{\mathrm{B,i}}\, \delta v, \tag{1.20}$$

where N is the column particle density in [cm^{-2}], k is the number of consecutive velocity channels occupied by the shell, $\delta T_{\mathrm{B,i}}$ is difference between the brightness temperature of ambient medium and the brightness temperature of the central hole in the i-th velocity channel, measured in [K] and δv is the width of one velocity channel, measured in [km/s]. This can be also expressed using the temperature averaged over the velocity interval (spanned by the H I shell):

$$\Delta N = 1.823 \times 10^{18}\, \Delta v\, \left\langle \delta T_{\mathrm{B}}\left(v\right)\right\rangle, \tag{1.21}$$

where $\delta \langle T_{\rm B}(v) \rangle$ is difference brightness temperature averaged over the velocity interval occupied by the shell, Δv is the velocity dimension of the shell. Having the brightness temperature averaged over the velocity channels—$\langle \delta T_{\rm B,i} \rangle$—this can be rewritten to

$$\Delta N = 1.823 \times 10^{18} \, \frac{\Delta v}{\delta v} \, \langle \delta T_{\rm B,i} \rangle \, , \tag{1.22}$$

Combining the equations above, we can express the local particle density as

$$n_{\rm local} \approx 5.317 \times 10^{-2} \, \frac{\Delta v \; \langle \delta T_{\rm B,i} \rangle}{\delta v \, d \, \sqrt{\pi \Omega}} , \tag{1.23}$$

where, $n_{\rm local}$ [cm^{-3}] is the local particle density in the vicinity of the H I shell; Δv [km/s] is the shell extend in the velocity dimension; $\delta \langle T_{\rm B,i} \rangle$ [K] is the mean difference between the shell central brightness temperature and the brightness temperature of the ambient medium, averaged over the velocity channels; d [kpc] is the shell distance and Ω [deg^2] is the shell angular dimension.

Energy

The average particle density in the shell position can be inserted into the formula by Chevalier (1974) to estimate the total energy of an expanding H I shell,

$$\boxed{\frac{E_{tot}}{\rm erg} = 5.3 \times 10^{43} \left(\frac{n_{\rm local}}{\rm cm^{-3}} \right)^{1.12} \left(\frac{r_{sh}}{\rm pc} \right)^{3.12} \left(\frac{v_{exp}}{\rm km \ \ s^{-1}} \right)^{1.4}} , \tag{1.24}$$

where $n_{\rm local}$ is the local particle density of ambient medium, r_{sh} is the shell radius and v_{exp} is the shell expansion velocity (half of the shell extent in velocity dimension). Note that this equation assumes expansion of a spherically symmetric shell into a homogenous medium, driven by an abrupt energy input. It was originally designed for expanding supernova remnants, thus the computed value may differ from the real energy of the shell. It should be interpreted as the energy of an equivalent explosion, that would create a similar shell.

Kinematical Distance

There are two methods of determinig the distances of H I shells for which we know their radial velocities. First, we can compute kinematical distances from formulas describing global galactic rotation. Second, we can read the distances from a graph of averaged radial velocities plotted as a function of the distance in a given direction from the Sun. The graph would be obtained from a large number of observations of different objects with known distances and radial velocities. Because the first—analytical—way is actually based on formulas with parameters obtained by fitting of a large number of individual measurements, more accurate (more direct) is the second method.

To derive kinematical distances of studied H I shells, I have used the graph **1.4**(15) by Brand & Blitz (1993). The graph displays contours of measured radial velocities of a large number of objects in the neighbourhood of the Sun with known distances.

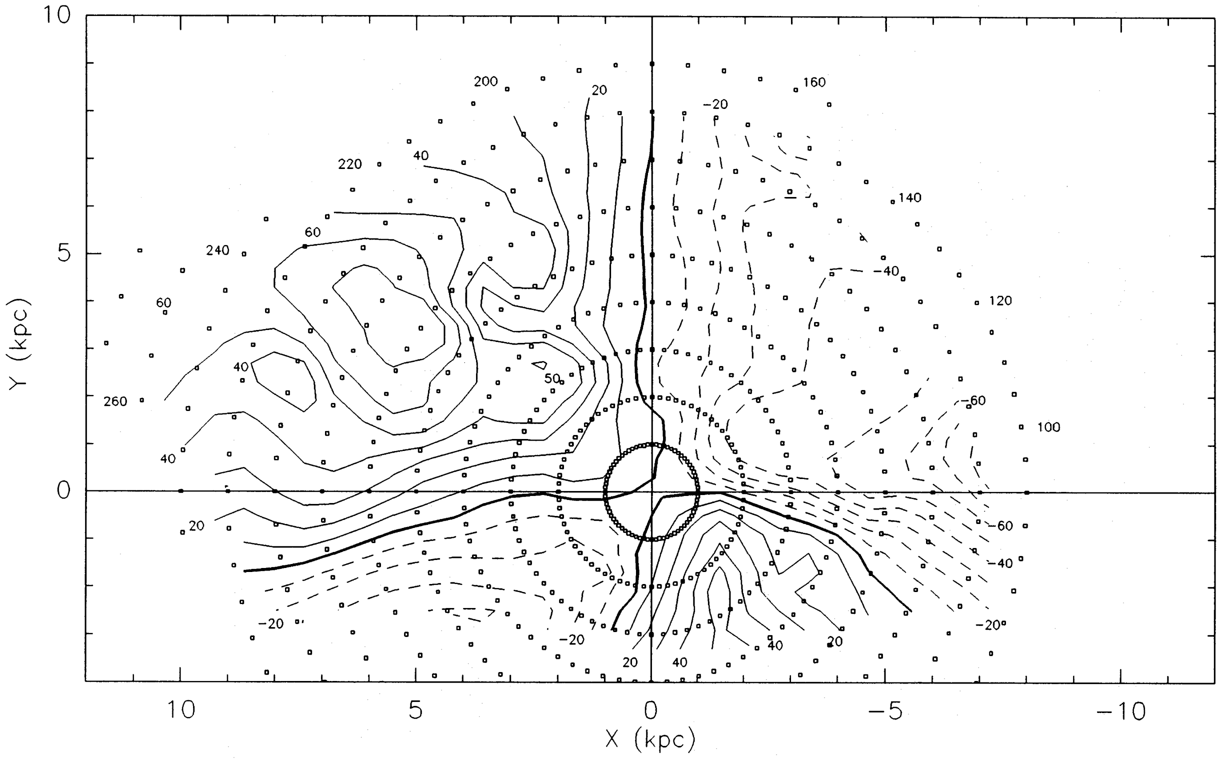

Figure 1.4: Contours of the observed radial velocities, projected onto the Galactic plane. The Sun is located at the position (0, 0); the Galactic center is at (0, −8.5). The heliocentric distance and the Galactic longitude are marked by points arranged in the concentric circles with radius steps by 1 kpc and angular steps by 5 deg. (Brand & Blitz, 1993)

1.2.6 Counterparts of H I Shells

H I shells are observed in neutral hydrogen, i.e at the wavelength of 21 cm. The question is if there can be present some counterparts that we could observed at different wavelength.

Radio—CO Line

Carbon monoxide, CO, is the molecule well mixed with cool molecular hydrogen (H_2) condensed in clouds. Because molecular hydrogen is almost invisible to direct observations, CO molecule is traditionally used as its tracer[4].

Molecular hydrogen is required to form stars, thus its condensations are early signs of possible future star formation. Following the concept of expanding H I shell collecting ambient medium in its borders, we may expect to detect clouds of molecular hydrogen along the borders of older shells.

Infrared—Dust Continuum

Following the overviews of Sauvage (1997); Boulanger (1999), dust is abundant in discs of galaxies. It emits mostly in the infrared domain. While the smallest dust grains—large molecules of polycyclic aromatic hydrocarbons (PAHs)—emits nonthermally, emission from large grains is well descirbed by a single Planck curve with the temperature of 17.5 K. This temperature denotes how much do we need to cool down out telescopes to distinguish the dust emission from the emission of telescope itself.

One source of dust heating is the global Galactic radiation field. This heating mechanism produces widespread, faint and diffuse emission. Another source of heating is radiation from star forming regions. This heating mechanism produces more compact, intensive emission.

Because dust is probably mixed both with molecular hydrogen and atomic hydrogen, we should observe its emission correlated with both CO line and H I line. The type of emission—diffuse or localized—would reveal the heating source, thus it may indicate early stages of star formation.

The dust emission spectrum from the paper of Boulanger (1999) is shown on figure **1.5**$_{(18)}$. Note that the emission from large grains is between wavelengths of 100 to 1000 µm.

Optical—Hα Line

Because Hα emission is associated with H II regions, it can serve as a direct tracer of very recent or ongoing star formation.

---

[4] CO molecule emits light as a result of rotational transitions. The lowest transition produces the line centered at the wavelength of 2.6 mm, or equivalently frequency 115 GHz. Though this wavelength is interacting with the Earth's atmosphere, especially with water vapor, it is received by high-altitude ground telescopes, located in dry environment.

Assuming that the H I shell has been created by an OB association, we can expect two types of associated Hα emission. First, diffuse Hα emission apparently filling the shell interior as a result of the original OB association that has created the H I shell. Second, more compact Hα emission from young H II regions apparently associated with shell borders or around the shell as a result of star formation triggered by the shell.

The study of H I shells in the nearby galaxy IC 2574 by Walter & Brinks (1999) has shown that H II regions tend to be located on the rims of H I shells—see figure **1.6**$_{(19)}$—and in only one case a diffuse Hα emission is observed inside an H I shell. This study supports the theory of star formation triggered by H I shells.

X-Ray—Hot Gas Continuum

Soft X-ray diffuse emission—photon energies about 0.25 eV—is associated with thermal emission of hot gas. This gas has been found either in the Galactic halo or in the Local Hot Bubble[5](Cox & Reynolds, 1987; Snowden et al., 1997).

Some H I shells may contain hot gas, therefore we may expect to observe counterpart X-ray emission.

---

[5] Local Hot Bubble = a bubble in interstellar medium surrounding the Sun in a radius of about 100 pc.

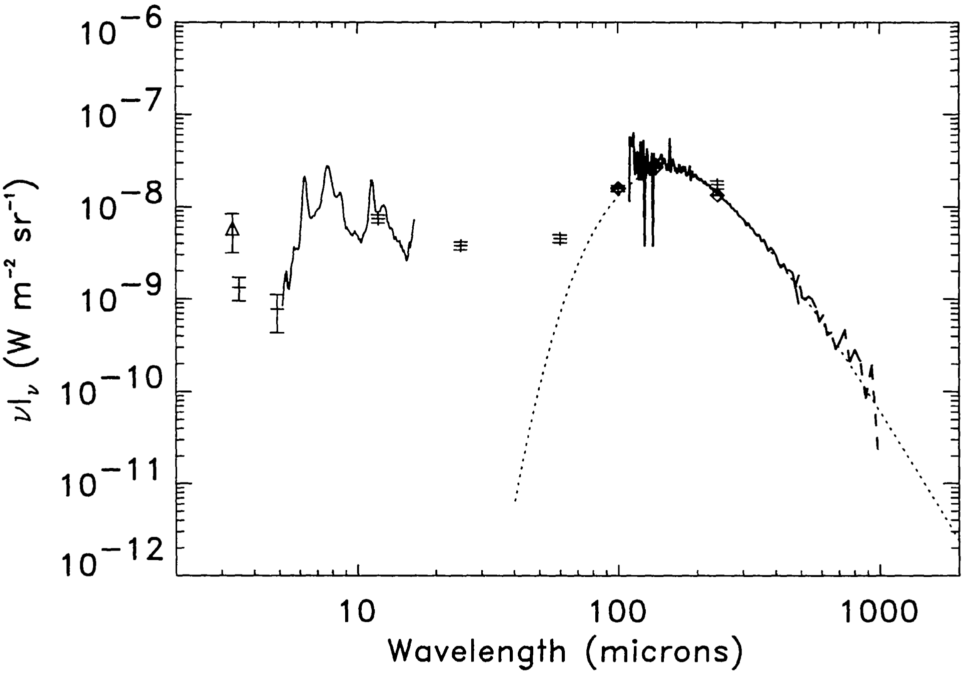

Figure 1.5: The dust emission spectrum from the near-infrared to millimeter wavelengths normalized for a column density of 10^{20} hydrogen atoms per cm^{-2}. At short wavelengths, the emission is nonthermal, while at long wavelengths it is well fitted by a single Planck function with temperature 17.5 K (dotted line). (Image published by Boulanger, 1999 with using spectra by Giard et al., 1994; Boulanger et al., 1996b; Bernard et al., 1994; Boulanger et al., 1996a.)

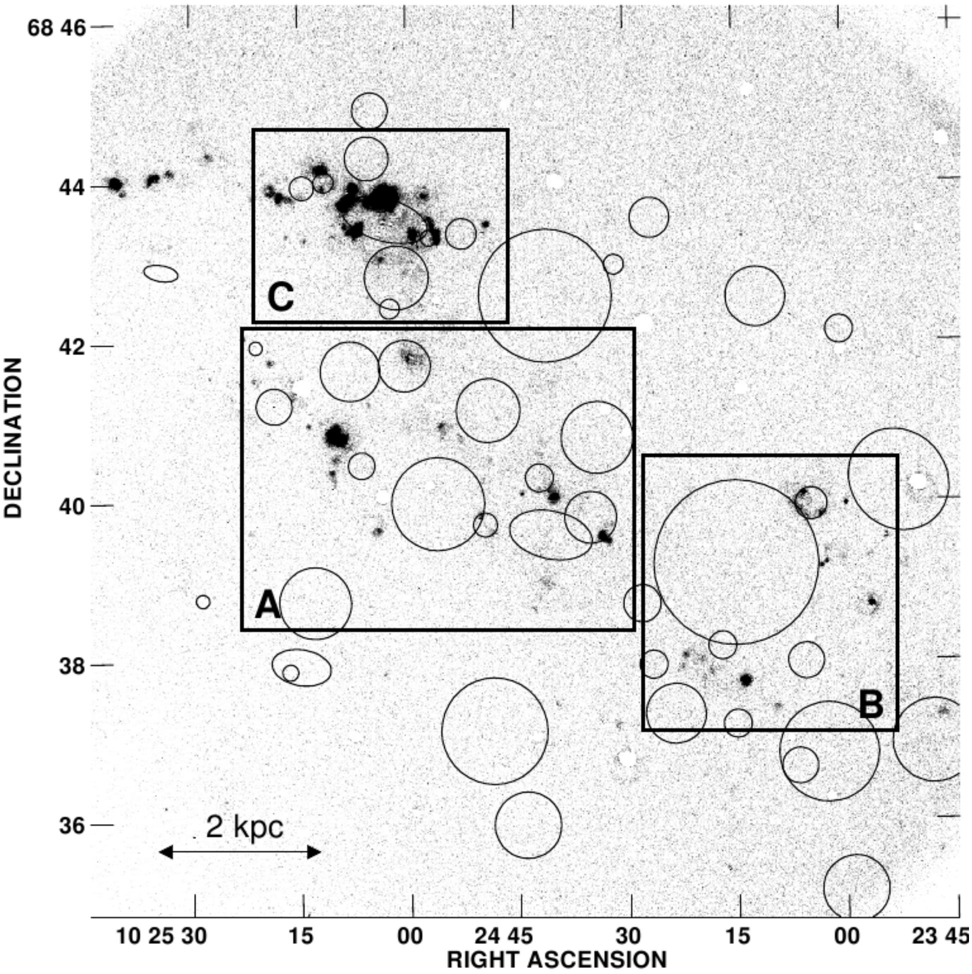

Figure 1.6: Hα emission (gray background) from the dwarf galaxy IC 2574 with overlaid identified H I shells (ellipses). Note that almost all distinct H II regions are located on the rims of H I shells. (Picture from the paper of Walter & Brinks, 1999. Rectangular areas A, B, C were studied in a more detail.)

Chapter 2

Searching for Counterparts of H I Shells

2.1 Data Sources

2.1.1 Radio—Neutral Hydrogen Line

As the basic source of 21 cm radio data, I have used the *Leiden/Argentine/Bonn Galactic H I Survey*[1] (Kalberla et al., 2005). See figure **2.1**$_{(22)}$.

The survey merges two H I surveys (Hartmann & Burton, 1997; Bajaja et al., 2005; Arnal et al., 2000) to a full-sky data cube of neutral hydrogen emission in the Milky Way Galaxy. The data are distributed in FITS[2] files containing spatial maps for each LSR[3] radial velocity channel in the range range -450 to $+400$ km/s. The width of a singe velocity channel is 1.03 km/s. The maps are in equirectangular projection[4]. These radio data of neutral hydrogen emission provide essential images of H I shells.

The used file is `lab250h.fit`[5], containing the subset velocity interval of -250 to $+250$ km/s. An overview of the whole sky in neutral hydrogen line is seen on figure **2.1**$_{(22)}$.

---

[1] Website: http://www.astro.uni-bonn.de/∼webrai/english/tools_ labsurvey.php; FTP archive: ftp://cdsarc.u-strasbg.fr/pub/cats/VIII/76/

[2] FITS = **F**lexible **I**mage **T**ransport **S**stem

[3] LSR = **L**ocal **S**tandard of **R**est

[4] Equirectangular projection is also called Cartesian projection.

[5] `lab250h.fit`: ftp://cdsarc.u-strasbg.fr/pub/cats/VIII/76/lab250h.fit.gz

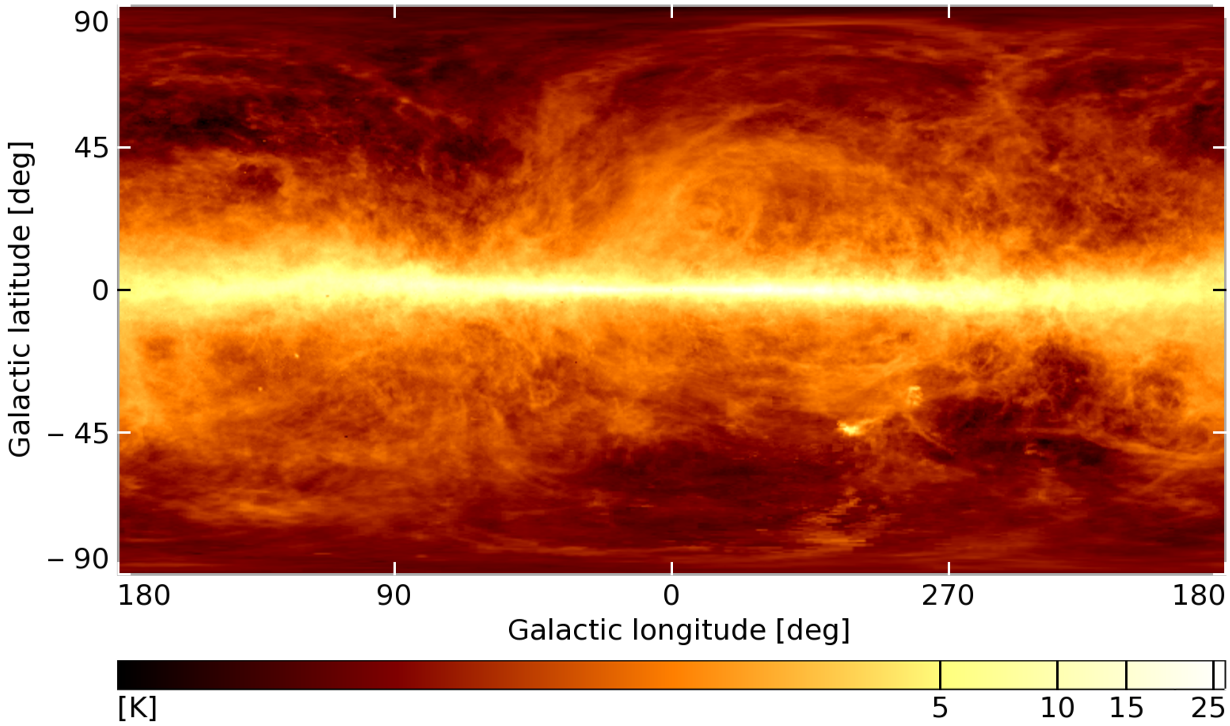

Figure 2.1: Full-sky image of neutral hydrogen line (21 cm). The intensity is measured in units of brightness temperature, averaged over all 1.03 km/s wide velocity channels from the interval ±250 km/s. (Leidergentine/Bonn Galactic H I Survey, Kalberla et al., 2005)

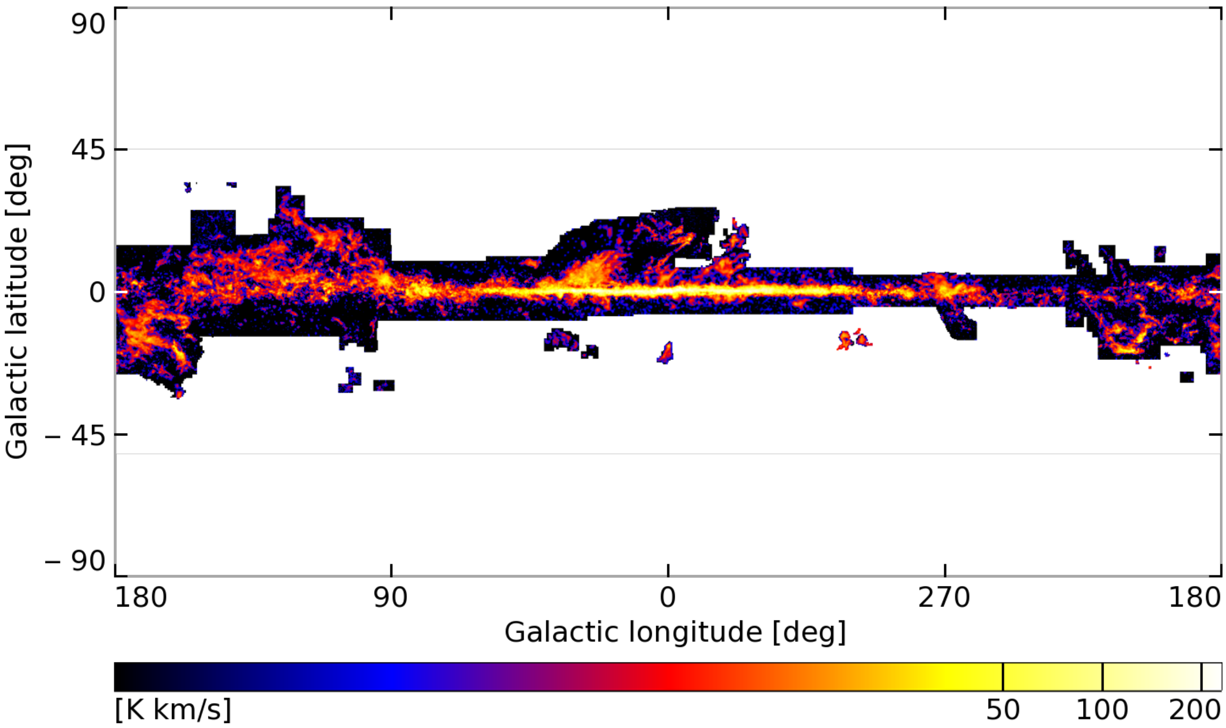

Figure 2.2: CO line emission (2.6 mm) near the Galactic disc. (Milky Way in Molecular Clouds: A New Complete CO Survey, Dame et al., 2001)

2.1.2 Radio—CO Line

As the source of CO line emission (2.6 mm), I have used the *Milky Way in Molecular Clouds: A New Complete CO Survey*[6] (Dame et al., 2001). This in an composite survey consisting of 37 parts. It covers the whole Galactic disc and some adjacent regions. Because this is not a full-sky survey data are available only for some H I shells. See an overview on figure **2.2**(23).

The data are available in FITS files, containing spatial maps integrated over velocity channels. The projection used is equirectangular with galactic coordinates. Because the center of the map is shifted slightly from the Galactic center, I have reprojected the image, so that its center corresponds to the Galactic center. This is more suitable for comparison with other data.

The used file is `Wco_DHT2001.fits`[7].

---

[6] Website: http://cfa-www.harvard.edu/mmw/MilkyWayinMolClouds.html

[7] `Wco_DHT2001.fits`: http://cfa-www.harvard.edu/mmw/Wco_DHT2001.fits.

2.1.3 Infrared—Dust Continuum

As the source of infrared continuum emission, I have used the *IRIS—Improved Reprocessing of the IRAS Survey*[8]. (Miville-Deschênes & Lagache, 2005). The survey provides reprocessed images taken by the *IRAS*[9] satellite in 1983. It is an all-sky survey in four infrared bands centered at: 12 μm, 25 μm, 60 μm and 100 μm. While the 12 and 25 μm bands contain emission from the smallest dust grains—PAHs[10]—the 60 and 100 μm bands represent thermal emission from larger grains.

I have used the 100 μm band, because it reveals both bright compact sources and faint diffuse regions. Besides this band was also used for searching for far-infrared loops (see section 2.1.7$_{(31)}$).

The data are available in a set of FITS files, representing individual reprocessed IRAS plates, with angular dimension about 12.5×12.5 deg. The used coordinates are right ascension and declination in tangent projection. I have reprojected and mosaicked these plates into the large maps in equirectangular projection with galactic coordinates. See the figure **2.3**$_{(25)}$ for an overview of all-sky continuum emission at 100 μm.

The used file—package containing individual plates—is `IRISNOHOLES_B4H0.tar.gz`[11].

---

[8] Website: http://lambda.gsfc.nasa.gov/product/iras/

[9] IRAS = **I**nfra**R**ed **A**stronomical **S**atellite

[10] PAHs = **P**olycyclic **A**romatic **H**ydrocarbons, the smallest discovered dust grains.

[11] `IRISNOHOLES_B4H0.tar.gz`:
http://www.cita.utoronto.ca/~mamd/IRIS/data/IRISNOHOLES_B4H0.tar.gz

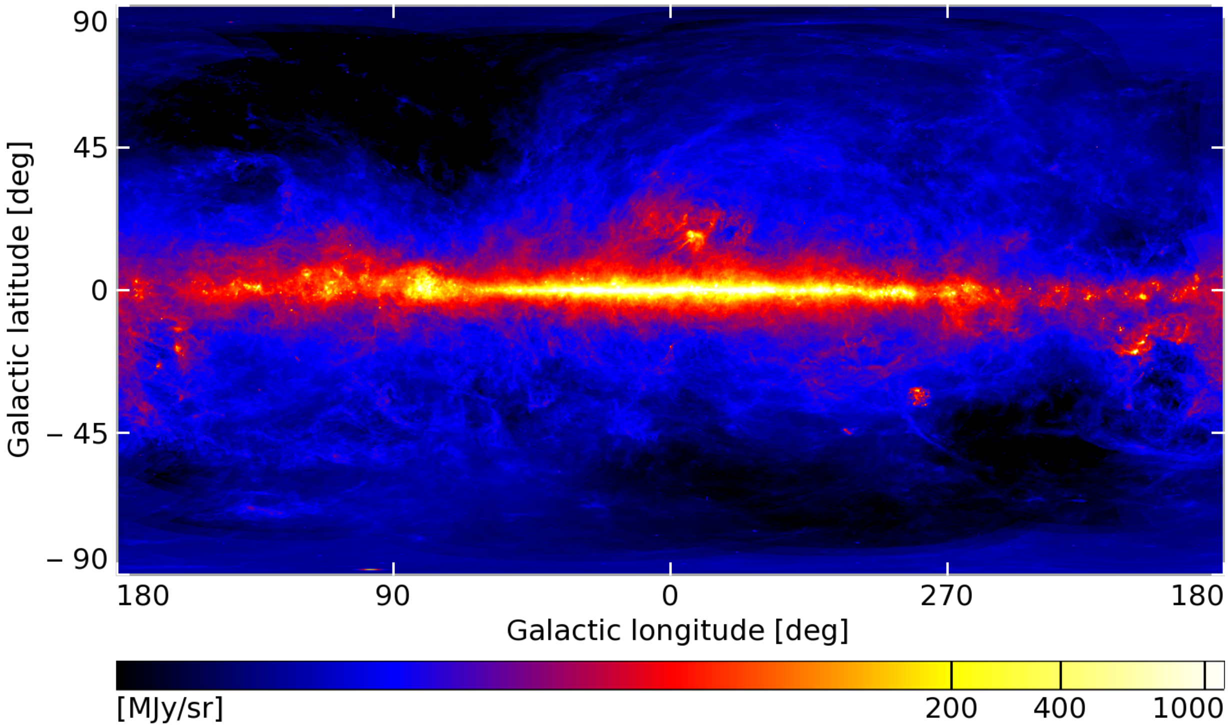

Figure 2.3: All-sky continuum dust emission at 100 μm. (IRIS—Improved Reprocessing of the IRAS Survey, Miville-Deschênes & Lagache, 2005)

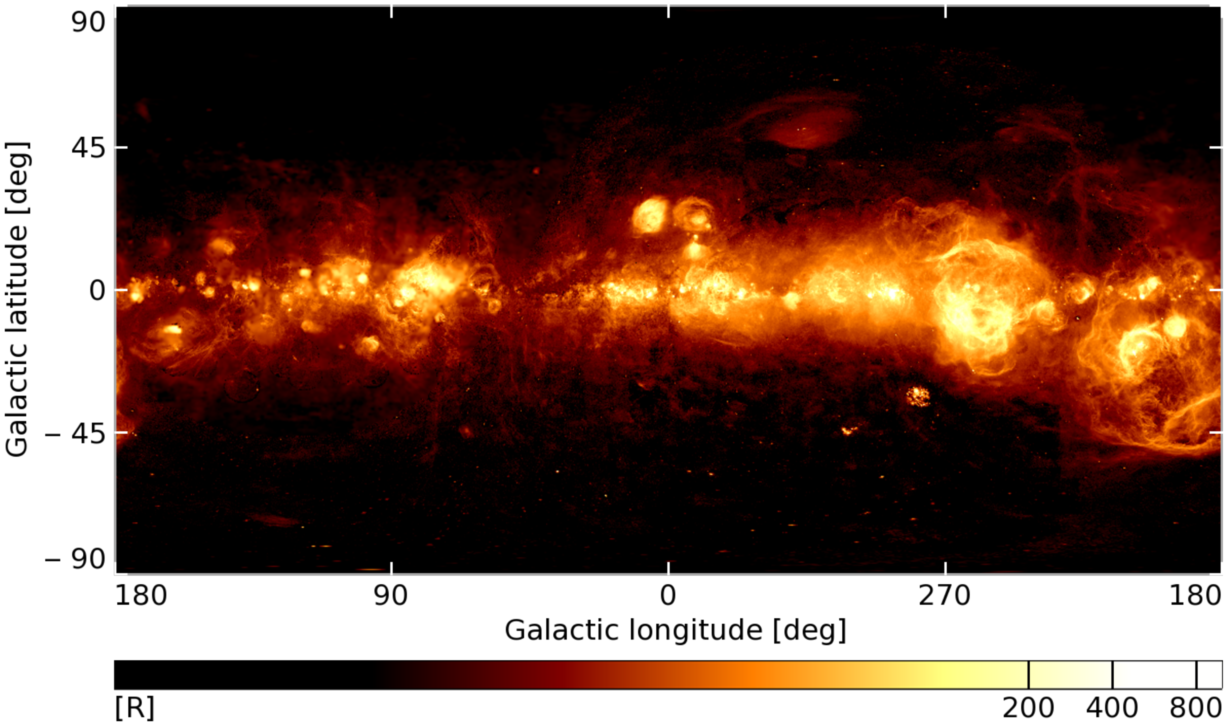

Figure 2.4: All-sky Hα line emission (656 nm). (H-alpha Full Sky Map, Finkbeiner, 2003)

2.1.4 Optical—Hα Line

As the source of Hα line emission (656 nm), I have used the *H-alpha Full Sky Map*[12] (Finkbeiner, 2003). This map is assembled from the following three surveys, together covering the full-sky: *The Wisconsin Hα Mapper Northern Sky Survey*[13](Haffner et al., 2003), *The Southern H-Alpha Sky Survey Atlas*[14](Gaustad et al., 2001) and *The Virginia Tech Spectral-Line Survey*[15]. The data are available in FITS file. They are represented in equirectangular galactic projection, so no reprojection was needed. See figure **2.4**$_{(26)}$ for an overview.

The used file is `Halpha_map.fits`[16].

---

[12] Website: http://www.astro.princeton.edu/∼dfink/halpha/

[13] WHAM website: http://www.astro.wisc.edu/wham/; The Wisconsin H-Alpha Mapper is funded by the National Science Foundation.

[14] http://amundsen.swarthmore.edu/SHASSA/; The Southern H-Alpha Sky Survey Atlas is supported by the National Science Foundation.

[15] http://www.phys.vt.edu/∼halpha/; The Virginia Tech Spectral-Line Survey is supported by the National Science Foundation

[16] `Halpha_map.fits`:
http://www.astro.princeton.edu/∼dfink/halpha/data/v1_1/maps/Halpha_map.fits

2.1.5 X-Ray—Hot Gas Continuum

As the source of X-ray emission, I have used *The ROSATX-Ray All-Sky Survey.* The survey is based on the data taken by the German satellite ROSAT[17], which was operating between the years 1990 and 1999. Its instruments were sensitive to X-ray radiation in the energy range 0.1–2 keV and extreme ultraviolet radiation in the energy range 0.042–0.21 keV.

I have used the second band, *R2*, from the data release *12' Maps of the Soft X-ray Diffuse Background*(Snowden et al., 1997). It covers energies between 0.14 and 0.284 keV in soft X-ray domain and belongs to the thermal emission of hot gas with temperatures of a few MK. This band is further referred as 0.25 keV band. See figure **2.5**$_{(28)}$ for an overview.

For each band, data are available in six FITS files, covering the whole sky. The projection used is Zenithal Equal Area in galactic coordinates. I have reprojected and mosaicked the individual maps into a single all-sky map. See an overview on figure **2.5**$_{(28)}$.

The used files are: `g000m90r2b120pm.fits`[18], `g000p00r2b120pm.fits`[19], `g000p90r2b120pm.fits`[20], `g090p00r2b120pm.fits`[21], `g180p00r2b120pm.fits`[22], `g270p00r2b120pm.fits`[23].

Note The FITS files from the data release “12’ Maps of the Soft X-ray Diffuse Background” by Snowden et al. (1997) contain wrong astrometric records in their headers. See appendix C$_{(101)}$ for details.

---

[17] ROSAT = **Rö**ntgen**sat**ellit; Website: http://www.xray.mpe.mpg.de/cgi-bin/rosat/rosat-survey

[18] `g000m90r2b120pm.fits`: http://www.xray.mpe.mpg.de/rosat/survey/sxrb/12/g000p90r2b120pm.fits

[19] `g000p00r2b120pm.fits`: http://www.xray.mpe.mpg.de/rosat/survey/sxrb/12/g000p00r2b120pm.fits

[20] `g000p90r2b120pm.fits`: http://www.xray.mpe.mpg.de/rosat/survey/sxrb/12/g000m90r2b120pm.fits

[21] `g090p00r2b120pm.fits`: http://www.xray.mpe.mpg.de/rosat/survey/sxrb/12/g090p00r2b120pm.fits

[22] `g180p00r2b120pm.fits`: http://www.xray.mpe.mpg.de/rosat/survey/sxrb/12/g180p00r2b120pm.fits

[23] `g270p00r2b120pm.fits`: http://www.xray.mpe.mpg.de/rosat/survey/sxrb/12/g270p00r2b120pm.fits

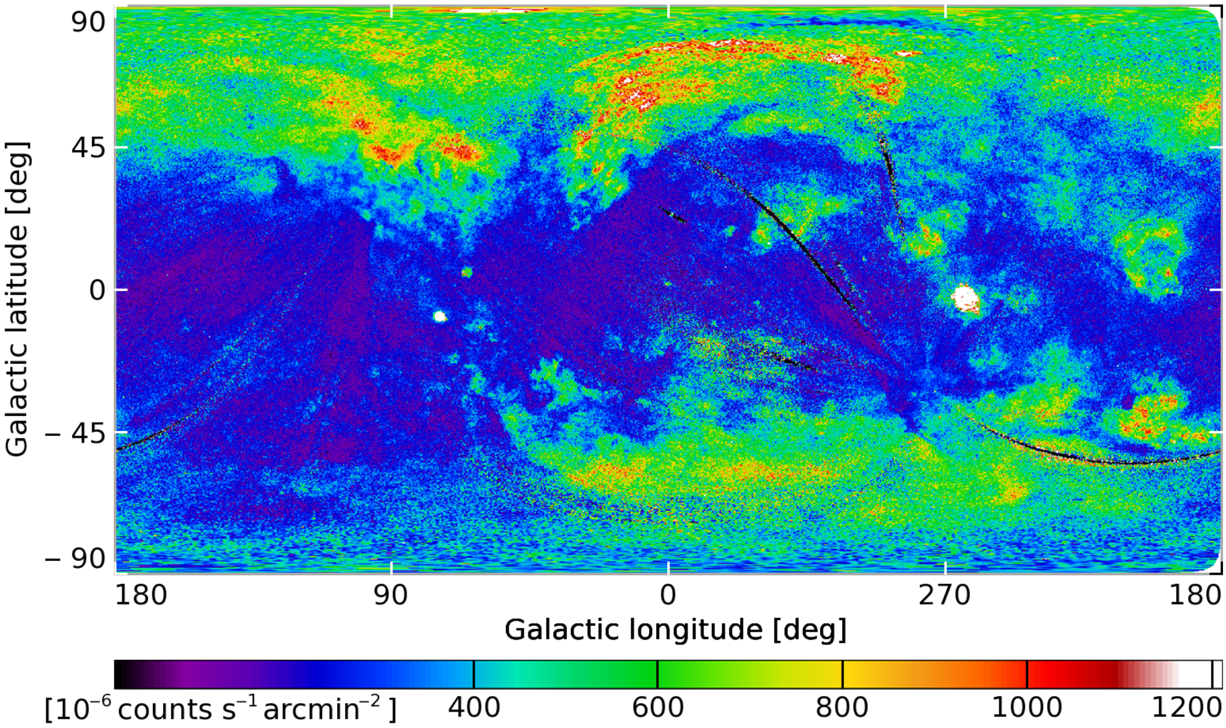

Figure 2.5: Soft X-ray continuum (0.25 keV) revealing hot gas in Galactic halo. (The ROSAT X-Ray All-Sky Survey, Snowden et al., 1997)

2.1.6 Catalogue of H I Shells

The essential source of data for this work is the catalogue of H I shells in the Milky Way Galaxy, presented by Ehlerová & Palouš (2005). For an overview, see the figure **2.6**(29). The catalogue is based on the *Leiden-Dwingeloo H I survey*[24] (Hartmann & Burton, 1997), made between years 1989 and 1993 with the Dwingeloo 25 m telescope in the Netherlands. The H I data were searched for expanding H I shell by a computer program. There are 628 expanding H I shell found in the Milky Way Galaxy, distributed acros the sky, with a gap around longitude 300 deg. Because at that time homogenous H I data were available only for northern sky, the gap in the catalogue is present.

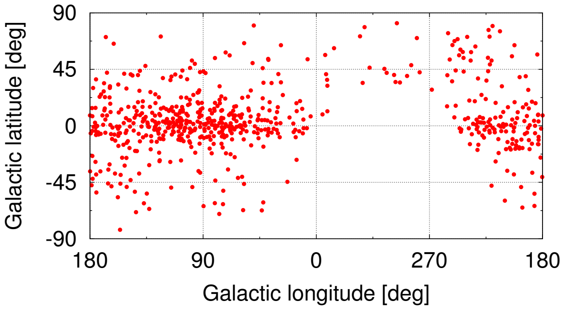

Figure 2.6: Positions of all H I shells from the catalogue Ehlerová & Palouš (2005).

The used file is 'table1.dat'[25], containing the whole catalogue in ASCII[26] format. The H I shells are displayed on figure **2.7**(30). A simplified plot containing only shell's positions is on figure **2.6**(29).

---

[24] Note that the Leiden-Dwindeloo survey is part of the Leidergentine/Bonn Galactic H I Survey (section 2.1.1(21)).

[25] table1.dat: ftp://cdsarc.u-strasbg.fr/pub/cats/J/A+A/437/101/table1.dat

[26] ASCII = **A**merican **S**tandard **C**ode for **I**nformation **I**nterchange

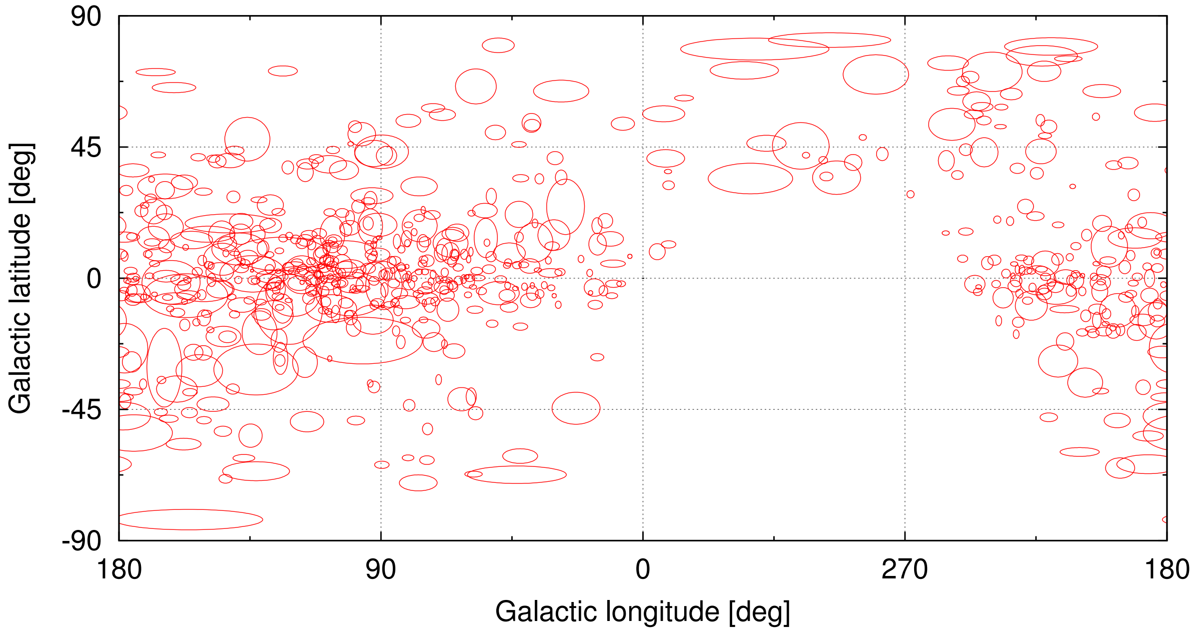

Figure 2.7: H I shells from the catalogue of Ehlerová & Palouš (2005).

2.1.7 Catalogue of Far-Infrared Loops

Far-infrared loops are structures very similar to H I shells. The catalogue is based on IRAS all-sky far-infrared data—hence the name—of dust emission at 100 and 60 μm. The loops were searched for by eye in the ISSA plates—data release of IRAS. The catalogue contains 462 far-infrared loops identified in the Milky Way Galaxy. Distance estimates based on associated objects are given for 73 loop.

The all-sky catalogue of far-infrared loops is available in two consecutive data releases: Kiss et al. (2004)[27] and Könyves et al. (2007)[28].

The used files are

- Kiss et al. (2004):
  ‘tablea.dat’[29]—positions, shapes
  ‘table2n.dat’[30]—distances
- Könyves et al. (2007):
  ‘appenb.dat’[31]—positions, shapes
  ‘appenc.dat’[32]—distances

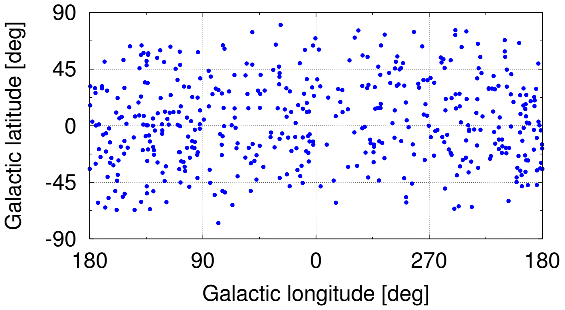

Figure 2.8: Positions of far-infrared loops from the catalogue (Kiss et al., 2004; Könyves et al., 2007).

For an overview of the catalogue projected to the equirectangular galactic coordinates see figure **2.9**(32)—ellipses—or figure **2.8**(31)—only positions.

Note There is a bug in data description in the file ReadMe by Könyves et al. (2007): The position angle of the ellipse is defined here as `...relative to the Galactic longitude main circles, from E to N`. But—following the original images of recognized far-infrared loops available online at http://kisag.konkoly.hu/CFIRLG/—the position angle is from N to E. (Assuming that the galactic longitude is increasing eastwards.) This bug is manifested also in the paper (Könyves et al., 2007, fig. 1). For the correct visualization, see figure **2.9**(32).

---

[27] FTP access: ftp://cdsarc.u-strasbg.fr/pub/cats/J/A+A/418/131

[28] FTP access: ftp://cdsarc.u-strasbg.fr/pub/cats/J/A+A/463/1227

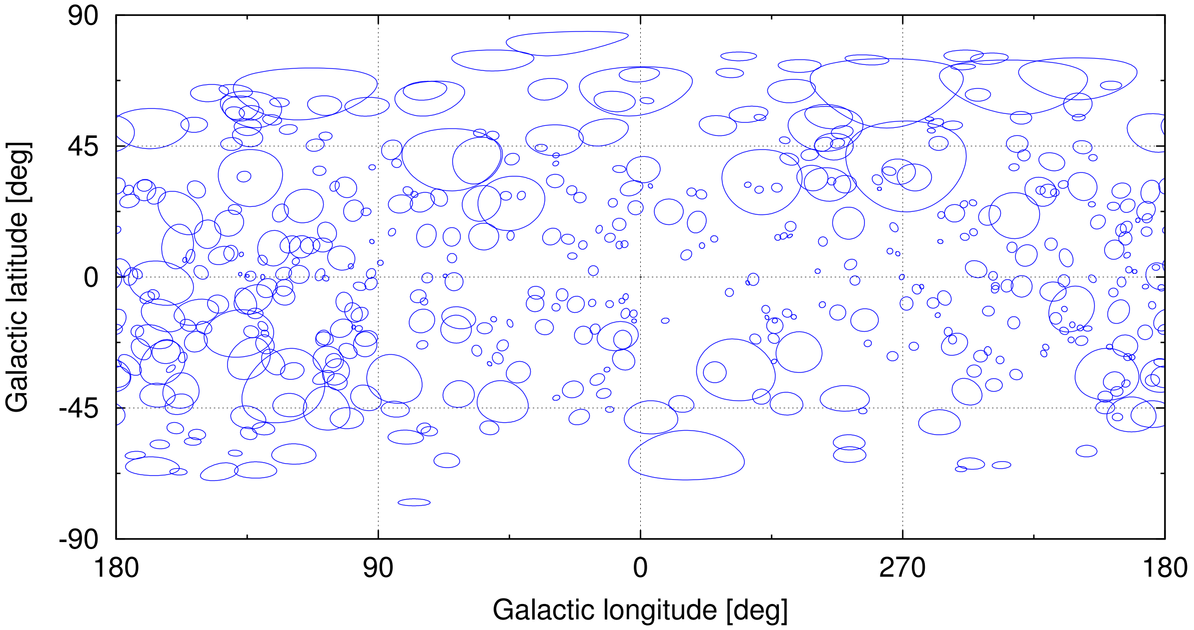

Figure 2.9: Far-infrared loops from the catalogue of Kiss et al. (2004); Könyves et al. (2007).

2.2 Counterpart Far-Infrared Loops

Because dust is well mixed with both neutral and molecular hydrogen some far-infrared loops should be associated with H I shellls.

Besides the general correlation between dust and gas, there are two additional possible physical connections of H I shells and far-infrared loops:

- Through the first generation of stars: A far-infrared loop is in this case dust collected and heated by the original OB association, that have also created the H I shell.
- Through the second generation of stars: In this case, triggers formation of new stars. These young stars heat up the ambient dust and the dust emits infrared radiation. Because the second generation of stars is arranged in the area formed out of the original shell, we would observe the dust as a far-infrared loop. Therefore far-infrared loops may serve as indicators of early stages of star formation.

In the first case, IR dust emission would be faint, diffuse and rather uniform, while in the second case, emission would be stronger with hot spots and point-like sources of emission excesses.

The global layout of H I shells and IR loops (figure **2.10**$_{(35)}$ and **2.11**$_{(36)}$) shows significant differences between the two sets: H I shells are concentrated towards the galactic disc, while IR loops cover the sky quite uniformly. Far-infrared loops are much more local compared to H I shells, which is due to the dust extinction preventing us to see the distant infrared dust. On the other hand, in H I radio emission we can detect even very distant H I structures at the opposite parts of the Milky Way Galaxy. Therefore in order to search for counterparts, only those H I shells should be taken into account that are close enough to observe their corresponding infrared emission.

The process of searching for counterparts was divided into the following consecutive steps:

1. automatic searching by the **findcan** program,
2. manual checking the list of H I shells–IR loop pairs.

The program *findcan*—written in the C programming language—outputs a list of pairs of H I shellls and IR loops that are apparently associated. The input is the list of H I shells, the list of IR loops and three threshold parameters—thres_dist, thres_area_ratio and thres_hi_dist_cut.

thres_dist is the H I shell–IR loop center-to-center relative distance threshold. To become a candidate pair for counterparts, the angular distance between the H I shell and the IR loop have to be less than or equal to the thres_dist value. The angular distance on the celestial sphere is computed using the haversine formula (equation A.4$_{(98)}$).

thres_area_ratio is the area ratio threshold. The ratio of the angular areas of corresponding H I shells and IR loops have to be in the interval from thres_area_ratio^{-1} to thres_area_ratio. The angular area is computed on the celestial sphere—for IR loops directly as the area of an ellipse (area $= \pi ab$)—for H I shells using reprojection from equirectangular coordinates onto the sphere and then by numerical integration.

thres_hi_dist_cut is the distance threshold in kpc for the H I shells. Only the shells with kinematical distances less than or equal to the thres_dist are taken into account. The purpose of this criterion is to throw away these H I shells that are too far away to observe a corresponding IR loop. The kinematical distance is computed from equation A.9$_{(98)}$, using the rotational velocity of 220 km/s and the galactocentric distance of 8.5 kpc (IAU recommended values). When the kinematical distance of a sheel can not be determined—see further text—the shell is not thrown away.

The threshold parameters used for the search are in table **2.1**$_{(35)}$.

The candidate pairs for counterparts are shown in figure **2.12**$_{(37)}$ and overviewed in table **2.2**$_{(38)}$. The pairs selected for multiwavelength study are shown in figure **2.13**$_{(37)}$.

On kinematical distances When using the equation A.9$_{(98)}$ to determine the kinematical distance, we need to know the rotational velocity—θ_0—and the galactocentric distance of the Sun—R_0. I have used the canonical values of IAU ($\mathrm{R}_0 = 8.5$ kpc, $\theta_0 = 220$ km/s), but measurements show that the real values may be significantly different, for example:

- $\mathrm{R}_0 = 7.9 \pm 0.8$ kpc, $\theta_0 = 200 \pm 10$ km/s (Merrifield, 1992);
- $\mathrm{R}_0 = 7.66 \pm 0.32$ kpc, $\theta_0 = 237 \pm 12$ km/s (Metzger et al., 1998);
- $\mathrm{R}_0 = 7.94 \pm 0.42$ kpc (Eisenhauer et al., 2003);
- $\mathrm{R}_0 = 7.62 \pm 0.32$ kpc (Eisenhauer et al., 2005).

An interesting determination of the galactocentric distance was done by Reid (1993) who had used several at that time publicated values to estimate the most likely one: $\mathrm{R}_0 = 8.0 \pm 0.5$ kpc.

Kinematical distances of H I shells located in the I. and IV. Galactic quadrant have ambiguous solutions. This is a consequence of the symmetry with respect to the subcentral point[33]. Ambiguity is reflected by the plus-minus sign in the equation A.9$_{(98)}$. Moreover there are H I shells manifesting peculiar radial velocities with respect to the ideal—cylindrical—rotation of the Galaxy. For these shells kinematical distances are not derived.

---

[33] subcentral, or tangent point = the closest point to the Galactic center for a given direction

Table 2.1: Settings of the threshold parameters in the findcan program.

Parameter	Value
thres_dist	$0.5 * 2/3$
thres_area_ratio	3.0
thres_hi_dist_cut	3.5

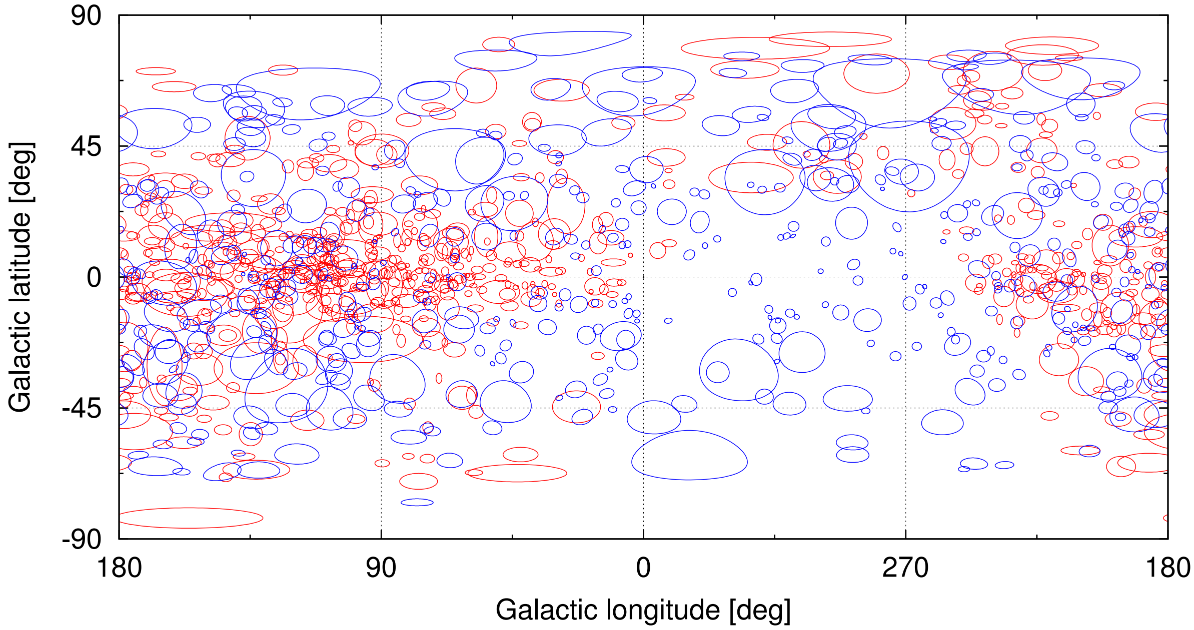

Figure 2.10: H I shells from the catalogue Ehlerová & Palouš (2005) (red ellipses) versus far-IR loops from the catalogue Kiss et al. (2004); Könyves et al. (2007) (blue ellipses).

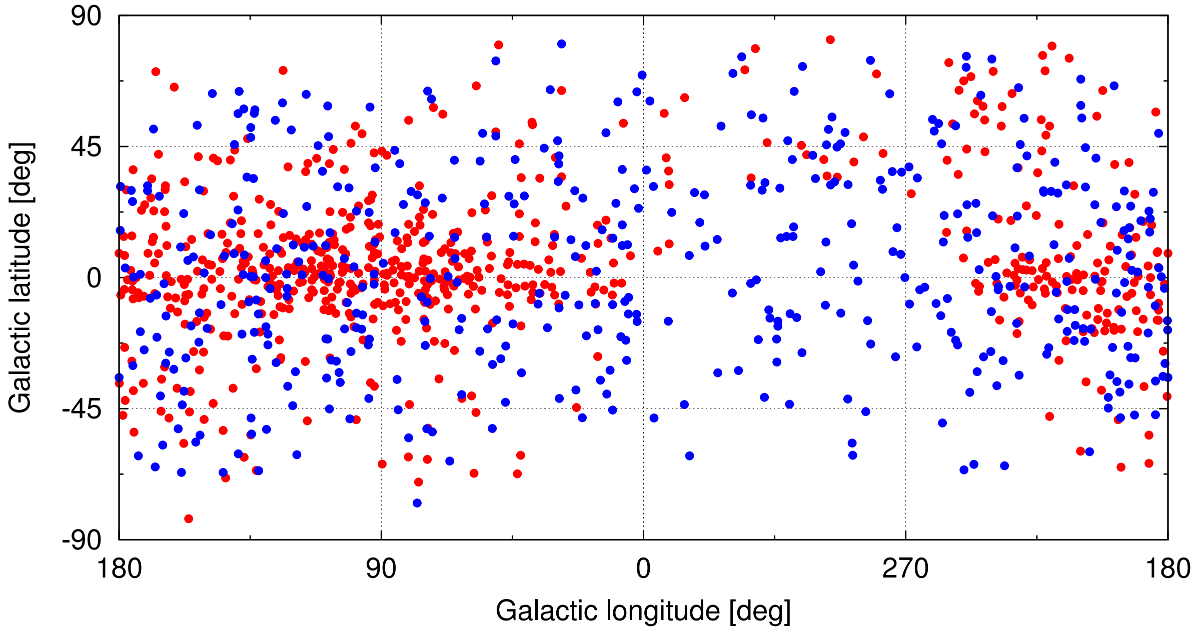

Figure 2.11: H I shells from the catalogue Ehlerová & Palouš (2005) (red points) versus far-IR loops from the catalogue Kiss et al. (2004); Könyves et al. (2007) (blue points). Note the different distribution of loops and shells with respect to the Galactic disc. The gap in the catalogue of H I shells between the longitude 0 and 270 deg is a result of using a non–full-sky data to build the catalogue up. See section 2.2$_{(33)}$—Counterpart Far-Infrared Loops—for further discussion.

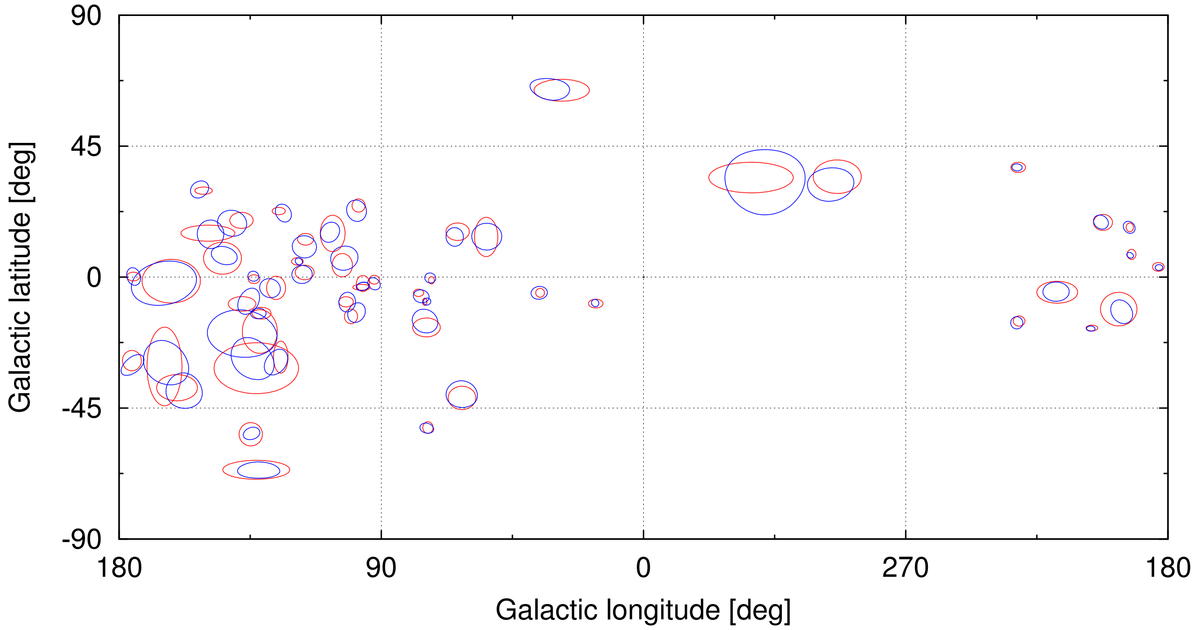

Figure 2.12: The pairs of H I shells (red ellipses) and far-infrared loops (blue ellipses), candidates for counterparts.

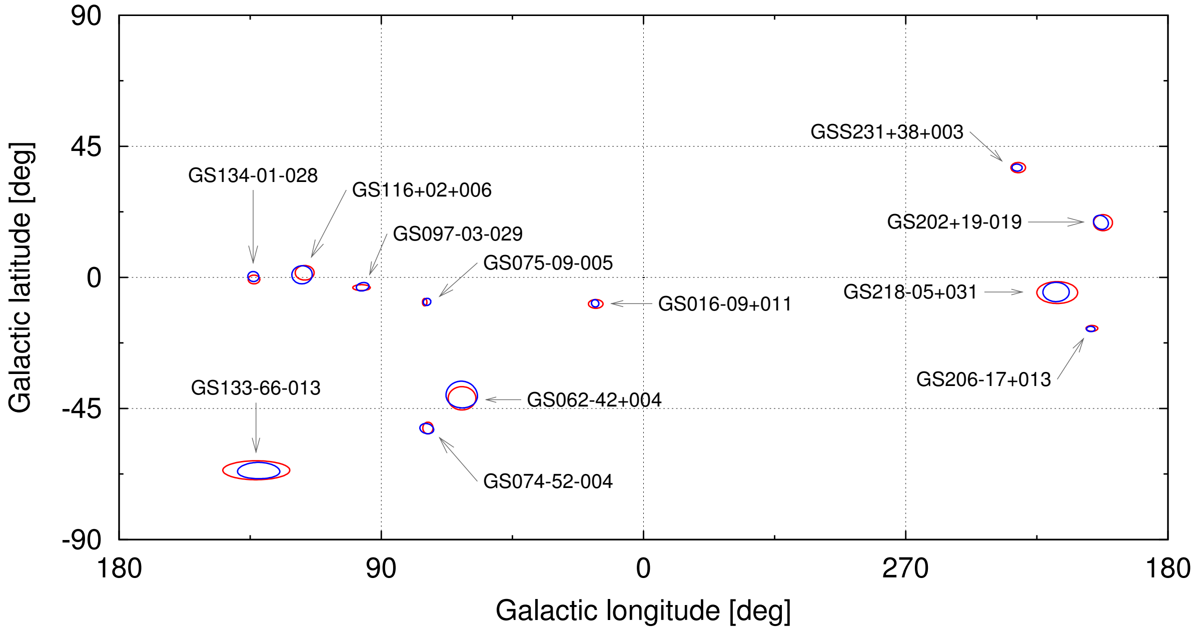

Figure 2.13: The pairs of H I shells (red ellipses) and far-infrared loops (blue ellipses) that were selected for multiwavelength study. The labels with arrows belong to the H I shells. The pairs were selected to cover various positions in the sky.

Table 2.2: Candidate pairs of H I shells–IR loops for counterparts. H I shells selected for multiwavelength study (section 2.3$_{(40)}$) are in boldface. $d_{\mathrm{H\,I}}^{\mathrm{anal}}$ is the shell kinematical distance derived by findcan progam analytically. Note that for some shells it was not possible to determine their kinematical distances. For shells having a counterpart far-infrared loop with known distance—d_{IR}— the kinematical distance—$d_{\mathrm{H\,I}}^{\mathrm{graph}}$— was also determined from the graph **1.4**$_{(15)}$. See discussion in section 2.2$_{(33)}$ for more details.

H I shell	$d_{\mathrm{H\,I}}^{\mathrm{anal}}$ [kpc]	$d_{\mathrm{H\,I}}^{\mathrm{graph}}$ [kpc]	IR loop	d_{IR} [kpc]
GS016-09+011	15.12 | 1.40		GIRL G016-08	
GS028+64-004	36.58		GIRL G032+64	
GS036-05+015	12.73 | 1.17		GIRL G035-05	
GS054+14+018	8.73 | 1.56		GIRL G053+13	
GS062-42+004	9.85 | 0.71		GIRL G062-40	
GS064+16+013	6.29 | 1.50		GIRL G064+13	
GS073-01+007	3.88 | 1.15		GIRL G073-00	
GS074-52-004	8.91		GIRL G074-51	
GS075-17+013	2.38	1.0 | 2.5	GIRL G075-15	0.335
GS075-09-005	5.12	$\leq$ 0.2 | 4.8	GIRL G074-08	0.770
GS077-05+015	1.89		GIRL G076-06	
GS092-01+016			GIRL G092-02	
GS096-02+000			GIRL G096-03	
GS097-03-029	3.97		GIRL G096-03	
GS098+25+004			GIRL G098+22	
GS100-13-038	4.73		GIRL G098-12	
GS102-09-069	7.71		GIRL G101-08	
GS103+04+001			GIRL G102+06	0.620
GS107+15-000	0.03		GIRL G107+15	
GS116+13-114	16.05		GIRL G116+10	
GS116+02+006			GIRL G117+00	2.500
GS119+05-074	7.57		GIRL G118+05	
GS124-27-031	3.37		GIRL G126-29	
GS125+23-016	1.59		GIRL G123+22	
GS126-04-076	8.23		GIRL G128-03	
GS131-12-002	0.20		GIRL G132-12	
GS132-19-051	5.56		GIRL G137-19	
GS133-66-013	7.24		GIRL G132-66	
GS133-31+008			GIRL G134-27	
GS134-01-028	2.42	1.5	GIRL G133+00	2.400
GS135-54-005	1.15		GIRL G134-53	
GS138-09-003	0.21		GIRL G135-08	

(continuing on the next page)

Table 2.2: (continued)

H I shell	$d_{\text{H I}}^{\text{anal}}$ [kpc]	$d_{\text{H I}}^{\text{graph}}$ [kpc]	IR loop	d_{IR} [kpc]
GS138+20-006	0.54		GIRL G141+18	
GS144+07-020	1.84	1.5	GIRL G143+07	0.900
GS150+15-003	0.27		GIRL G148+14	
GS151+30-007	0.86		GIRL G152+30	
GS160-38-002	0.44		GIRL G157-39	
GS162-01-002	0.30		GIRL G164-02	
GS164-31+011			GIRL G164-29	
GS175+00+016			GIRL G175+00	
GS176-29+016			GIRL G175-30	
GS183+03+008	14.69		GIRL G183+03	
GS192+08+008	1.73		GIRL G193+07	
GS193+17-008			GIRL G193+17	
GS197-11-000		< 0.2	GIRL G195-11	0.400
GS202+19-019			GIRL G203+18	0.405
GS206-17+013	1.57	2.0	GIRL G206-17	0.305
GS218-05+031	3.06		GIRL G218-05	
GS231-15+047	4.69		GIRL G231-15	
GS231+38+003	0.36		GIRL G231+37	
GS293+35+001	8.44		GIRL G295+31	
GS323+34-021	2.24 | 14.20	1.5	GIRL G318+32	0.630

2.3 Multiwavelength Study of Selected H I Shells

From the list of H I shell—far-infrared loop pairs of possibly associated counterparts (table **2.2**(38) and figure **2.12**(37)), I have selected twelve H I shells for multiwavelength study (figure **2.13**(37)). These shells were selected from different parts of the sky in order to explore various conditions for the evolution of shells, especially the density and homogeneity of the ambient medium. They also represent all basic types of shells:

- fully enclosed/open,
- with homogenous border/inhomogenous border,
- close to elliptical shape/more deformed,
- with slow/fast expansion,
- with faint/distinct border.

I have preferentially chosen smaller shells because they are more appropriate for detailed study and for searching for their counterparts. The disadvantage of this selection is that they make a bad statistical sample.

Note that all these shells are assumed to be closer than the distance limit defined in the *findcan* program—*thres_hi_dist_cut* parameter. Note also that kinematically derived distances are vague and it is, generally, not a good practice to compare them to other distances without further analysis or discussion.

The images of H I shells are extracted from the large data cube of H I line emission—see section 2.1.1(21). Because the expanding H I shells span three dimensions in this data cube—the longitude, the latitude and the radial velocity—I have prepared their images by averaging the H I emission over several velocity channels centered at the mean radial velocity of particular shells. This practice should highlight the shells and the medium in their vicinity. The interval of velocity channels for averaging was chosen to represent half of the shell's span in the velocity dimension.

For each studied shell, I have prepared multiwavelength images of its vicinity, representing different phases of interstellar medium—see section 1.2.6(16) for an overview. The images are cut from all-sky maps of

- far-infrared continuum emission at 100 μm,
- optical Hα line emisson at 656 nm,
- X-ray continuum emission at 0.25 keV;

and partial-sky maps of

- CO line emission at 2.6 mm.

See section 2.1(21) for desciption of data sources.

If there were any signs of correlation between H I emission and the corresponding image at a different wavelength, I have also prepared composite images of contours overlaid on the H I data. The contours are smoothed to adjust for the lower resolution of H I images.

I have also searched the SIMBAD database[34] for young stellar objects identified in the direction of studied H I shells. These objects could provide valuable kinematical information and, of course, they are a clear sign of ongoing or recent star formation.

Note that images are in galactic coordinates, with the latitude increasing northwards and the longitude increasing eastwards. This implies that when using some standard projection—galactic cartesian[35] in this case—and standard orientation—galactic north pole up, **the east is on the left side** of images, while **the west is on the right side**.

In the analysis of H I shells, I am using the following expressions to describe the nature of their counterparts in this meaning:

diffuse for faint sources covering larger areas, especially for faint dust and Hα emission;

compact for smaller, stronger sources, especially for compact H II regions;

fragment for small fragments of medium, especially molecular clouds and small dust clouds;

filament for filamentary structures, built up from several fragments;

condensation for larger, denser and brighter sources.

The *angular area* of H I shells is provided as a byproduct of the *findcan* program. The expansion velocity—v_{exp}—is simply half the shell extent in velocity dimension; the distance—d—is determined from the graph **1.4**$_{(15)}$, see section 2.2$_{(33)}$ for the discussion on distances; the shell radius—r_{sh}—is equivalent to the shell characteristic length (equation 1.19$_{(13)}$); the local particle density—n_{local}—is obtained from the equation 1.23$_{(14)}$; and the shell embedded energy—E_{tot}—is obtained from Chevalier's formula (equation 1.24$_{(14)}$).

To determine the mean difference brightness temperature used in the equation for local particle density, I have used the following method: For each studied shell, I have measured the brightness temperature in the central hole, then in four points outside the shell (northwards, southeards, eastwards and westwards). $\langle T_{\mathrm{B,i}} \rangle$ is then defined as

$$\langle T_{\mathrm{B,i}} \rangle = \frac{T_1 + T_2 + T_3 + T_4}{4} - T_{\mathrm{hole}}, \tag{2.1}$$

where $T_{1\ldots4}$ are temperatures outside the shell, T_{hole} is the temperature in the centeral hole. The four reference surrounding points should represent the ambient medium, therefore they have been located off the bright pixels showing only local excess in emission.

Basic properties of the studied H I shells are summarized in table **3.1**$_{(90)}$.

---

[34] The SIMBAD database provides basic astronomical data for objects outside the solar system. See the website http://simbad.u-strasbg.fr.

[35] galactic cartesian projection = equirectangular projection with galactic coordinates

2.3.1 GS016-09+011

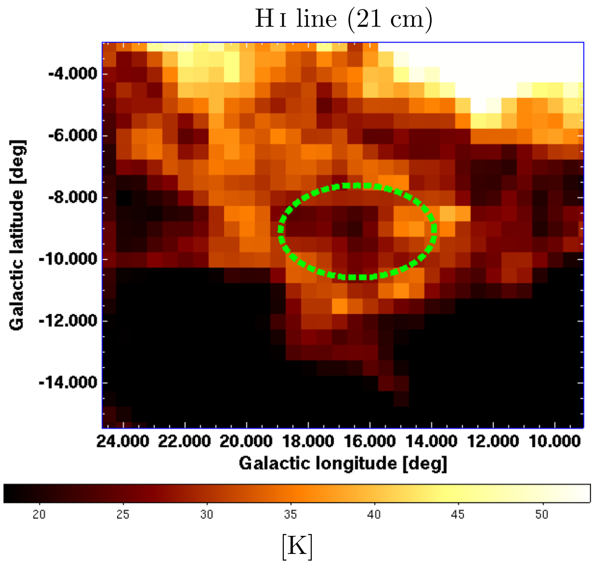

Figure 2.14: *GS016-09+011.* Neutral hydrogen emission with the identified expanding shell (green dashed ellipse).

This H I shell is an example of low-latitude shells, with a hole in its center fully enclosed by a dense wall—see figure **2.14**$_{(42)}$. The shell angular area is $11.6^{\circ 2}$, the kinematical distance is 1 kpc, the radius is 33.6 pc, the local particle density is 0.35 cm^{-2} and the expansion velocity is 4.1 km/s. The estimated embedded energy is relatively low, only about 6.89×10^{48} erg.

The southeastern shell wall is slightly fainter than other parts, which indicates that a break out may evolve here in the future.

Counterpart infrared emission (figure **2.15a**$_{(44)}$ and **2.16a**$_{(45)}$) The counterpart IR emission reveals a broken, slightly fragmented dust wall in the southwestern[36] direction and a hole in the center.

Counterpart Hα emission (figure **2.15b**$_{(44)}$ and **2.16b**$_{(45)}$) The counterpart Hα emission around the central hole is diffuse with a topology similar to the topology of dust. The border is apparently open in the southwestern direction from the center too.

Counterpart X-ray emission X-rays show faint increase of intensity in the central part of the shell, that does not differ significantly from the surroundings.

Summary Both infrared and Hα emission show central hole apparently associated with the H I hole. No distinct features in X-rays possibly associated with the shell are present. No catalogued young stellar objects in the direction of the shell were found. Radio data of the CO line are not available.

With the kinematical distance of 1 kpc and the galactic latitude of -9.1°, the shell is expanding inside the Galactic disc. While the H I emission shows fully enclosed homogenous border, infrared and Hα emission show an open border. Considering the low latitude—where the medium is abundant and rich in features—we are probably observing overlapping structures. The larger structure surrouding the central hole with an open border may

---

[36] Note again that the galactic longitude is measured eastwards, what means that—assuming the standard orientation of image—**east is on the left** while **west is on the right** side of the image!

not be associated with the H I shell, while the smaller and fainter structure consisting of fragmented dust aroung the hole may be associated with the shell.

(a) IR continuum (100 μm)

(b) Hα line (656 nm)

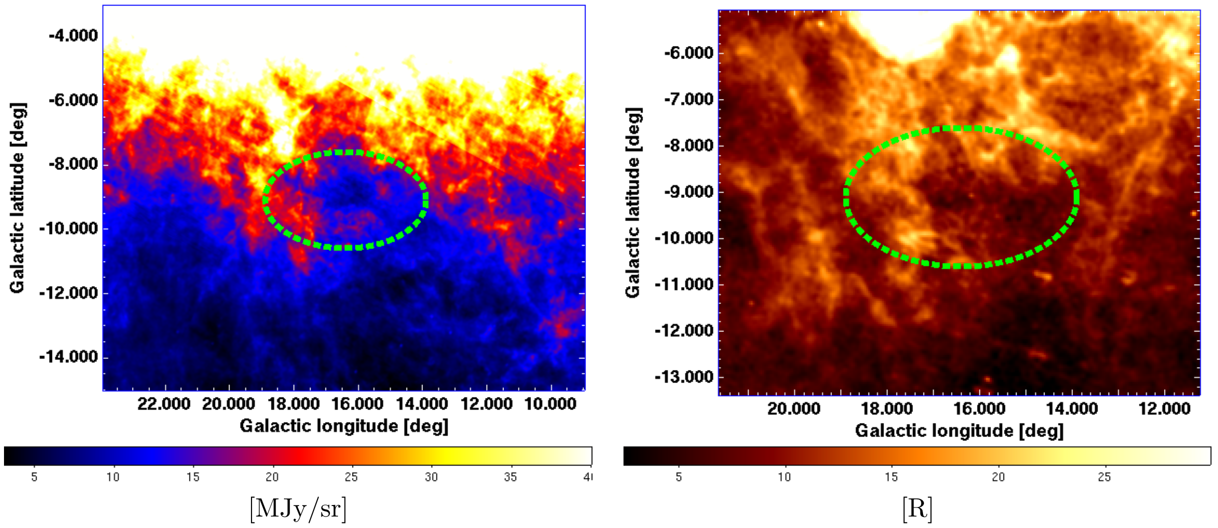

(c) X-ray continuum (0.25 keV)

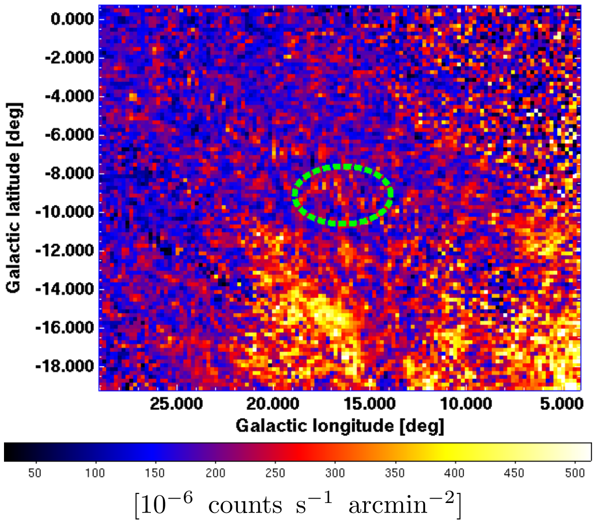

Figure 2.15: *GS016-09+011.* Multiwavelength images of the vicinity of the H I shell. (green dashed ellipse).

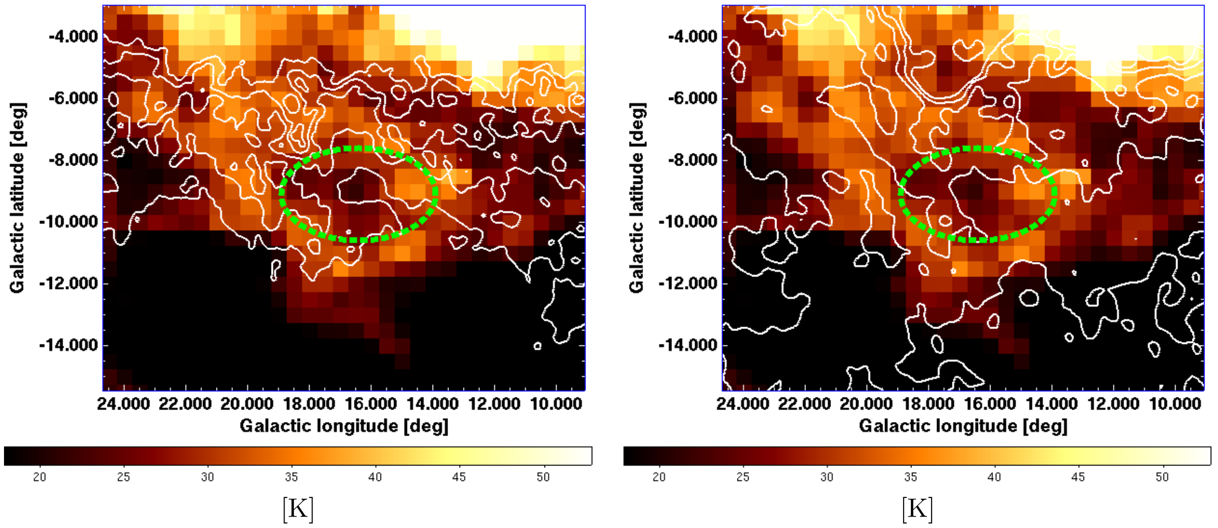

(a) background: H I line (21 cm)
contours: IR continuum (100 μm)

(b) background: H I line (21 cm)
contours: Hα line (656 nm)

Figure 2.16: *GS016-09+011.* Contours of various wavelengths overlaid on the neutral hydrogen emission, with the identified H I shell (green dashed ellipse).

2.3.2 GS062-42+004

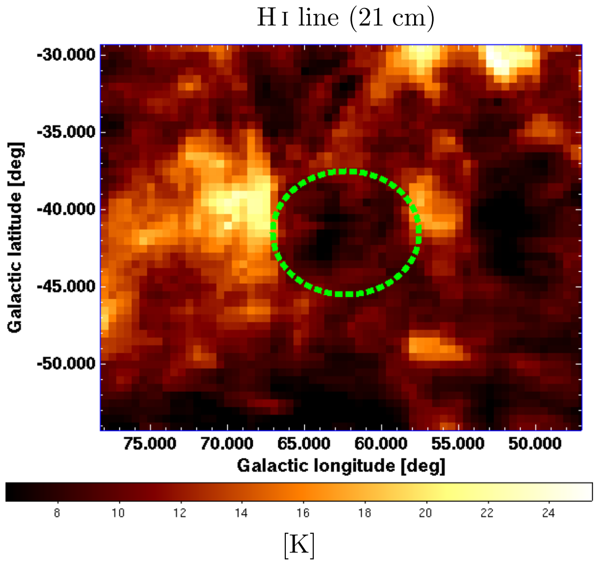

Figure 2.17: *GS062-42+004*. Neutral hydrogen emission with the identified expanding shell (green dashed ellipse).

This shell is an example of mid-latitude shells with strongly nonuniform borders—see figure **2.17**$_{(46)}$. There are two distinct bright areas—larger in the eastern border and smaller in the western border. The excess in H I emission may be the result of several nearby expanding shells that have caused the medium to collect in these areas—see the holes around. The collection process and collisions of several shock fronts of expanding shells would also make the H I transition probability higher, resulting in increased emission.

The expansion velocity of the shell is 8.8 km/s, the angular area is $44.7^{\circ 2}$. Its kinematical distance is ambiguous: either 0.4 kpc or 4.5 kpc, which results in ambiguous shell radius 26.3 or 296.2 pc, particle density 1.60 or 0.14 cm^{-3} and embedded energy 5.07×10^{49} or 6.41×10^{51} erg. If the shell is closer (0.4 kpc) it would be expanding in the southern part of the Galactic disc. If the shell is farther (4.5 kpc) it would be expanding below the Galactic disc.

Counterpart infrared emission (figure **2.18a**$_{(48)}$ and **2.19a**$_{(49)}$) The counterpart infrared emission (figure **2.18a**$_{(48)}$) shows structure very similar with the H I line emission: a hole inside bordered by two clouds of condensed medium. There are also smaller fragments found along the shell border, especially along the southern part.

Counterpart Hα emission (figure **2.18b**$_{(48)}$ and **2.19b**$_{(49)}$) Hα emission reveals one distinct H II region in the southeast border indicating advanced star formation, but no catalogued young stellar object is here. Note that the Hα hot spot in the southwest part of the shell's interior is, probably, an observation artefact.

Counterpart X-ray emission (figure **2.18c**$_{(48)}$ and **2.19c**$_{(49)}$) Diffuse X-ray emission obviously correlates negatively with both H I line (figure **2.19c**$_{(49)}$) and infrared emission. The most intensive is in directions where no dust or neutral gas is observed, especially in the nearby area beyond the western dust-gas condensation.

Summary The X-ray emission is apparently filling the shell interior. This is probably an example of the shadowing effect. Assuming the shell is close (0.4 kpc), it would represent a foreground object with respect to the Galactic halo. Then it will result in the observed correlation between the soft X-ray diffuse background and the emission of dust and gas, because the dust and gas would absorb incoming X-rays. Note that not only the shell itself but also the medium in its vicinity is shadowing.

The only observed Hα structure is a compact region with no obvious counterparts in other multiwavelength images. No young stellar objects were found in SIMBAD and CO radio data are not available for this region.

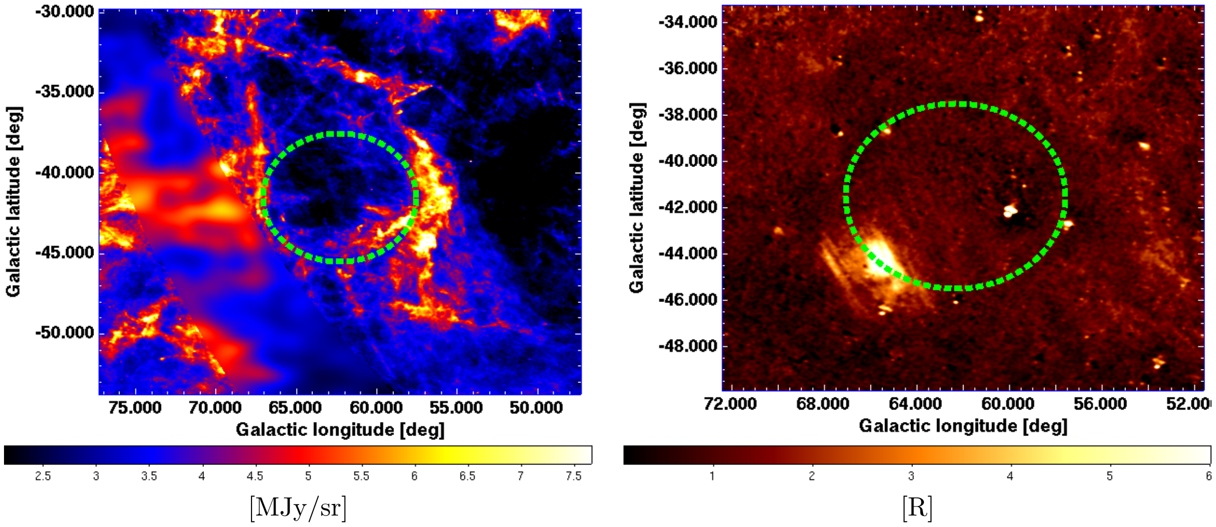

(a) IR continuum (100 µm)

(b) Hα line (656 nm)

(c) X-ray continuum (0.25 keV)

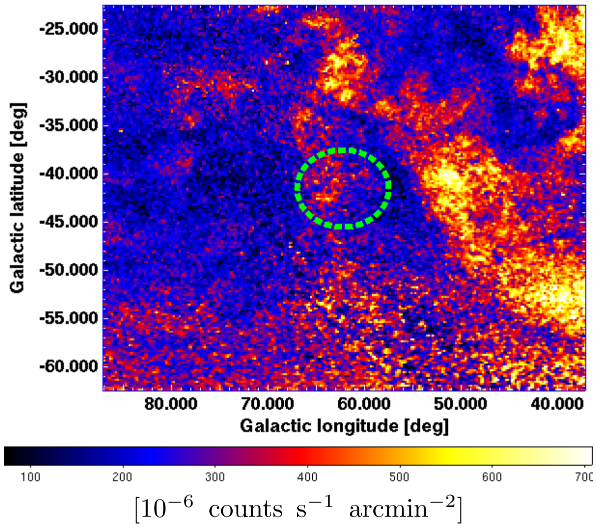

Figure 2.18: *GS062-42+004*. Multiwavelength images of the vicinity of the H I shell. (green dashed ellipse).

(a) background: H I line (21 cm)
contours: IR continuum (100 µm)

(b) background: H I line (21 cm)
countours: Hα line (656 nm)

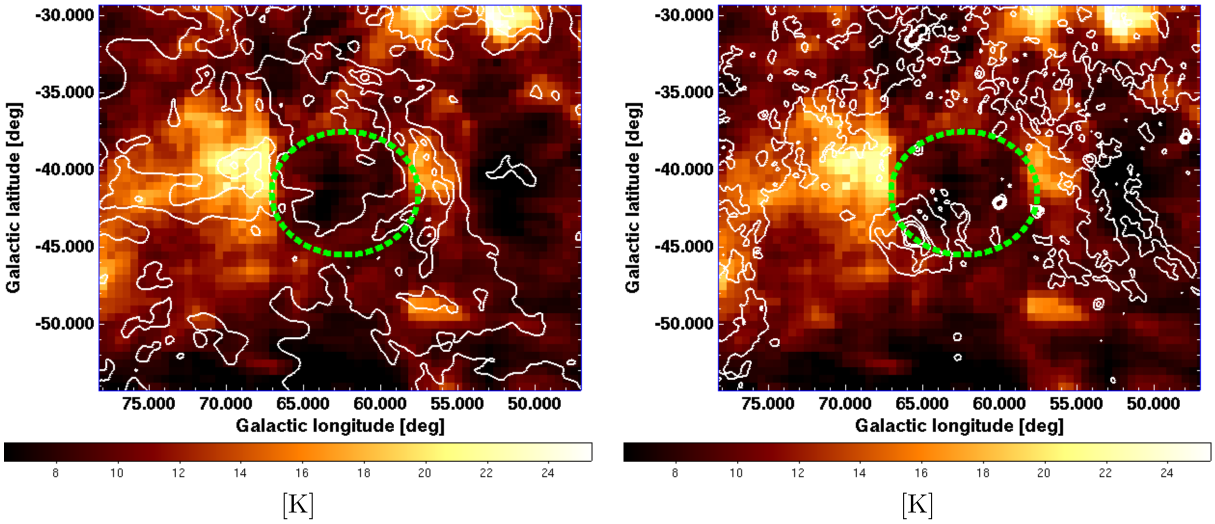

(c) background: H I line (21 cm)
contours: X-ray continuum (0.25 keV)

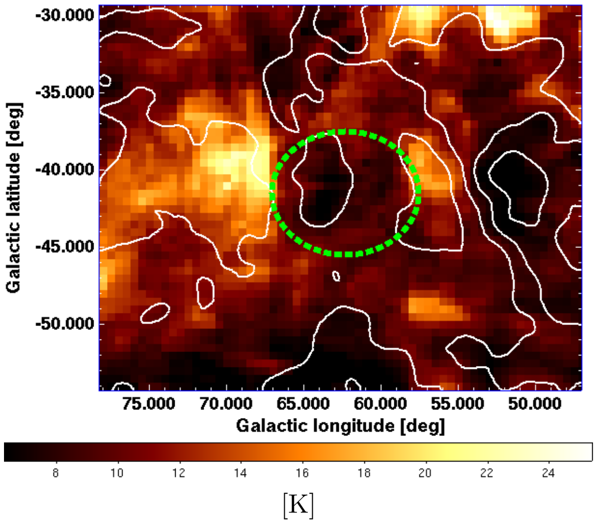

Figure 2.19: *GS062-42+004*. Contours of various wavelengths overlaid on the neutral hydrogen emission, with the identified H I shell (green dashed ellipse).

2.3.3 GS074-52-004

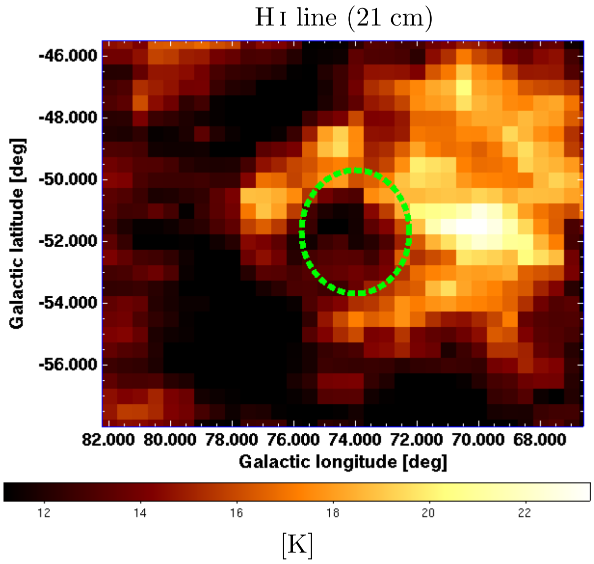

Figure 2.20: *GS074-52-004*. Neutral hydrogen emission with the identified expanding shell (green dashed ellipse).

This shell is another example of mid-latitude shells with open borders. H I emission reveals a gap in the southeastward direction (figure **2.20**$_{(50)}$), a possible way for its content to escape. The expansion velocity of the shell is 7.4 km/s, angular area is about $6.8^{\circ 2}$, and the ambiguous kinematical distance is either ≤ 0.1 kpc or 3.0 kpc. It the latter case—distance of 3.0 kpc—the shell would be expanding below the Galactic disc in a medium with the density of about $0.34\ \mathrm{cm}^{-3}$. The shell diameter would be 77.1 pc and the energy 1.93×10^{50} erg. In the former case—distance of ≤ 0.1 kpc—the shell would be located inside the Galactic disc, near the Solar system and may be in touch with the Local Hot Bubble. The density of the ambient medium was determinend to be about $10.16\ \mathrm{cm}^{-3}$, the diameter of 2.6 pc and the energy of 2.15×10^{47} erg.

Counterpart infrared emission (figure **2.21a**$_{(51)}$ and **2.22a**$_{(52)}$) Counterpart infrared emission shows nearly the same topology as H I emission and reveals fragments of various sizes aroung the central hole.

Counterpart Hα emission (figure **2.21b**$_{(51)}$ and **2.22b**$_{(52)}$) There is one compact H II region inside the shell, shifted slightly in the northeastward direction from the center. Also several other, small H II regions are observed eastwards from the shell. Large region with diffuse Hα emission is apparently touching the eastern border of the shell.

Counterpart X-ray emission (figure **2.21c**$_{(51)}$ **2.22c**$_{(52)}$) There is a well distinguished structure in the X-ray emission negatively correlating with dust and gas emission. This is probably another example of the shadowing effect caused by absorption of the soft X-ray diffuse radiation in the foreground medium.

Summary There is a distinct correlation between the soft X-ray diffuse background emission and the emission of dust and gas. The Hα emission seems not to be correlated neither with neutral hydrogen or dust. No SIMBAD young stellar objects are present in the direction of the shell. CO radio emission is not available for this region.

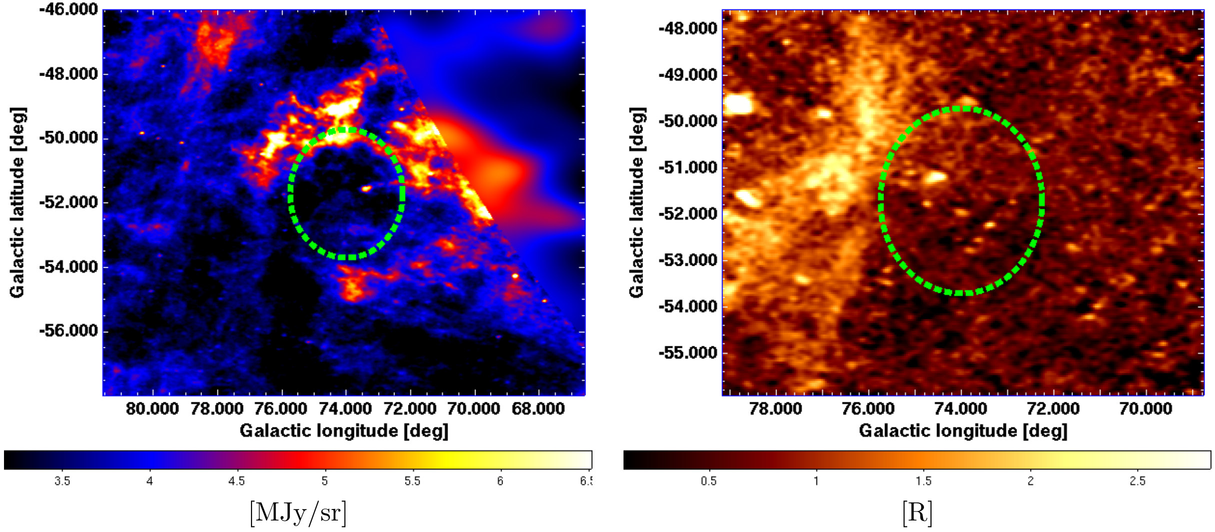

(a) IR continuum (100 µm)

(b) Hα line (656 nm)

(c) X-ray continuum (0.25 keV)

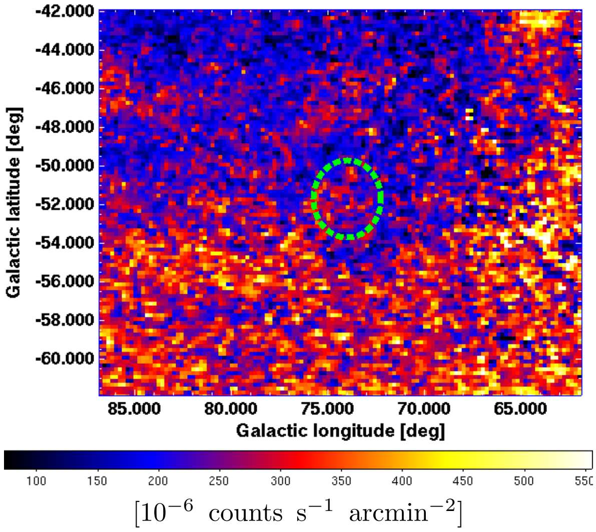

Figure 2.21: *GS074-52-004*. Multiwavelength images of the vicinity of the H I shell. (green dashed ellipse).

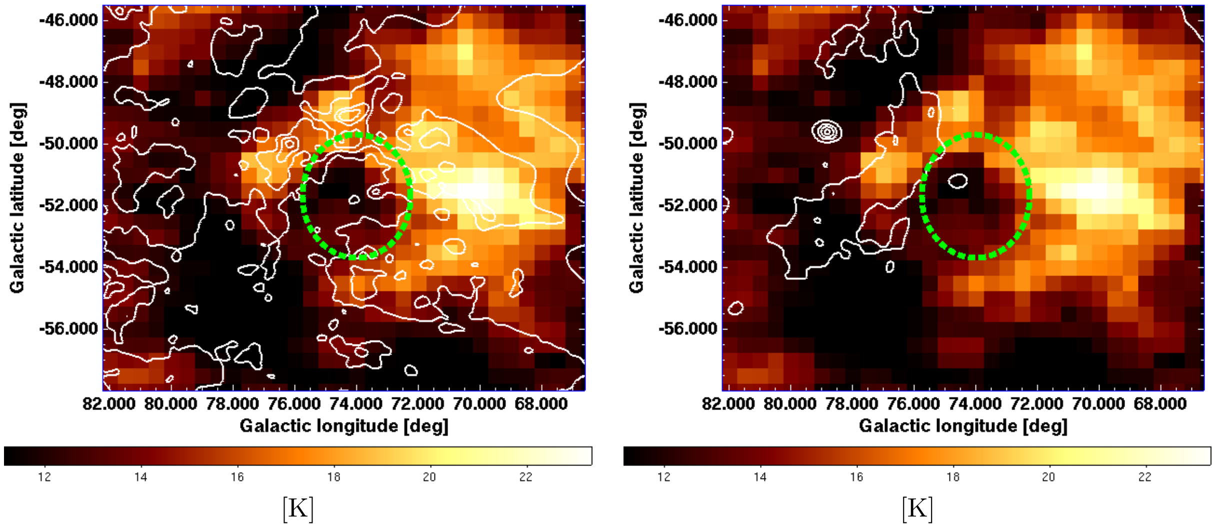

(a) background: H I line (21 cm)
contours: IR continuum (100 µm)

(b) background: H I line (21 cm)
countours: Hα line (656 nm)

(c) background: H I line (21 cm)
contours: X-ray continuum (0.25 keV)

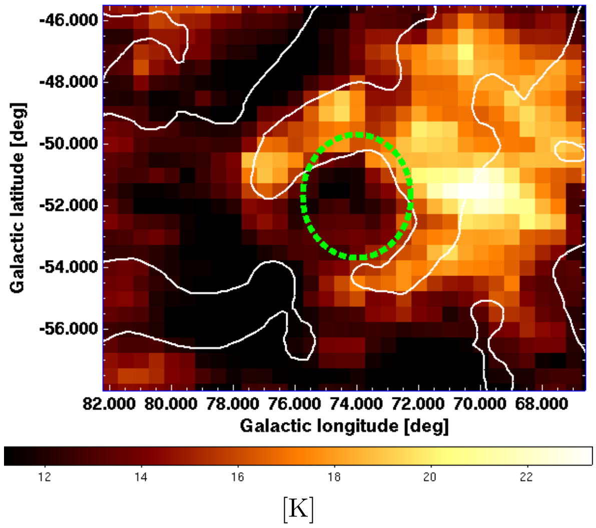

Figure 2.22: *GS074-52-004*. Contours of various wavelengths overlaid on the neutral hydrogen emission, with the identified H I shell (green dashed ellipse).

2.3.4 GS075-09-005

This shell is one of the smallest shells from the catalogue, having an angular area of only about $2.9^{\circ 2}$. Its expansion velocity is 9.3 km/s and its ambiguous kinematical distance is either ≤ 0.2 kpc or 4.9 kpc. In the former case—distance of ≤ 0.2 kpc—the shell would be located in the Galactic disc, in a medium with density of 6.02 cm^{-3}. Its radius would be 3.4 pc and embedded energy about 3.91×10^{47} erg. In the latter case—distance of 4.9 kpc—the shell would be located at the edge of the Galactic disc, in a medium with density of 0.25 cm^{-3}. Its radius would be 82.3 pc and embedded enegy about 2.34×10^{50} erg.

The shell is located in the direction of the *Cygnus Loop*, a supernova remnant. The distance to the Cygnus Loops was determined by Minkowski (1958) to be about 770 pc, but latter studies have revealed that the remnant is closer. Blair et al. (1999) determined the distance to be 440^{+130}_{-100} pc.

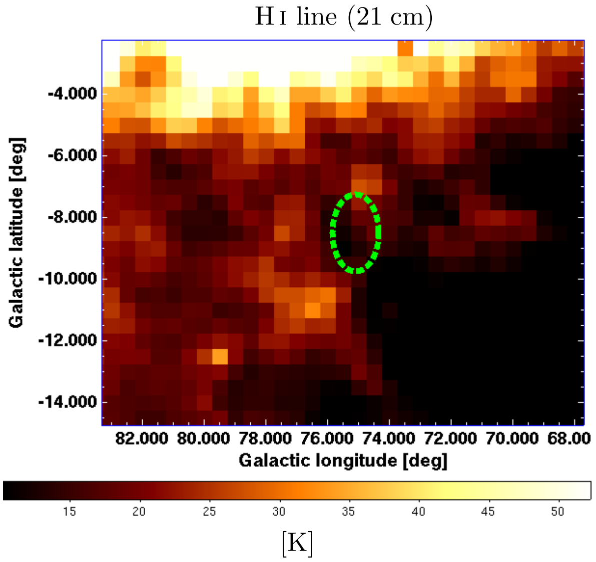

Figure 2.23: *GS075-09-005.* Neutral hydrogen emission with the identified expanding shell (green dashed ellipse).

Counterpart infrared emission (figure **2.24a**$_{(55)}$ and **2.25a**$_{(56)}$) Infrared emission of the region shows long filament of dust located along the eastern border. Western part is open.

Counterpart Hα emission (figure **2.24b**$_{(55)}$ and **2.25b**$_{(56)}$) Hα emission reveals the shape of the Cygnus Loop. The loop is open in the soutwestward direction and the H I shell is located on its eastern part. Note that Hα emission of the eastern part of the Cygnus Loop is available only in lower spatial resolution.

Counterpart X-ray emission (figure **2.24c**$_{(55)}$ and **2.25c**$_{(56)}$) X-ray emission shows clearly the shape of the Cygnus Loop and reveals significantly stronger intensity from the eastern part, where the H I shell is apparently located.

Counterpart CO emission (figure **2.24d**$_{(55)}$) Counterpart CO emission shows no correlation with the H I shell. No molecular clouds are found near the eastern part of the Cygnus Loop. The dark spherical hole in the center of the shell is probably an observational artifact.

Summary This shell is probably connected to the Cygnus Loop, a supernova remnant, observed in both Hα and X-ray emission. Infrared emission shows only a partial arc. CO emission shows no distinct features near the shell. No catalogued young stellar objects have been found in SIMBAD.

(a) IR continuum (100 μm) **(b)** Hα line (656 nm)

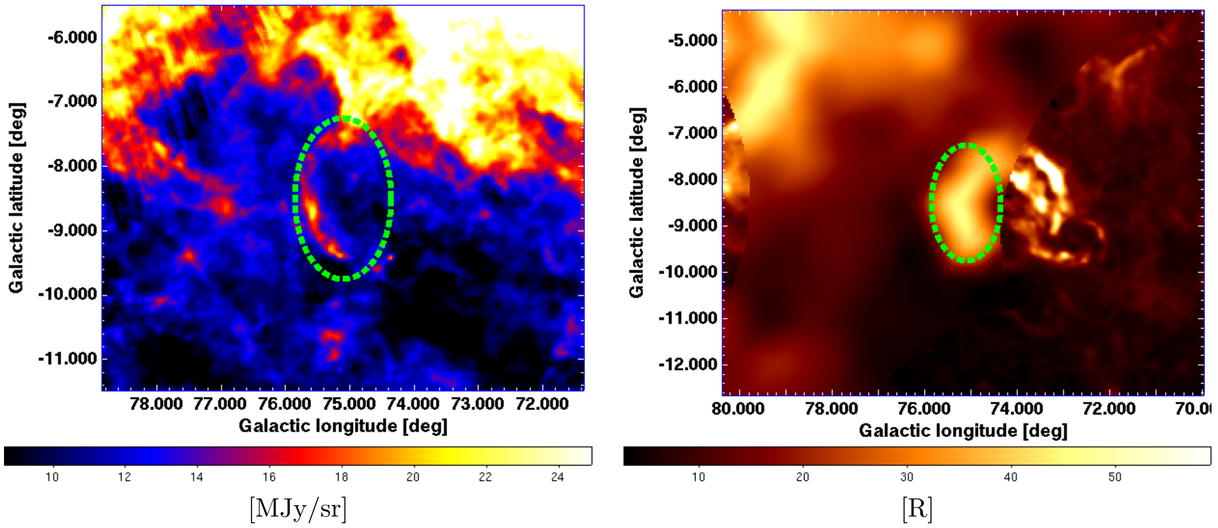

(c) X-ray continuum (0.25 keV) **(d)** CO line (2.6 mm)

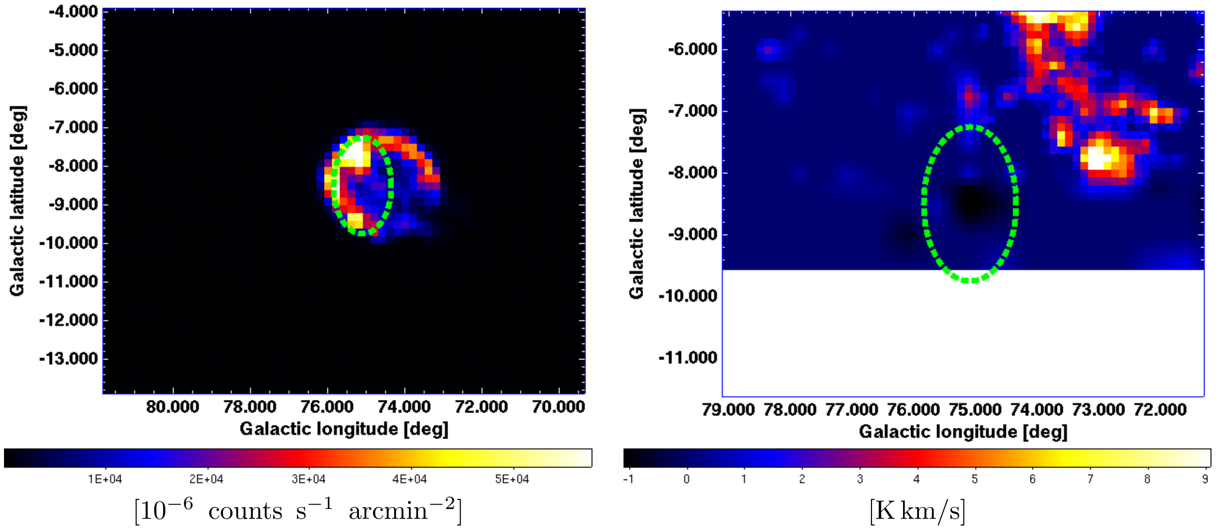

Figure 2.24: *GS075-09-005*. Multiwavelength images of the vicinity of the H I shell. (green dashed ellipse).

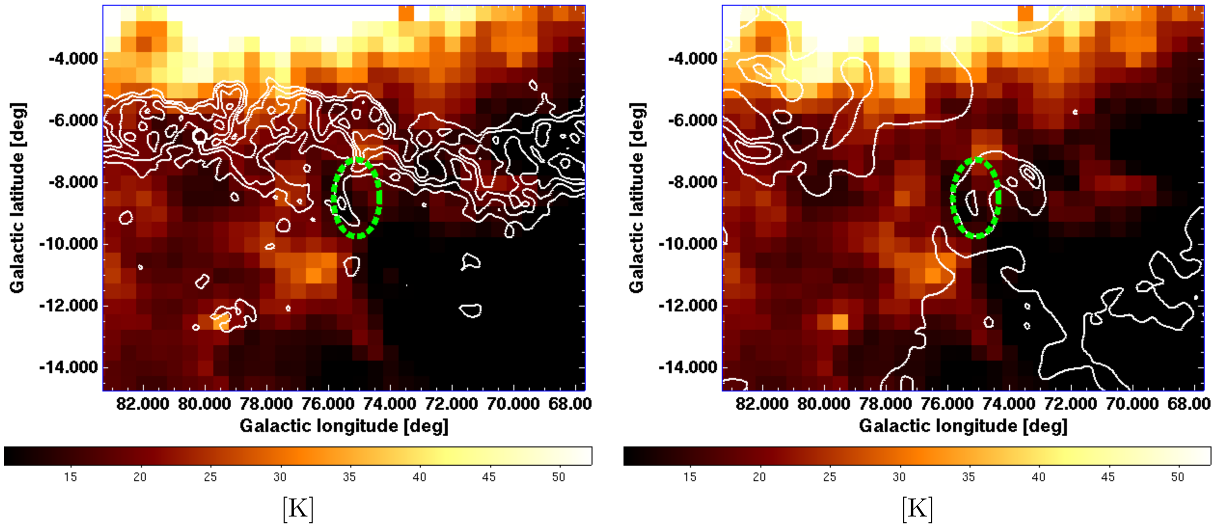

(a) background: H I line (21 cm) contours: IR continuum (100 µm)

(b) background: H I line (21 cm) countours: Hα line (656 nm)

(c) background: H I line (21 cm) contours: X-ray continuum (0.25 keV)

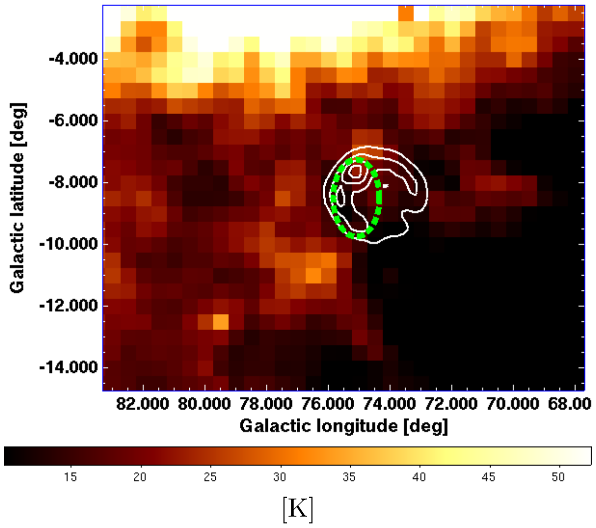

Figure 2.25: *GS075-09-005.* Contours of various wavelengths overlaid on the neutral hydrogen emission, with the identified H I shell (green dashed ellipse).

2.3.5 GS097-03-029

This H I shell (figure **2.26**$_{(57)}$) is an example of shells with highly elongated shape. It is located in the southern part of the Galactic disc, expanding with a velocity of 13 km/s. Its angluar area is $9.4^{\circ 2}$ and the corresponding kinematical distance is about 2.1 kpc. The shell radius is 63.4 pc, the density of ambient medium is about $1.80\ \mathrm{cm}^{-3}$ and the total embedded energy 1.54×10^{51} erg.

The shell is elongated in the longitudinal direction with the central hole shifted westwards from the center. In the north, the shell is bordered by a condensation of neutral medium.

Counterpart infrared emission (figure **2.27a**$_{(58)}$ and **2.28a**$_{(59)}$) The infrared emission shows no obvious counterpart structure, but there are several dust fragments located in the northern and western border and a faint hole inside the shell with a shape similar to that of the H I shell.

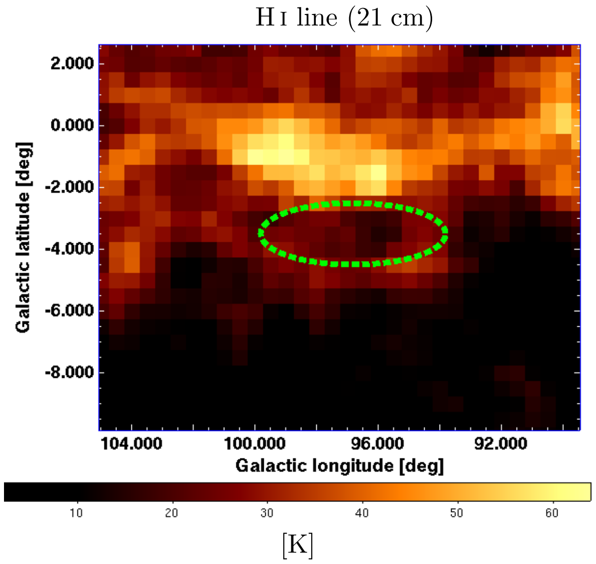

Figure 2.26: *GS097-03-029.* Neutral hydrogen emission with the identified expanding shell (green dashed ellipse).

Counterpart Hα emission (figure **2.28b**$_{(59)}$ and **2.28b**$_{(59)}$) There are two distinct H II regions near the norhern border of H I shell. The inner part of the shell shows slight depression in the Hα emission, but it is not clear if it is connected to the H I shell. A drop-like diffuse prominence penetrated the northern border.

Counterpart X-ray emission (figure **2.27c**$_{(58)}$) X-ray emission shows no correlation with H I emission. This indicates no hot gas in the vicinity and strong absorption of the X-ray emission from the halo.

Counterpart CO emission (figure **2.27d**$_{(58)}$ and **2.28c**$_{(59)}$) Counterpart CO emission reveals several condensations of molecular clouds, mainly around the northern and western border of the H I shell.

Summary In this case, there are no obvious features observed in multiwavelength images. However the shape of the H I shell is irregular, which could be the result of dynamical processes in its environment. Moreover, the shell is obviously expanding in an inhomogenous medium (see figure **2.26**$_{(57)}$). These two factors—external forces and medium inhomogenity—could have led to distortion of the original spherical shape.

(a) IR continuum (100 µm) **(b)** Hα line (656 nm)

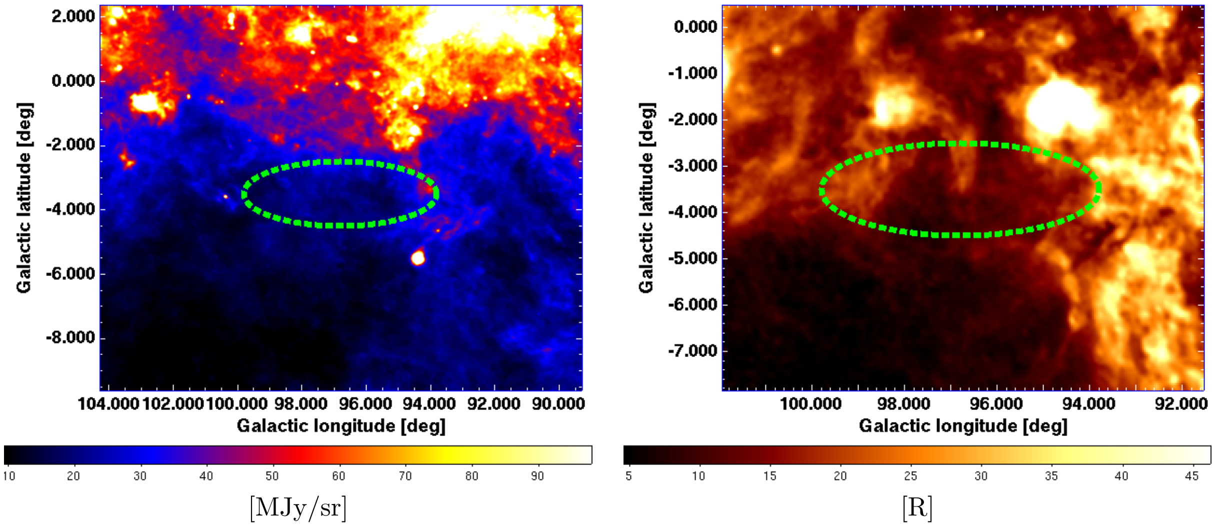

(c) X-ray continuum (0.25 keV) **(d)** CO line (2.6 mm)

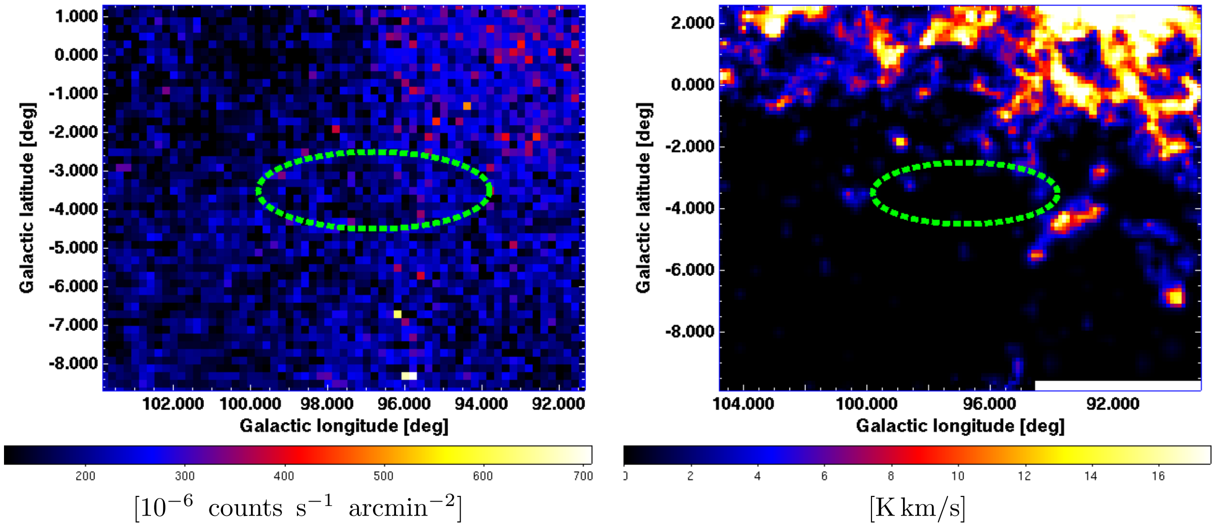

Figure 2.27: *GS097-03-029.* Multiwavelength images of the vicinity of the H I shell. (green dashed ellipse).

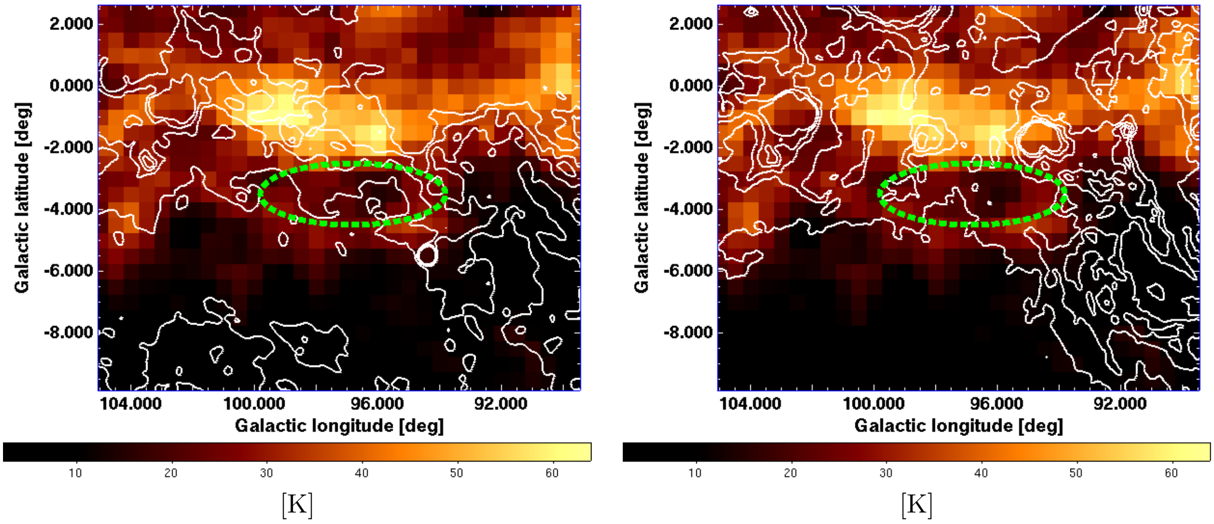

(a) background: H I line (21 cm)
contours: IR continuum (100 µm)

(b) background: H I line (21 cm)
countours: Hα line (656 nm)

(c) background: H I line (21 cm)
contours: CO line (2.6 mm)

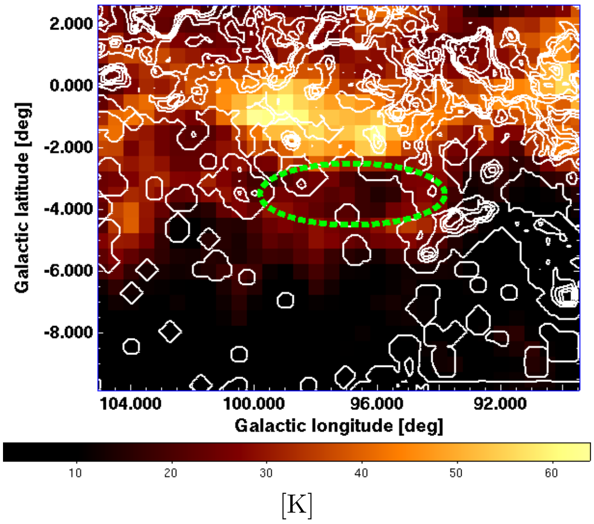

Figure 2.28: *GS097-03-029.* Contours of various wavelengths overlaid on the neutral hydrogen emission, with the identified H I shell (green dashed ellipse).

2.3.6 GS116+02+006

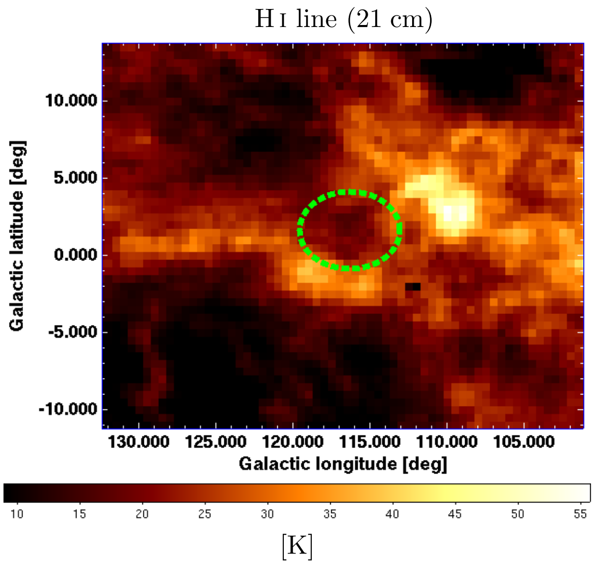

Figure 2.29: *GS116+02+006.* Neutral hydrogen emission with the identified expanding shell (green dashed ellipse).

This H I shell is located in the Galactic disc and with its mean radial velocity, 6.3 km/s, it is an example of a H I region with peculiar motion with respect to the Galactic rotation. Thus, it is not possible to determine the kinematical distance and other properties derived from it. The shell is expanding with velocity 5.2 km/s; its angular area is $25.5^{\circ 2}$.

The central hole is rather spherical, while the borders are inhomogenous, open in the northeastward and southwestward direction.

The distance of the counterpart far-infrared loop, GIRL G117+00, is catalogued as 2.5 kpc.

Counterpart infrared emission (figure **2.30a**(62) and **2.31a**(63)) The infrared emission shows abundace of dust fragments arranged along the borders of the H I shell and outside. The central hole is slightly shifted eastwards. Two large condensations are bordering with the shell. One is located in the northeastward direction and the second in partially surrounding the shell from the east.

Counterpart Hα emission (figure **2.30b**(62) and **2.31b**(63)) There are many compact H II regions of various sizes around the H I shell. They are predominantly located in the areas occupied by large dust condensations, making possible heating sources of the ambient dust.

Counterpart X-ray emission (figure **2.30c**(62)) X-ray emission shows no obvious counterpart features. The apparent line of increased intensity pervading the hole image may be an observational artifact.

Counterpart CO emission (figure **2.30d**(62) and **2.31c**(63)) CO emission reveals abundant fragments and filaments of molecular gas in the vicinity of the shell. They are located especially along the northern and western borders.

Young Stellar Objects (figure **2.32**(64)) There are two young stellar objects discovered in the direction of the H I shell, located apparently in its borders: *CPM 1* (IRAS 00211+6549) and *CPM 40* (IRAS 23390+6524). The kinematic measurements of CPM 40 are not available. The kinematics of CPM 1, by Wouterloot et al. (1993), are: distance 7.1 kpc, radial velocity (from CO measurements) −68.6 km/s. This implies that the CPM 1 is not associated with the H I shell.

Summary Because the H I shell is located in the Galactic disc, there are many objects and features, often overlapping, observed on the multiwavelength images, but association of these features with the shell is not clear.

The dust emission is here well correlated with the Hα emission from H II regions, suggesting that these H II regions act as heating sources of the ambient dust.

Out of two young stellar objects found apparently in the walls of H I shell, one is kinematically far, and one is catalogued without radial velocity or distance measurements.

(a) IR continuum (100 μm)

(b) Hα line (656 nm)

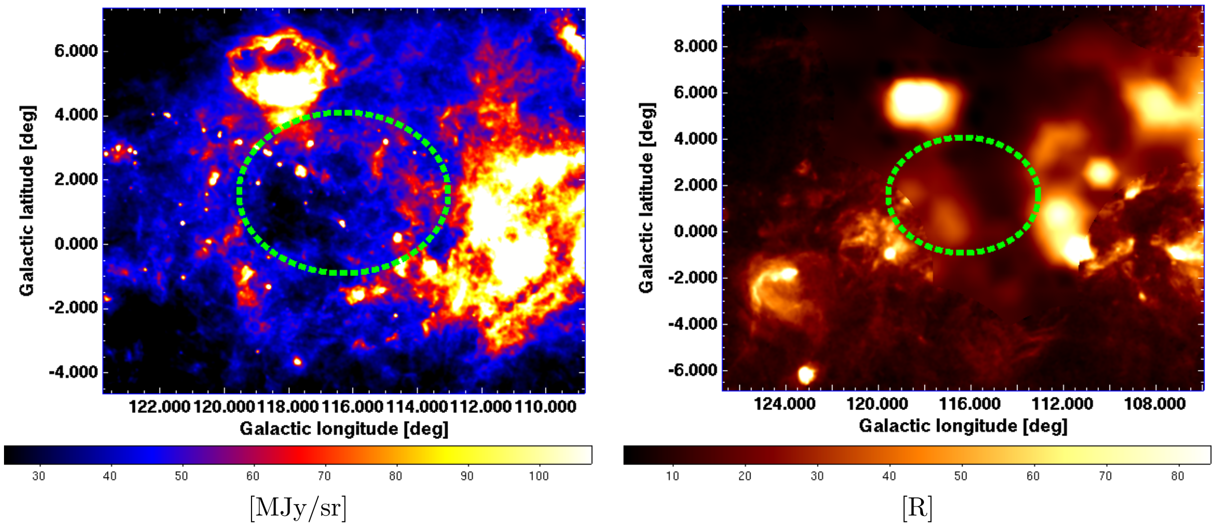

(c) X-ray continuum (0.25 keV)

(d) CO line (2.6 mm)

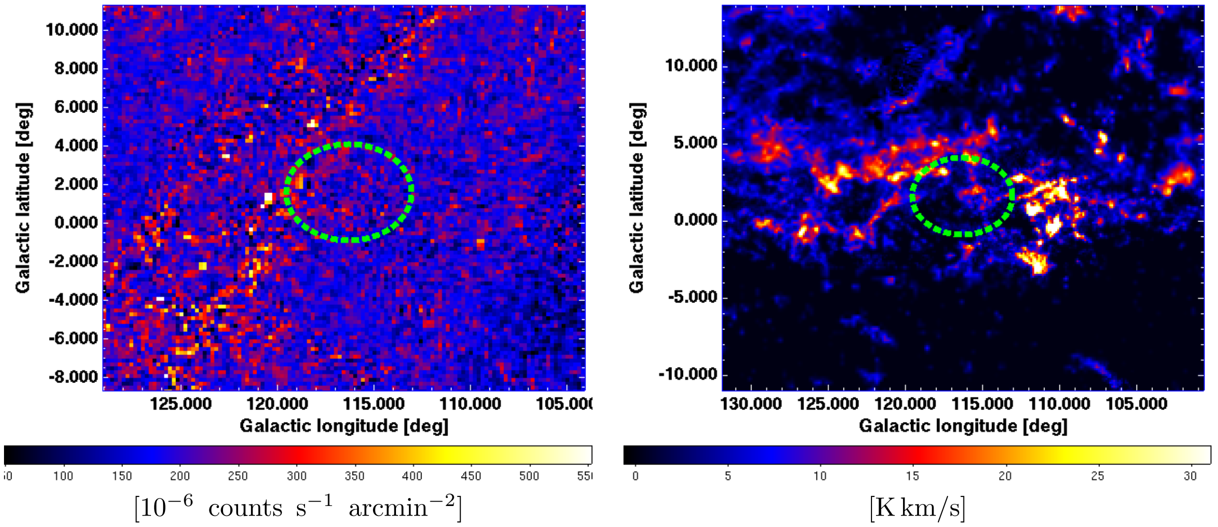

Figure 2.30: *GS116+02+006.* Multiwavelength images of the vicinity of the H I shell. (green dashed ellipse).

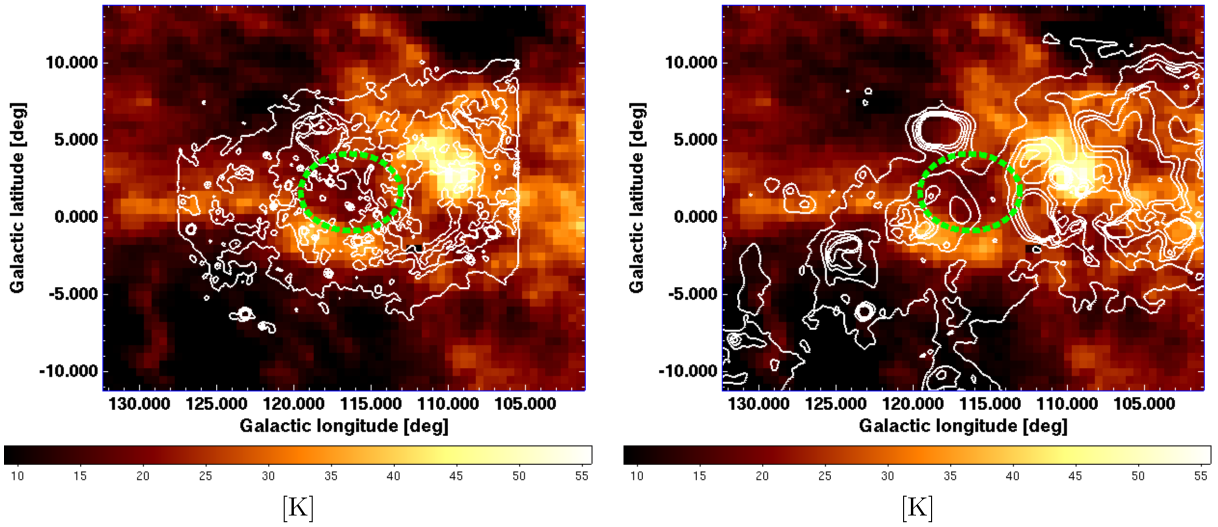

(a) background: H I line (21 cm) contours: IR continuum (100 μm)

(b) background: H I line (21 cm) countours: Hα line (656 nm)

(c) background: H I line (21 cm) contours: CO line (2.6 mm)

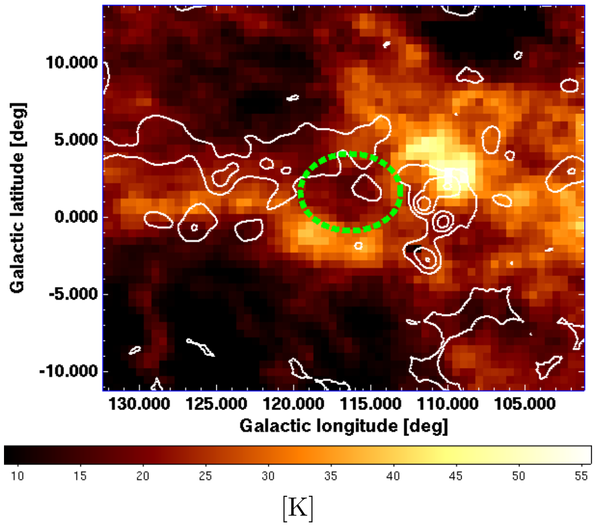

Figure 2.31: *GS116+02+006.* Contours of various wavelengths overlaid on the neutral hydrogen emission, with the identified H I shell (green dashed ellipse).

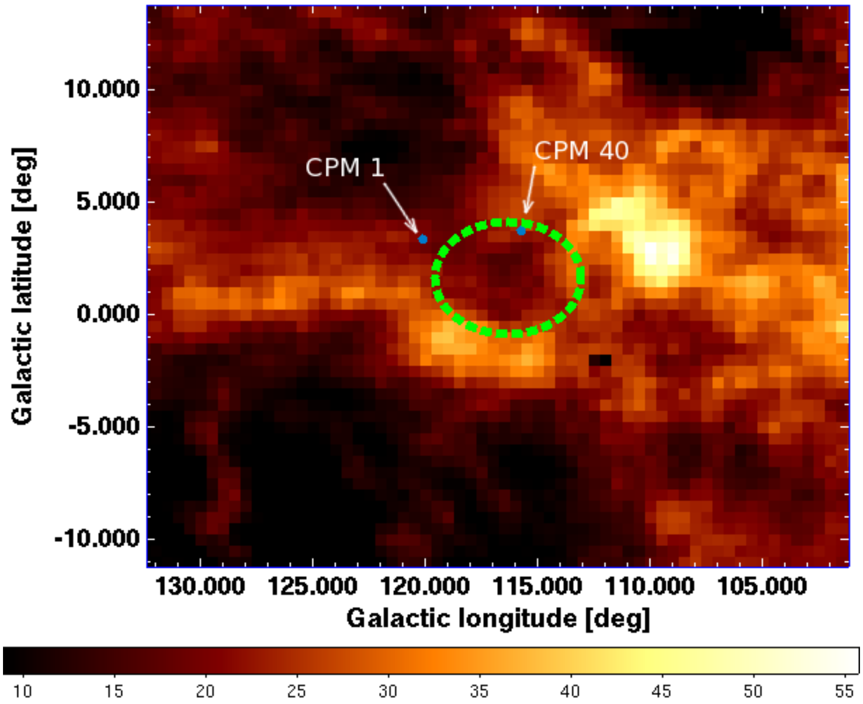

Figure 2.32: *GS116+02+006*. Young stellar objects (blue points) in the direction of the H I shell (green dashed ellipse).

2.3.7 GS133-66-013

This shell is an example of high-latitude shells. Its expansion velocity is 9.3 km/s, angular area is $47.4^{\circ 2}$ and kinematical distance is about 0.4 kpc. The shell is located near the southern edge of the Galactic disc, in a medium with particle density of $0.90\ \mathrm{cm}^{-3}$. The shell radius is 27.1 pc and the embedded energy 3.13×10^{49} erg.

The shell consists of a hole fully enclosed by the wall. There is a region of increased intensity in the southern part of the wall indicating a condensation of neutral material. The shell is expanding in a larger region of accumulated neutral hydrogen spanning between the longitude 80 and 160°, around the radial velocity of -10 km/s.

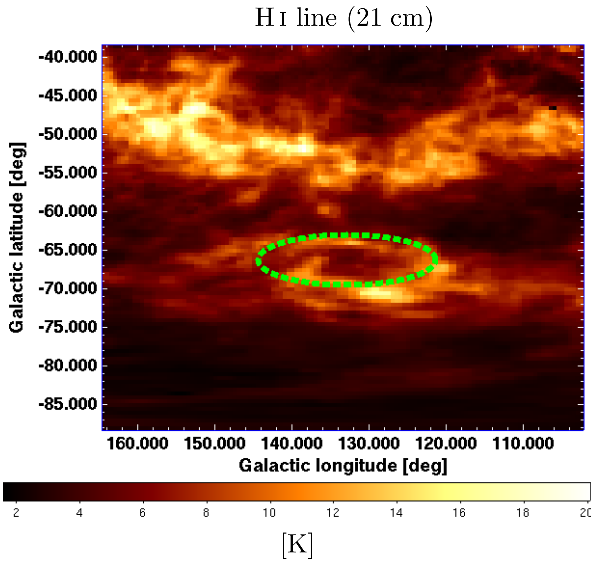

Figure 2.33: *GS133-66-013.* Neutral hydrogen emission with the identified expanding shell (green dashed ellipse).

Counterpart infrared emission (figure **2.34a**(66) and **2.34a**(66)) Infrared emission shows that dust is distributed similary to the neutral hydrogen. There is large a dust condensation along the southern border and a smaller one is in the northern border. Several fragments are located outside the west border.

Counterpart Hα emission (figure **2.34b**(66) and **2.34b**(66)) Hα emission reveals a large, but faint area of ionized hydrogen, touching the southern border of the shell. Very faint increase in intensity is present around the rest of the shell's border.

Counterpart X-ray emission (figure **2.34c**(66) and **2.34c**(66)) X-ray emission is well negatively correlated with the H I emission, clearly observable on the H I image with X-ray contours (figure **2.35c**(67)). There is a weakly increased emission in the center of the shell and a more obvious depression in the shell's border.

Summary Counterparts of both infrared dust emission and hot gas X-ray emission are observable. The Hα line shows only unclear and faint increase in intensity along the shell's borders and one large H II region. No catalogued young stellar objects in the direction of the shell were found in SIMBAD. CO emission is not available in this region.

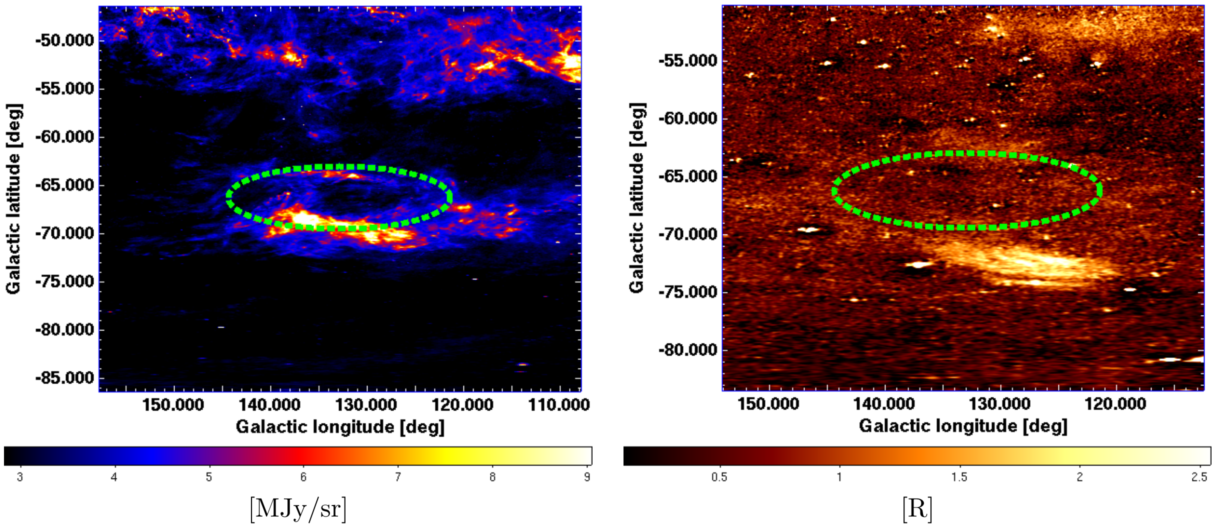

(a) IR continuum (100 µm)

(b) Hα line (656 nm)

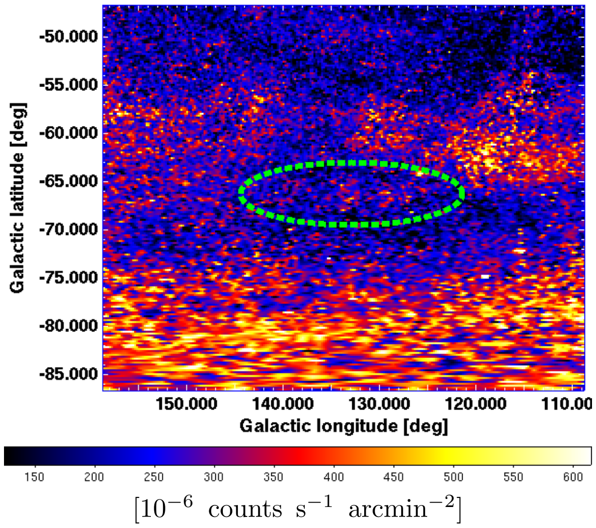

(c) X-ray continuum (0.25 keV)

Figure 2.34: *GS133-66-013.* Multiwavelength images of the vicinity of the H I shell. (green dashed ellipse).

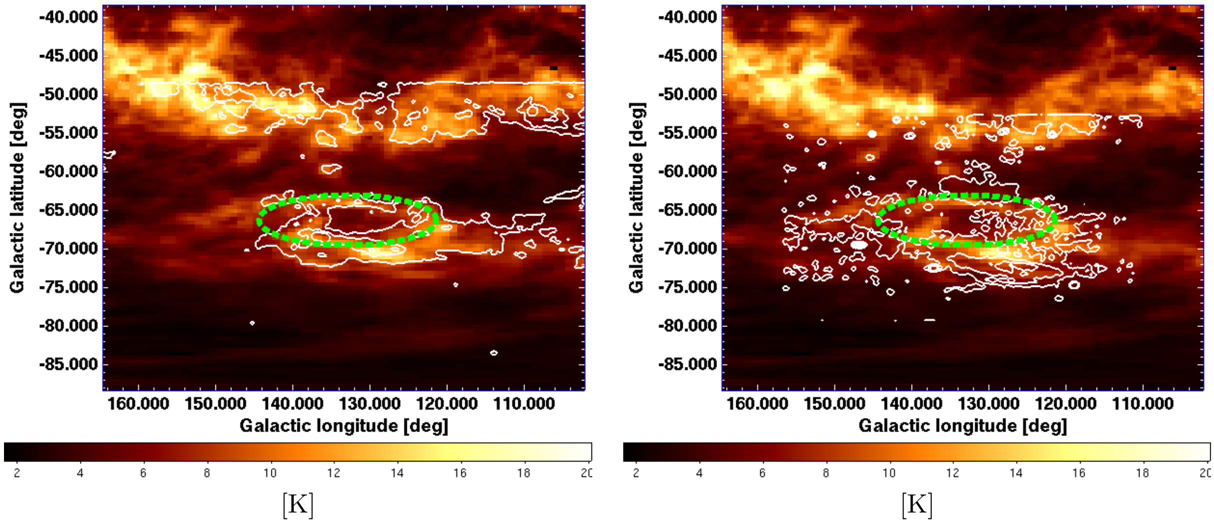

(a) background: H I line (21 cm)
contours: IR continuum (100 μm)

(b) background: H I line (21 cm)
countours: Hα line (656 nm)

(c) background: H I line (21 cm)
contours: X-ray continuum (0.25 keV)

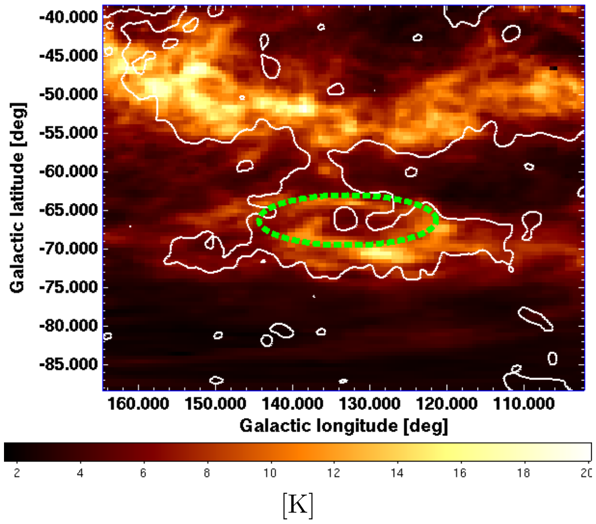

Figure 2.35: *GS133-66-013.* Contours of various wavelengths overlaid on the neutral hydrogen emission, with the identified H I shell (green dashed ellipse).

2.3.8 GS134-01-028

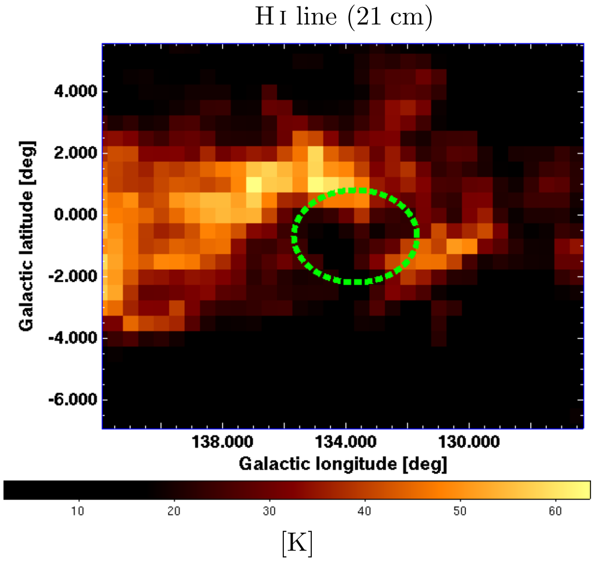

Figure 2.36: *GS134-01-028.* Neutral hydrogen emission with the identified expanding shell (green dashed ellipse).

This shell is located in the Galactic disc, near the well known star-forming regions in the Perseus Arm of the Galaxy. The expansion velocity is 8.3 km/s, its angular distance is $9.4^{\circ 2}$, the kinematical distance is about 1.5 kpc and the shell radius is 45.4 pc. The density of the ambient medium is about 2.37 cm^{-3} and the embedded energy 3.93×10^{50} erg. The shell consist of a hole partially surrounded by borders, open in the southern direction.

Counterpart infrared emission (figure **2.37a**$_{(70)}$ and **2.38a**$_{(71)}$) The infrared emission shows bright and distinct condensation of dust in the areas of the H II regions. There is a hole in the center of the H I shell, observable better with slightly shifted image contrast, and faint border, open in the south.

First condensation is located in the northern border of the shell, while the second is outside the shell, in the northeastward direction. Both condensations contain a small, spherical holes, indicating remnants of former star formation.

Counterpart Hα emission (figure **2.37b**$_{(70)}$ and **2.38b**$_{(71)}$) Hα emission reveals two distinct H II regions. One is located in the northern border and contains well known star forming regions W 3 and W 4. Second region—W 5—is located northeastwardly off the shell. Considering that the ellipse is only the interpolated shape of the H I shell, looking at the H I line emission, we can assume that also the W 5 region is touching the shell border in the northeast.

Counterpart X-ray emission (figure **2.37c**$_{(70)}$) X-ray emission shows only an unclear image with no obvious correlation with the H I emission line.

Counterpart CO emission (figure **2.37d**$_{(70)}$ and **2.38c**$_{(71)}$) CO emission reveals a large molecular cloud in the northern part of the shell's border, partially surrounding the W 3 H II region. Smaller condensation are found also near the W 5 region.

Counterpart Young Stellar Objects (figure **2.39**$_{(72)}$) The W 5 region contains tens of associated young stellar objects. Several young stellar objects are also discovered in the W 3 region.

The W 3, W 4, W 5 H II regions are thought to be examples of triggered star formation (Lada et al., 1978; Karr & Martin, 2003, see for example). In particular, the W 4 region is considered as a trigger of star formation in the W 3 region.

The radial velocities of the W 3/W 4/W 5 complexes are in the range of -37– -40 km/s (Lada et al., 1978; Karr & Martin, 2003); their distance is about 2 kpc (Hachisuka et al., 2006; Xu et al., 2006; Karr & Martin, 2003).

Summary Even though the ellipse describing the H I shell does not border with the W 5 region, the original shell may have supported star formation, or at least condensation of the medium. The interpolated ellipse may be shifted slightly (in both spatial and velocity dimension) from its original center as a result of expansion in an inhomogenous medium and dynamical processes such as the differential Galactic rotation and large-scale streams of the interstellar medium.

Correlation of the dust condensation with H II regions suggest that these regions are active heating sources of the dust. Note especially holes inside the dust condensations.

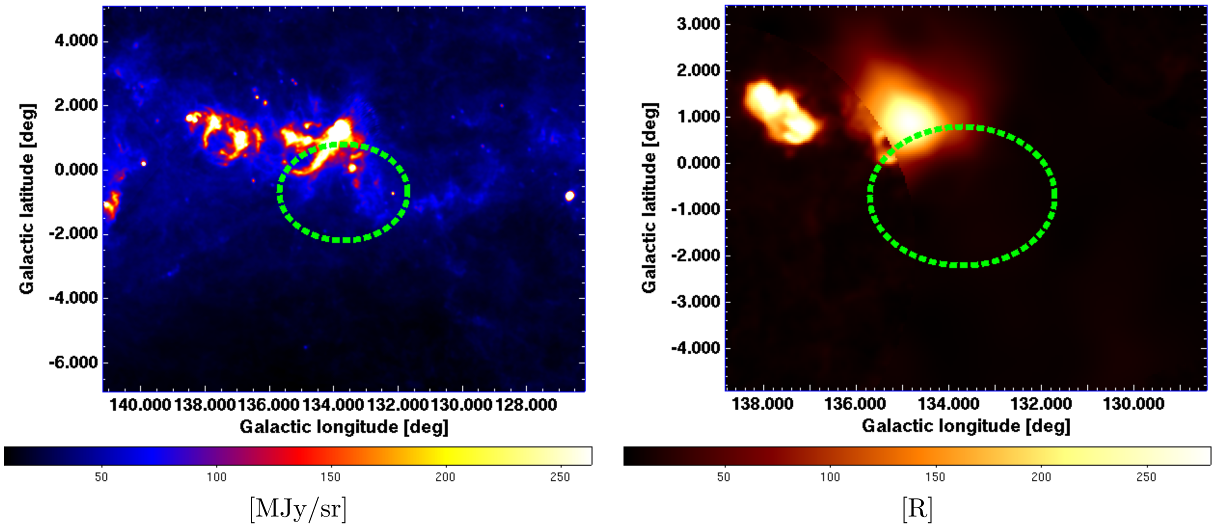

(a) IR continuum (100 µm)

(b) Hα line (656 nm)

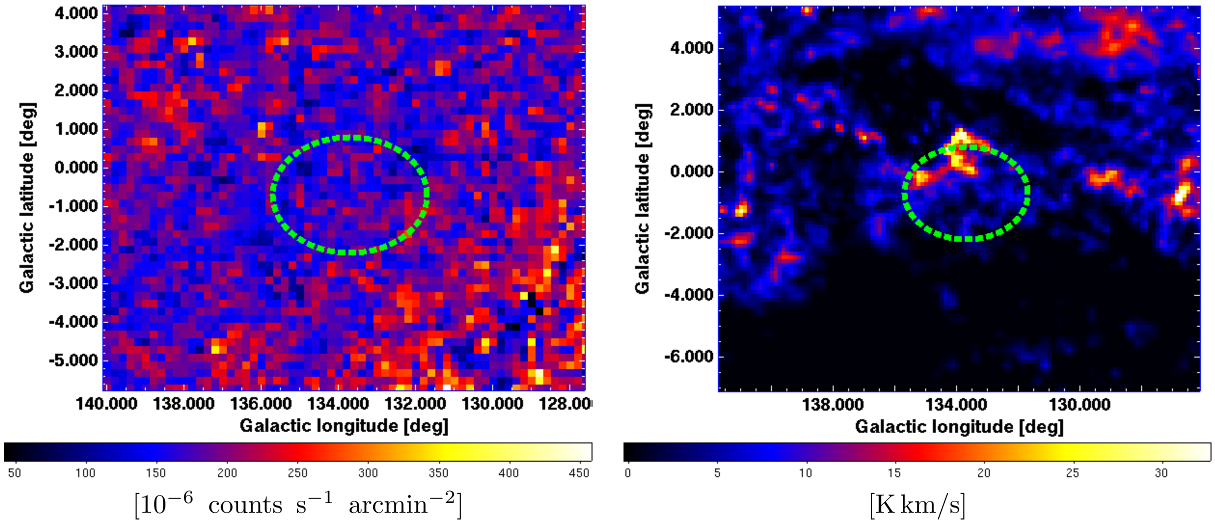

(c) X-ray continuum (0.25 keV)

(d) CO line (2.6 mm)

Figure 2.37: *GS134-01-028.* Multiwavelength images of the vicinity of the H I shell. (green dashed ellipse).

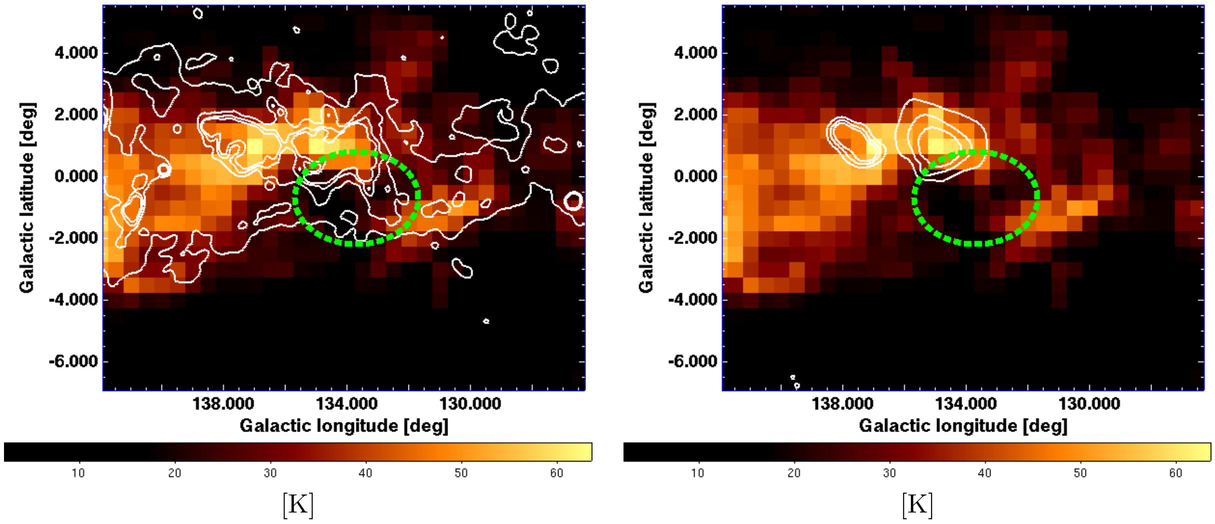

(a) background: H I line (21 cm)
contours: IR continuum (100 µm)

(b) background: H I line (21 cm)
countours: Hα line (656 nm)

(c) background: H I line (21 cm)
contours: CO line (2.6 mm)

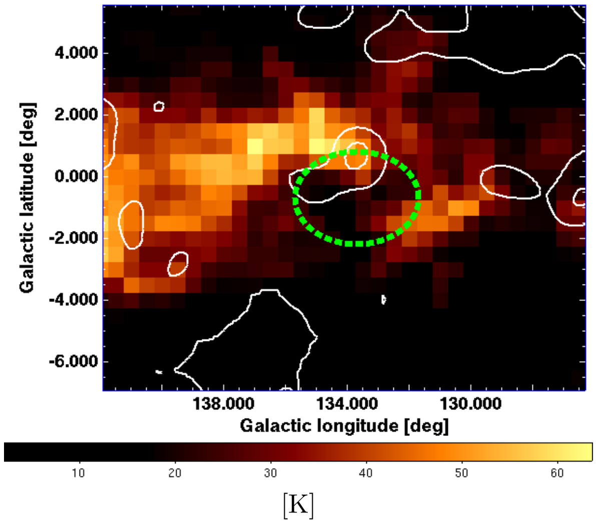

Figure 2.38: *GS134-01-028.* Contours of various wavelengths overlaid on the neutral hydrogen emission, with the identified H I shell (green dashed ellipse).

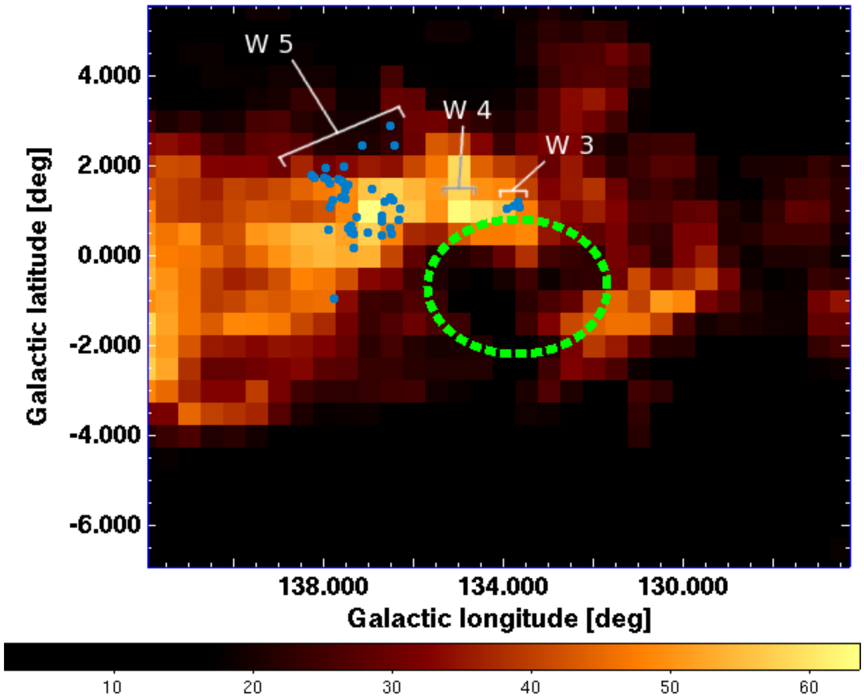

Figure 2.39: *GS134-01-028:* Young stellar objects (blue points) in the direction of the H I shell (green dashed ellipse).

2.3.9 GS202+19-019

This H I shell in an example of shells with open and strongly nonuniform borders. The border is open in the eastern part, with a brighter region in the northwestern direction, touching the larger, denser area in the southwestern region. The neutral hydrogen in the neighbourhood suggests that the shell is expanding inside an inhomogenous medium with a gradient pointing westwards, and also with preexisting condensations of neutral medium in the vicinity. Its central radial velocity, −18.8 km/s, is an example of peculiar motion of the neutral medium. Therefore its kinematical distance and dependent properties can not be determined. The shell's expansion velocity is 10.8 km/s and its angular area is 26.6$^{\circ 2}$.

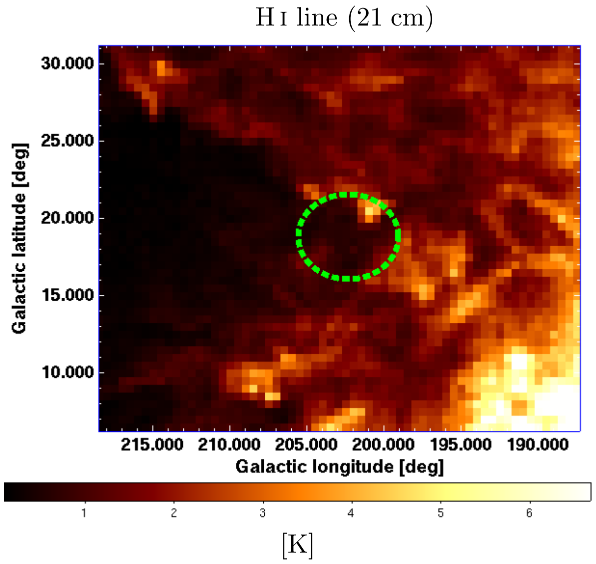

Figure 2.40: *GS202+19-019.* Neutral hydrogen emission with the identified expanding shell (green dashed ellipse).

Counterpart infrared emission (figure **2.41a**(74) and **2.42a**(75)) The infrared emission shows similar structure: a hole inside with a broken border in the eastward direction. Most of the border consists of dust condensations in filamentary structures. The distance of the catalogued counterpart far-infrared loop is 0.4 kpc.

Counterpart Hα emission (figure **2.41b**(74) and **2.42b**(75)) Hα emission shows in this case no similar structures. Only faint diffuse emission penetrates the shell and seems apparently not associated to it.

Counterpart X-ray emission (figure **2.41c**(74)) The X-ray emission apparently penetrates the shell but does not reveal any distinct features possibly associated to H I emission. The X-ray emission shows negative correlation with the dust emission.

Summary Counterpart infrared emission is observed, but no Hα or X-ray emission with some features similat to the H I emission. X-ray emission is more intensive in the direction where dust emission is fainter. This is probably another example of shadowing, when dust absorption prevents soft X-ray diffuse emission originating in hot gas in the halo. SIMBAD contains no catalogued young stellar objects in the direction of the shell and CO emission is not available for this region.

(a) IR continuum (100 µm) **(b)** Hα line (656 nm)

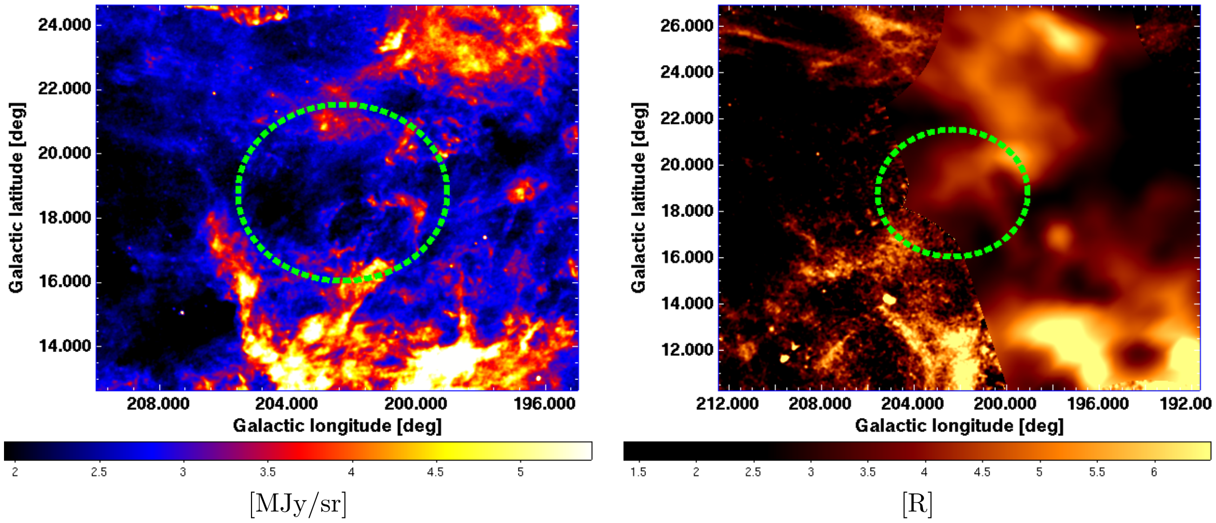

(c) X-ray continuum (0.25 keV)

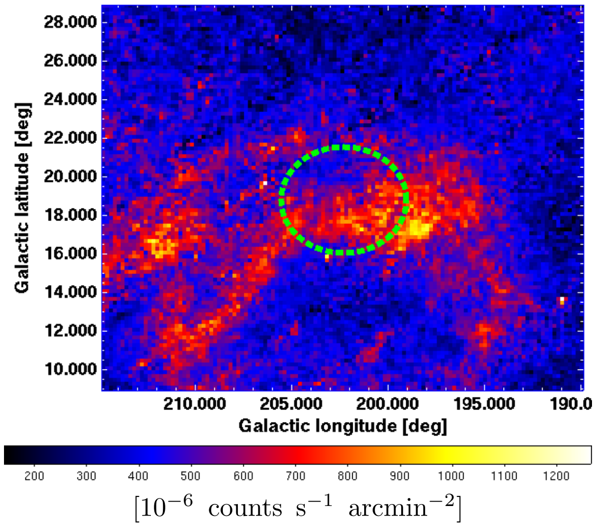

Figure 2.41: *GS202+19-019.* Multiwavelength images of the vicinity of the H I shell. (green dashed ellipse).

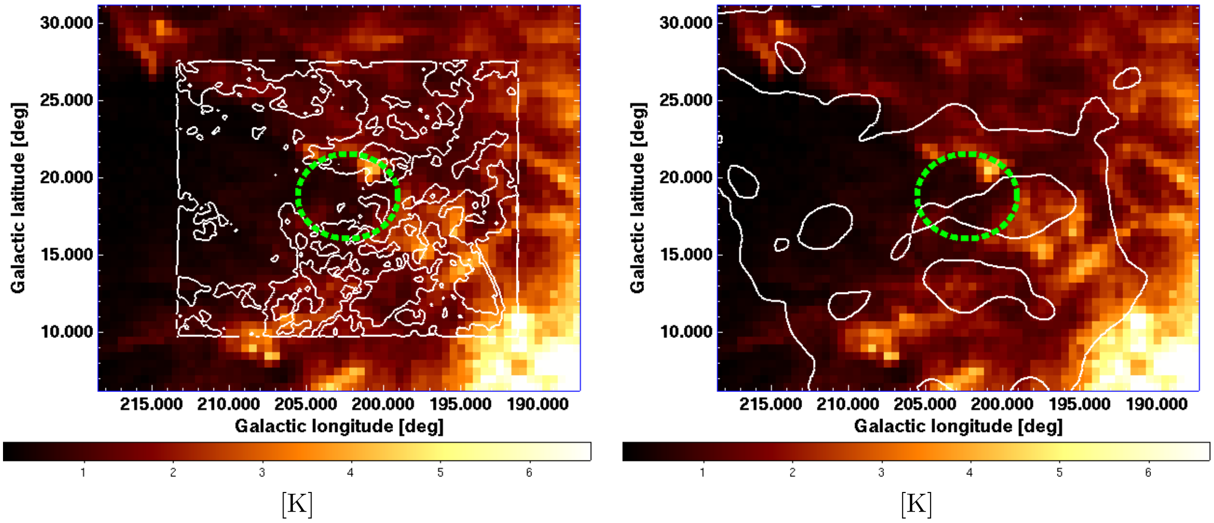

(a) background: H I line (21 cm)
contours: IR continuum (100 μm)

(b) background: H I line (21 cm)
contours: X-ray continuum (0.25 keV)

Figure 2.42: *GS202+19-019.* Contours of various wavelengths overlaid on the neutral hydrogen emission, with the identified H I shell (green dashed ellipse).

2.3.10 GS206-17+013

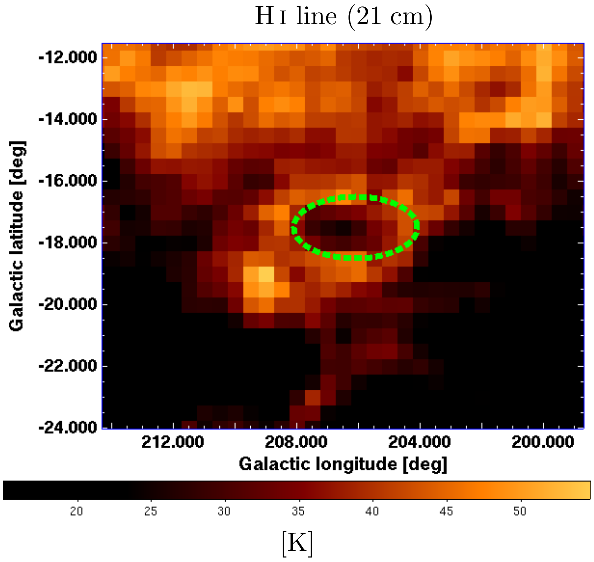

Figure 2.43: *GS206-17+013.* Neutral hydrogen emission with the identified expanding shell (green dashed ellipse).

This H I shell is expanding with a velocity of 7.8 km/s, its angular area is $6.0^{\circ 2}$, its kinematical distance is 2.0 kpc and the radius is 43.4 pc. The shell is an example of mid-latitude shells expanding near the southern edge of the Galactic disc in a stratified medium. The shell is fully enclosing the central hole and is slightly elongated in the longitudinal direction. The particle density of the ambient medium is about $0.99\ \mathrm{cm}^{-3}$ and the embedded energy 1.19×10^{50} erg.

The shell is apparently located in the *Orion Molecular Cloud Complex*, one of the most active regions of stellar formation that have been observed. The Complex consist of several H II regions and associated molecular clouds. Notable are the *Orion Nebula*, the *Horsehead Nebula* and *Bernard's Loop*.

Counterpart infrared emission (figure **2.44a**(79) and **2.45a**(80)) The infrared emission reveals two large dust condensations associated with the corresponding H II regions. One is partially covering the norther edge of the shell, and one is located outside the southeast border. There are several other fragmented filamentary condensations around the central hole coinciding with the shell's border but not associated with Hα emission.

Althoug the distance to the counterpart far-infrared loop is given as 0.3 kpc, the arrangement of the dust fragments around the border suggest, that the H I shell and far-infrared loop are associated.

Counterpart Hα emission (figure **2.44b**(79) and **2.45b**(80)) The Hα emission apparently filling the eastern part of the shell's interior is associated with the H II region *IC 434*. This region contains also the Horsehead Nebula.

Another H II region is observed in the northern border of the shell as a compact Hα emission. This is the *Flame Nebula* (also Orion B or W 12) associated with the cluster of stars *NGC 2024*. It is a reflection nebula illuminated by *Alnitak*[37]—an O9.5 star.

These two H II regions are probably responsible for heating ambient dust condensations, observed in the infrared emission.

---

[37] Alnitak is also the hostname of the computer I have used for this work.

The H II region located southeastwards is the Orion Nebula (also M 42), embedding an associated cluster of stars—the *Orion Nebula Cluster*. The distance to the Orion Nebula is 414 ± 7 pc, and its radial velocity is 9.6 ± 4.2 km/s (Menten et al., 2007).

Note that the Orion Nebula is observed in all multiwavelength images, even in X-rays (see figure **2.44a–d**$_{(79)}$).

The intensity of the inner H II region is increasing in the outward direction, indicating that the ionized hydrogen is distributed in a half-spherical region, open in the direction to the shell's interior.

Whole this complex is surrounded by an arc—Bernard's Loop—see figure **2.45b**$_{(80)}$.

Counterpart X-ray emission (figure **2.44c**$_{(79)}$) There is no obvious counterpart X-ray emission in the direction of the shell. A localized increase in intensity is observed in the direction of The Orion Nebula, suggesting there is hot gas in the nebula.

Counterpart CO emission (figure **2.44d**$_{(79)}$ and **2.45c**$_{(80)}$) CO emission reveals condensations of molecular clouds associated with the H II regions, making an ideal environment for star formation triggered by expanding H II regions.

Note that the observed clouds of molecular hydrogen are in touch with the observed H II regions—they do not merge. On the other hand, dust penetrates both H II regions and molecular clouds.

Counterpart young stellar objects (figure **2.46**$_{(81)}$) There are two groups of catalogued young stellar objects. The first group, located apparently inside the H I shell, is the *σ Orionis Young Group*, a constituent of the *Orion OB1b association*. The group distance is about 350 pc (Hipparcos catalogue: Perryman et al. 1997). Its mean radial velocity is about 30 km/s (Burningham et al., 2005; Kenyon et al., 2005; Muzerolle et al., 2003), some measurements show even more (37.3 ± 5.8 km/s, Zapatero Osorio et al., 2002). The radial velocity of the group is higher that the radial velocity of the shell, signing that the group is more distant than the shell. On the other hand, the distance of the group is smaller than the distance of the shell, suggesting that the group is a foreground object with respect to the shell.

Moreover the measurements of the cited authors reveals, that some apparently associated YSOs, excluded from the group, creates several smaller groups with lower radial velocities, close to the velocity of the H I shell.

Interesting phenomenon is, that if we average the radial velocities of all YSOs considered by Burningham et al. (2005), we get 13.8 km/s, what would make the group significantly larger and would also put its kinematical center to the kinematical center of the studied H I shell. But—following the figure 6 in the cited paper—this is probably not the actual configuration.

This discrepancy—radial velocity versus distance in context of the Galactic rotation—may be a sign of peculiar motion of the group or even whole region.

The second group, located apparently in the northern border of the shell, is associated with the *NGC 2024* star cluster, whose radial velocity measured by Fomalont & Weliachew (1973) is 8.65 km/s. This value is in the velocity range, spanned by the H I shell.

There is one more isolated young stellar object, published in the IRAS Catalogue as *IRAS 05399-0121*, whose radial velocity and distance is not available.

Summary Comparison of the mean radial velocity of the H I shell with the radial velocities of the nebulae in the Orion Molecular Cloud Complex, and also with the mean radial velocity of the identified young stellar objects, suggests that the observed H I shell is associated with the Complex. We are probably looking at a young remnant of recent star formation associated with the IC 434 H II region. Another remnant of the previous generation of stars and supernovae is Bernard's Loop.

The infrared dust emission, compared with the Hα and CO emission, represents the transition between ionized hydrogen and molecular cloud.

Because the Orion Complex is a region rich in objects associated with star formation, it is likely that the studied H I shell is connected to the dynamics of the region. Taking into account Bernard's Loop, the H I shell is smaller by about one order of magnitude. Therefore is is probably either a remnant of a consequent generation of stars, or a remnant of a subgroup of the original group of stars that have created Bernard's Loop.

(a) IR continuum (100 µm) **(b)** Hα line (656 nm)

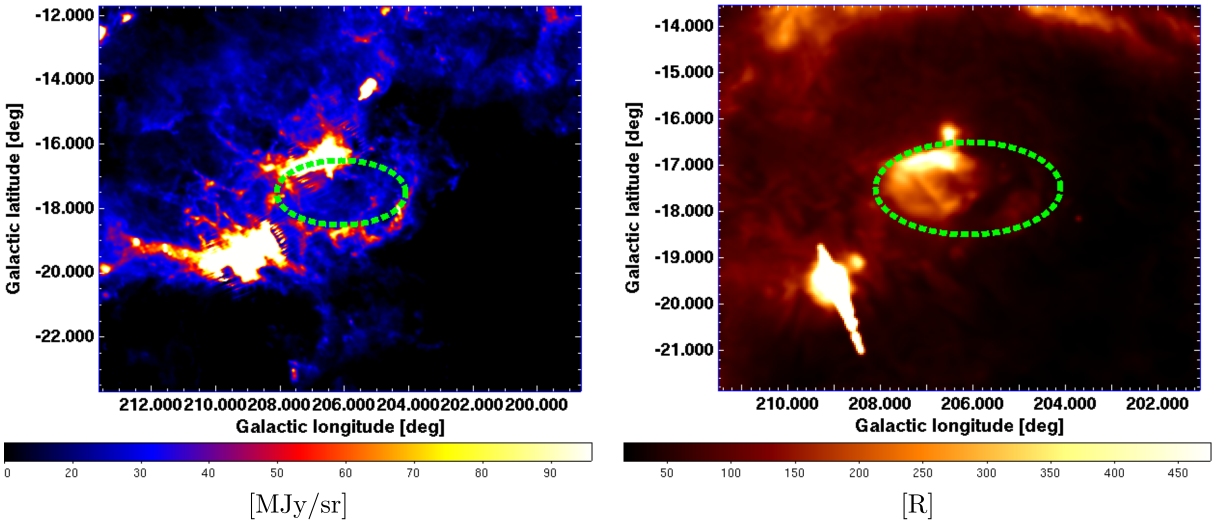

(c) X-ray continuum (0.25 keV) **(d)** CO line (2.6 mm)

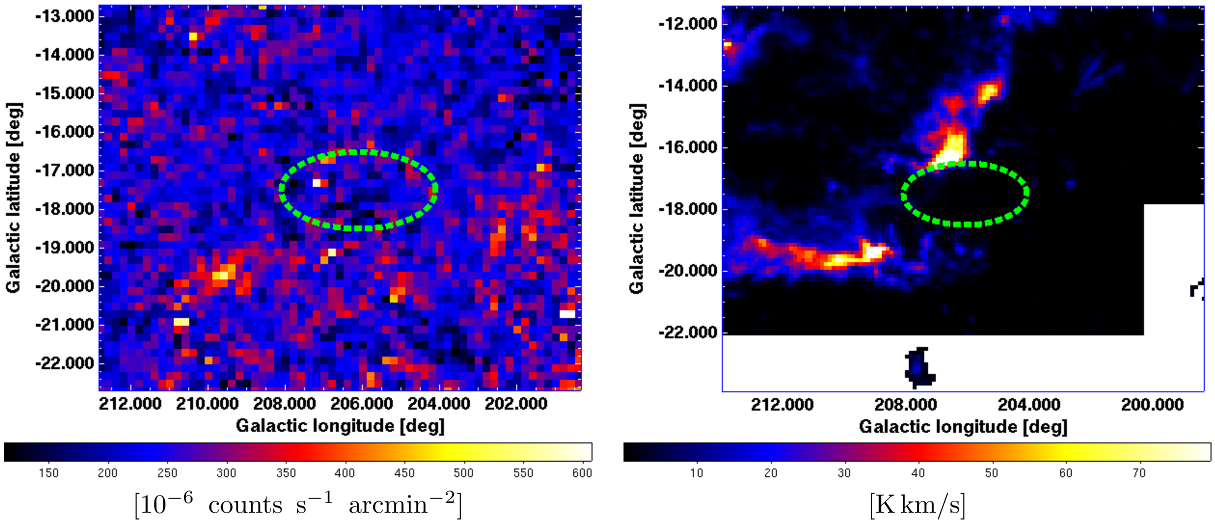

Figure 2.44: *GS206-17+013.* Multiwavelength images of the vicinity of the H I shell. (green dashed ellipse).

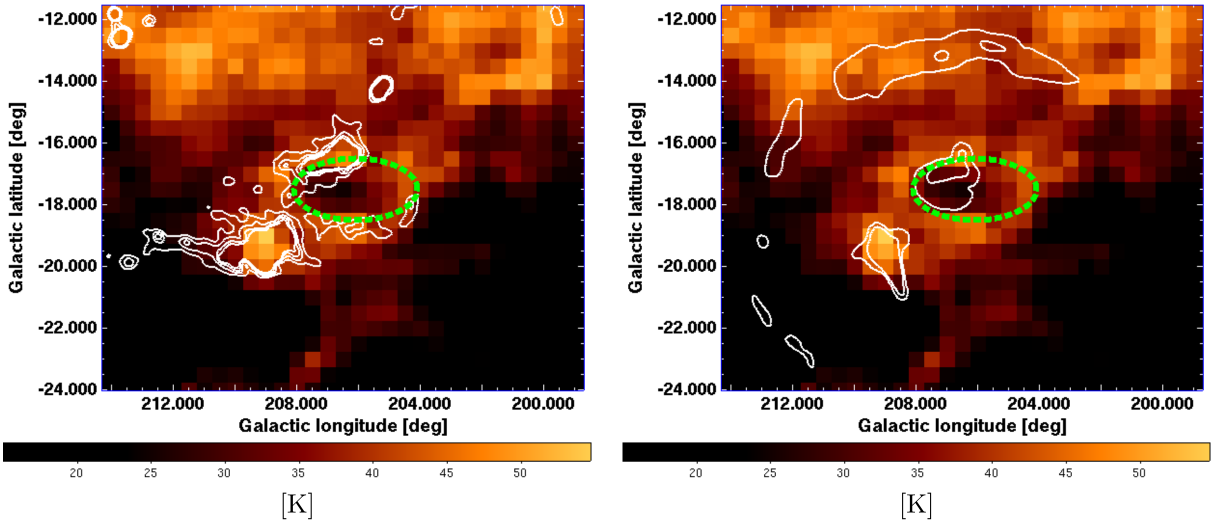

(a) background: H I line (21 cm)
contours: IR continuum (100 µm)

(b) background: H I line (21 cm)
countours: Hα line (656 nm)

(c) background: H I line (21 cm)
contours: CO line (2.6 mm)

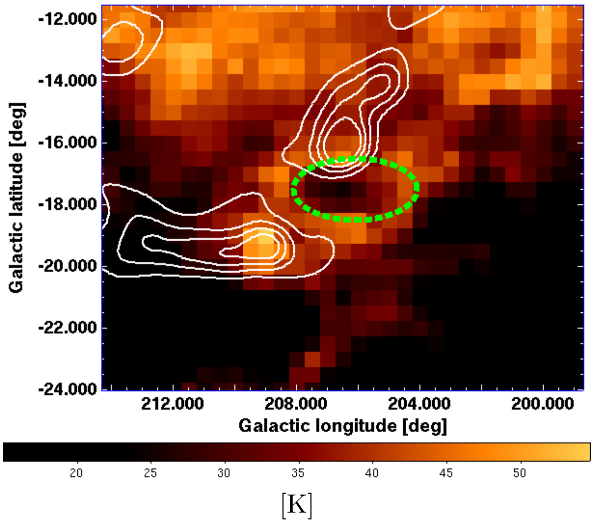

Figure 2.45: *GS206-17+013.* Contours of various wavelengths overlaid on the neutral hydrogen emission, with the identified H I shell (green dashed ellipse).

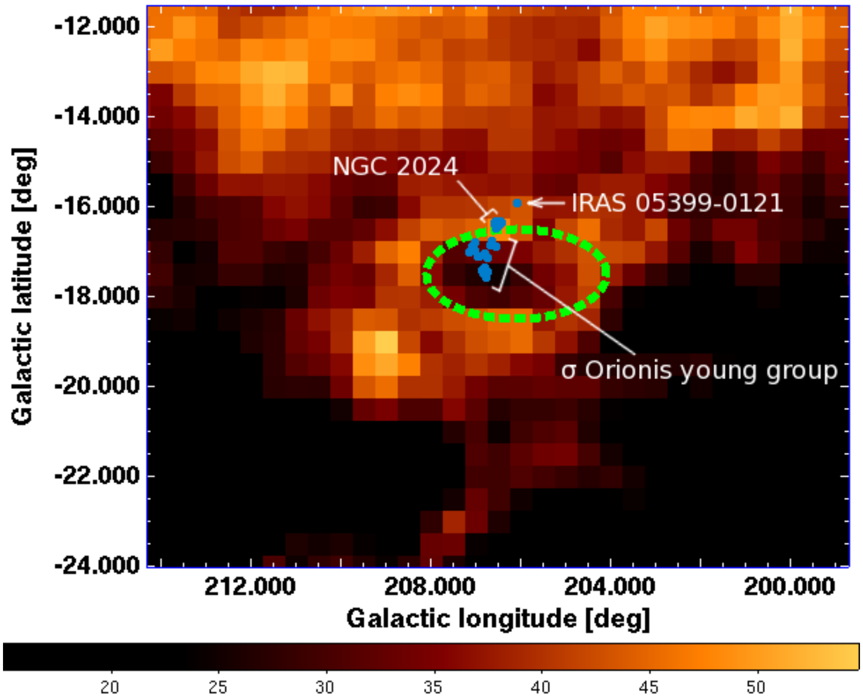

Figure 2.46: *GS206-17+013*. Young stellar objects (blue points) in the direction of the H I shell (green dashed ellipse).

2.3.11 GS218-05+031

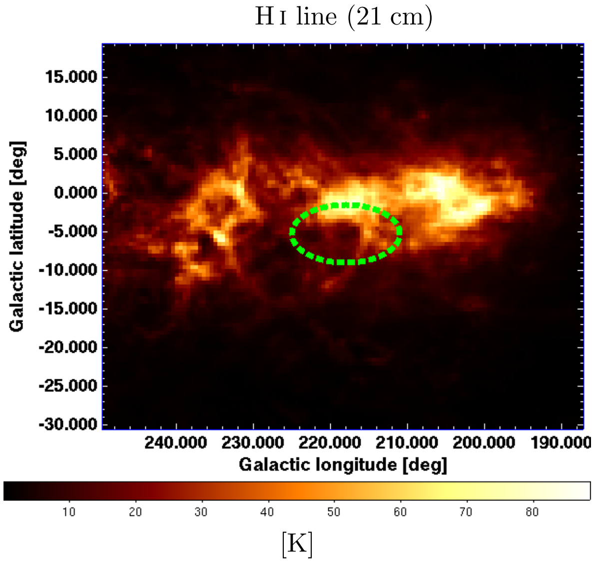

Figure 2.47: *GS218-05+031.* Neutral hydrogen emission with the identified expanding shell (green dashed ellipse).

This H I shell is an example of shells with an irregular shape and nonuniform borders. The expansion velocity is 8.3 km/s, the angular area is $82.11^{\circ 2}$ and the ambiguous kinematical distance is 2.5 or 4.5 kpc from the Sun. In the former case—distance of 2.5 pc—the shell radius is 223.1 pc, the local particle density is $0.58\ \mathrm{cm}^{-3}$, the embedded energy is 1.18×10^{52} erg and shell would expand in the southern part of the Galactic disc. In the latter case—distance of 4.5 kpc—the shell radius is 401.5 pc, the particle density is $0.32\ \mathrm{cm}^{-3}$, the embedded energy is 3.82×10^{52} erg and shell would be located at the souther edge of the Galactic disc.

Counterpart infrared emission (figure **2.48a**(84) and **2.49a**(85)) The counterpart infrared emission reveals fragments of condensed dust surrounding the central hole. There are several larger dust condensations, especially in the Galactic disc (northwards off the shell). These bright clouds are obviously associated with the ambient H II regions (see figure **2.48a,b**(84)).

Counterpart Hα emission (figure **2.48b**(84)) Hα emission show no obvious correlation with the H I observations. Because the H I shell is located in the direction of the Galactic disc, there is abundance of bright H II regions in the shell vicinity. Diffuse Hα emission is penetrating the shell, but does not seem to be associated with it.

Counterpart X-ray emission (figure **2.48c**(84)) There is no counterpart X-ray emission observed towards the H I shell. This may be a result of extinction in the galactic disc. Assuming the shell is located 2.5 or 4.5 kpc away from Sun, any associated X-ray emission of the shell would be absorbed by the galactic disc.

Counterpart CO emission (figure **2.48d**(84) and **2.49b**(85)) CO emission is well negatively correlated with the Hα emission, suggesting ongoing propagated star formation. There are also filamentary condensations apparently associated with the dust fragments. Note especially the one located in the southern edge of the shell. This fragment is observed both in the infrared dust emission and the CO emission, but not in the Hα region. This may be an example of a very young star forming region, in the stage before the H II region is created.

Counterpart young stellar objects There are several young stellar objects found in SIMBAD. Notable is the group associated to the molecular cloud *S287*. The distance to the cloud is about 2.3 kpc and its radial velocity is about 27.2 km/s (Williams & Maddalena, 1996). The radial velocity is very close to that of the H I shell.

Single young stellar objects are observed in the northern region of the shell, but kinematical data are missing in SIMBAD in all cases but one—the UYSO 1 object.

UYSO 1 (Unidentified Young Stellar Object) is a massive protostar, discovered by Forbrich et al. (2004), with an adopted distance 1 kpc. This suggests that the UYSO 1 is probably a foreground object with respect to the H I shell.

Summary Dust is arranged around the central hole of the H I shell in filaments and larger condensations. Also the molecular clouds are surrounding the central hole. One notable condensation, located in the suthern border of the H I shell, shows dust and molecular gas contents, but no associated H II region. This may be an early stage of star formation.

In the northern region of the shell's edge, there is a group of young stellar objects probably associated with the shell. Their creation may have been induced or at least supported by the expanding H I shell.

(a) IR continuum (100 µm) **(b)** Hα line (656 nm)

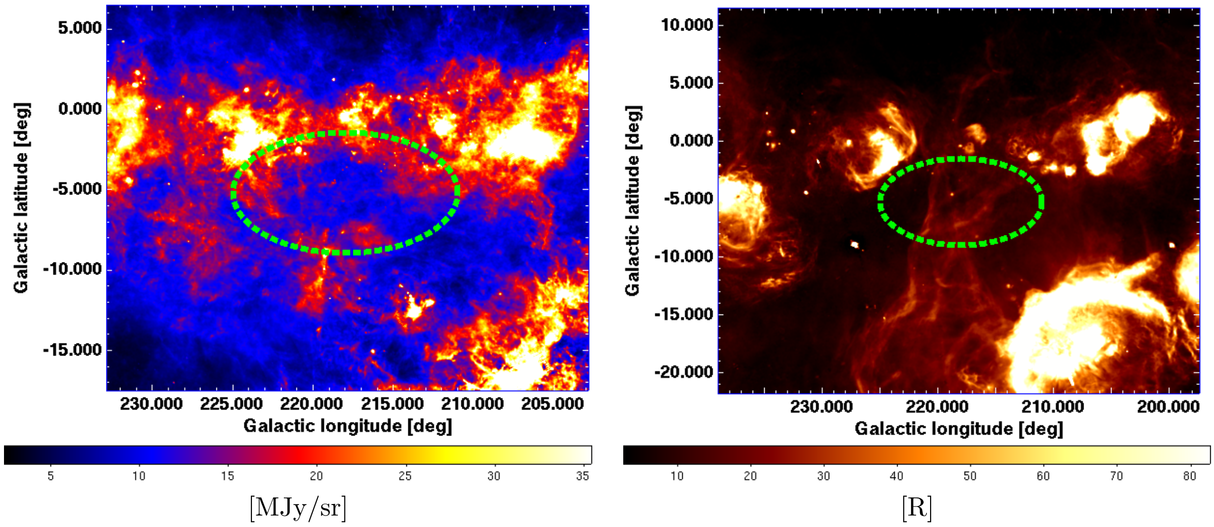

(c) X-ray continuum (0.25 keV) **(d)** CO line (2.6 mm)

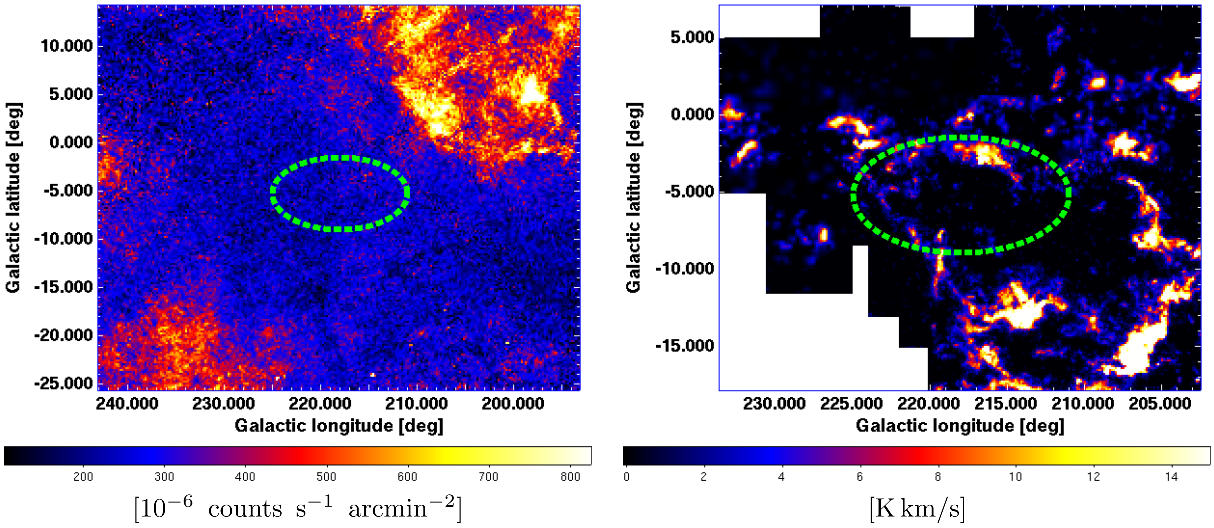

Figure 2.48: *GS218-05+031.* Multiwavelength images of the vicinity of the H I shell. (green dashed ellipse).

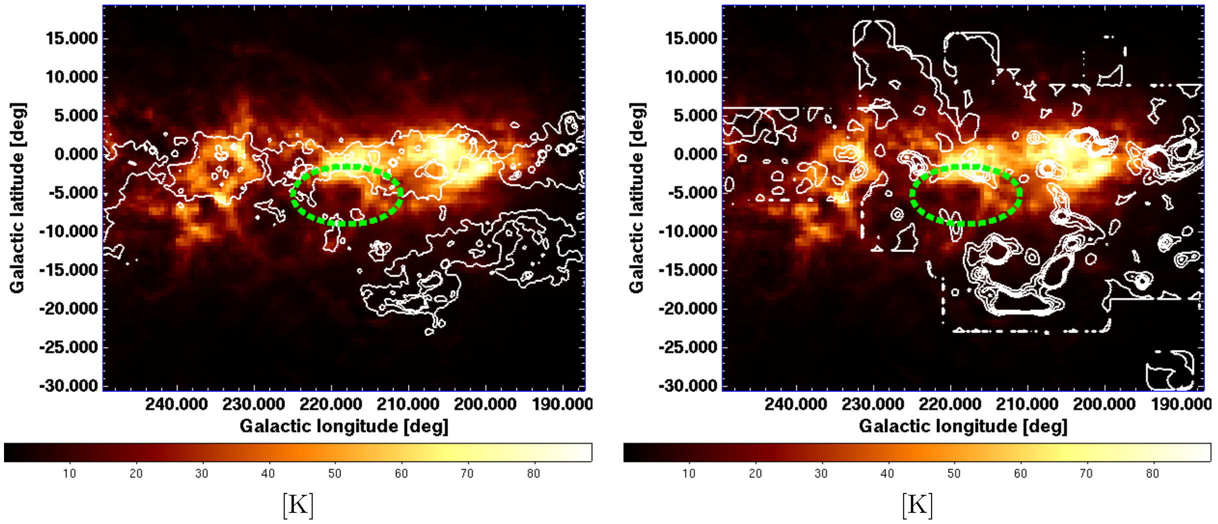

(a) background: H I line (21 cm)
contours: IR continuum (100 µm)

(b) background: H I line (21 cm)
contours: CO line (2.6 mm)

Figure 2.49: *GS218-05+031.* Contours of various wavelengths overlaid on the neutral hydrogen emission, with the identified H I shell (green dashed ellipse).

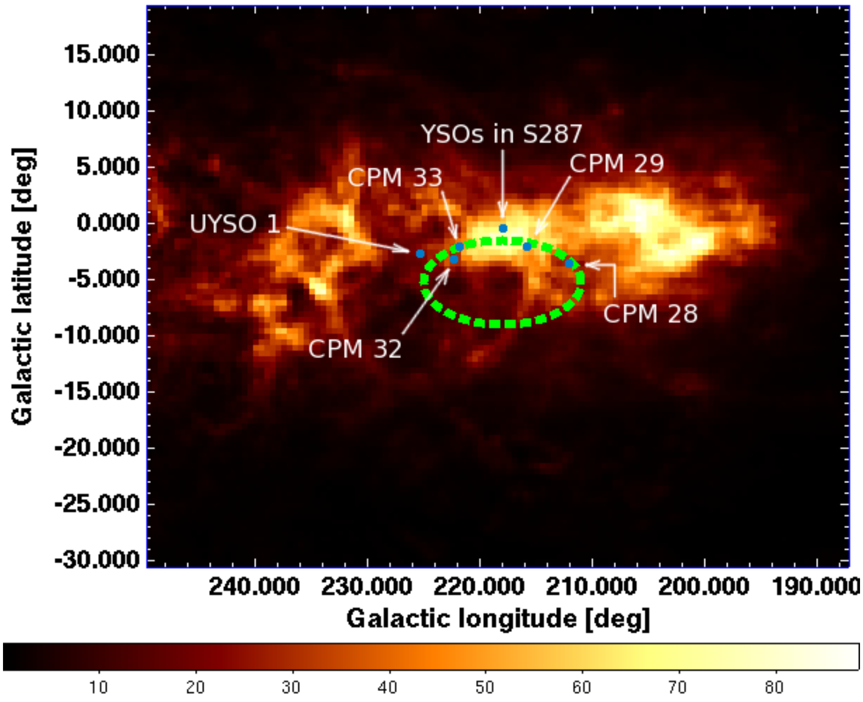

Figure 2.50: *GS218-05+031.* Young stellar objects (blue points) in the direction of the H I shell (green dashed ellipse).

2.3.12 GS231+38+003

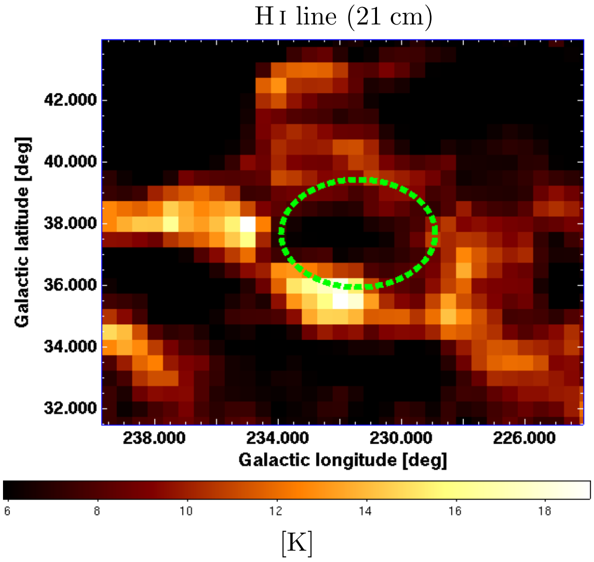

Figure 2.51: *GS231+38+003*. Neutral hydrogen emission with the identified expanding shell (green dashed ellipse).

This H I shell is another example of a high-latitude shell with a fully enclosed hole in the center, but nonhomogenous borders. Its expansion velocity is 4.1 km/s, the angular area is $10.9^{\circ 2}$, the kinematical distance is 0.2 kpc and the shell radius in 6.5 pc. The shell is expanding in the northern part of the Galactic disc in a medium with density about 2.62 cm^{-3}. The embedded energy is about 3.85×10^{47} erg.

Counterpart infrared emission (figure **2.52a**(87) and **2.53a**(88)) The infrared emission shows a distinct hole in the center surrounded by several dust fragments. Large dust condensation is bordering the shell from the eastern side, one fragment is located in the southern border and one outside the northwestern border of the shell. These fragments do not show obvious correlation with the Hα emission. The largest dust condensation shows obvious negative correlation with the X-ray emission. It is another example of shadowing.

The eastern and southern condensations are apparently associated with excesses in the H I emission.

Counterpart Hα emission (figure **2.52b**(87)) Hα emission shows no clear counterpart of the shell. Faint and diffuse emission is pervading the southwestern border.

Counterpart X-ray emission (figure **2.52c**(87) and **2.53c**(88)) The X-ray emission correlates negatively with the dust emission, suggesting that the dense medium in the foreground absorbs it. An increased intensity in the central hole of the shell can be explained by the shadowing effect too.

Summary Infrared emission reveals several clouds of dust aroung the central hole. These clouds are probably responsible for decreased intensity of X-ray emission. No young stellar objects were found in SIMBAD. CO emission is not available for this region.

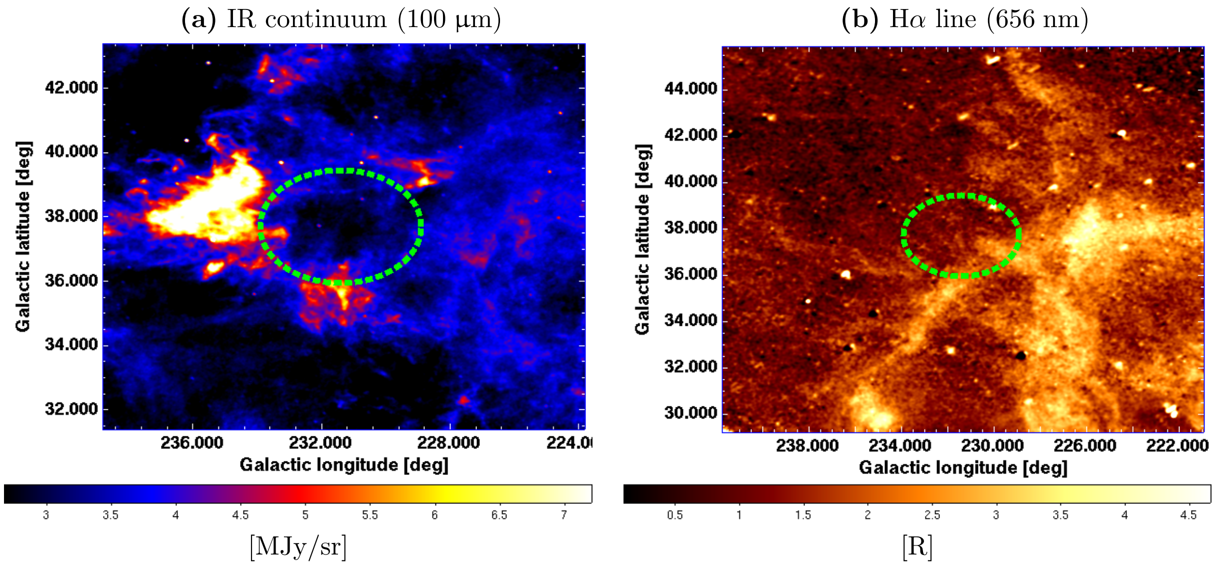

(a) IR continuum (100 µm)

(b) Hα line (656 nm)

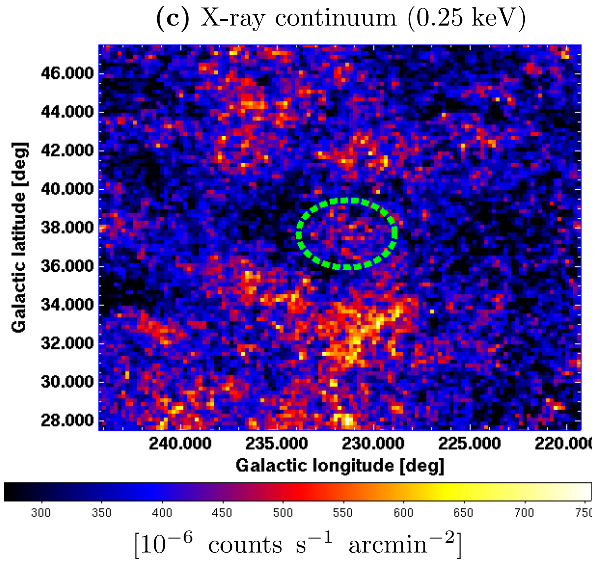

(c) X-ray continuum (0.25 keV)

Figure 2.52: *GS231+38+003*. Multiwavelength images of the vicinity of the H I shell. (green dashed ellipse).

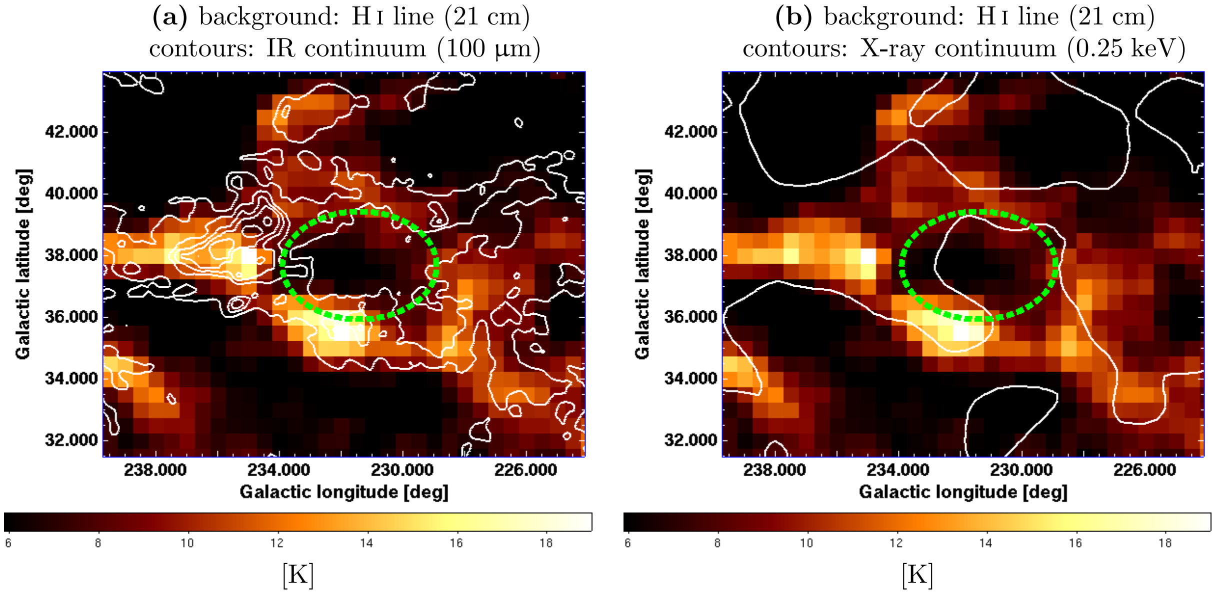

Figure 2.53: *GS231+38+003*. Contours of various wavelengths overlaid on the neutral hydrogen emission, with the identified H I shell (green dashed ellipse).

Chapter 3

Conclusion

3.1 Summary of Results

3.1.1 Counterpart Far-Infrared Loops

The catalogue of H I shells of Ehlerová & Palouš (2005) contains 628 shells. The number of close shells—with kinematical distance equal to or less than 3.5 kpc—is 491. 125 H I shells manifest peculiar velocities with respect to the galactic rotation, thus their kinematical distances can not be derived from their radial velocities. There are 58 H I shells with associated far-infrared loop from the catalogue Kiss et al. (2004); Könyves et al. (2007). From these 58 H I shells, 12 were selected for multiwavelength study.

3.1.2 Multiwavelength Study of Selected H I Shells

The multiwavelength images of the vicinity of H I shells were based on

- radio all-sky maps of the H I emission line—see section $2.1.1_{(21)}$—
- radio non–all-sky maps of the CO emission line—see section $2.1.2_{(23)}$—
- infrared all-sky maps of dust continuum emission—see section $2.1.3_{(24)}$—
- optical all-sky maps of the Hα line—see section $2.1.4_{(26)}$—and
- X-ray all-sky maps of hot gas continuum emission—see section $2.1.5_{(27)}$.

I have also performed a search for associated young stellar objects catalogued in the SIMBAD database.

The multiwavelength study of twelve selected H I shells presented in the section $2.3_{(40)}$ shows that dust is well correlated with neutral hydrogen, at least for the studied shells. Note that all the studied shells have a counterpart far-infrared loop. There are often condensations of interstellar dust and molecular gas found at the borders of H I shells, suggesting that they create environment convenient for star formation.

Comparison of the H I emission with the Hα emission shows that H II regions are located outside the studied shells, with only one exception—H I shell GS206-17+013 in the Orion Nebula.

There are four H I shells with apparently associated catalogued young stellar objects (GS116+02+006, GS134-01-028, GS206-17+013, GS218-05+031).

The X-ray emission shows no significant counterparts. There are several cases of shadowing effect—for example H I shells GS062-42+004 and GS074-52-004—when the foreground medium (dust and gas) absorbs X-ray emission from hot gas of the Galactic halo.

Estimated energies embedded in the studied H I shells with other properties are summarized in table **3.1**$_{(90)}$.

The table **3.2**$_{(91)}$ contains a brief summary of associated counterparts of the studied H I shells. Avoid the misinterpretation of this overview. It describes apparently associated counterparts. For the discussion of possible physical association, see section 2.3$_{(40)}$—Multiwavelength Study of Selected H I Shells.

Table 3.1: Summary of the basic properties of twelve studied H I shells. v_{exp} is the expansion velocity, d is the kinematical distance, r_{sh} is the radius, and E_{tot} is the total energy. See preface to the section 2.3$_{(40)}$ for detailed explanation of these values.

H I shell	v_{exp} [km/s]	d [kpc]	r_{sh} [pc]	n_{local} [cm^{-3}]	E_{tot} [erg]
GS016-09+011					
	4.1	1.0	33.6	0.35	6.89×10^{48}
GS062-42+004					
	8.8	0.4	26.3	1.60	5.07×10^{49}
		4.5	296.2	0.14	6.41×10^{51}
GS074-52-004					
	7.2	0.1	2.6	10.16	2.15×10^{47}
		3.0	77.1	0.34	1.93×10^{50}
GS075-09-005					
	9.3	0.2	3.4	6.02	3.91×10^{47}
		4.9	82.3	0.25	2.34×10^{50}
GS097-03-029					
	12.9	2.1	63.4	1.80	1.54×10^{51}
GS116+02+006					
	5.2				
GS133-66-013					
	9.3	0.4	27.1	0.90	3.13×10^{49}
GS134-01-028					
	8.3	1.5	45.4	2.37	3.93×10^{50}

(continuing on the next page)

Table 3.1: (continued)

H I shell	v_{exp} [km/s]	d [kpc]	r_{sh} [pc]	n_{local} [cm^{-3}]	E_{tot} [erg]
GS202+19-019					
	10.8				
GS206-17+013					
	7.8	1.8	43.4	0.99	1.19×10^{50}
GS218-05+031					
	8.3	2.5	223.1	0.58	1.18×10^{52}
		4.5	401.5	0.32	3.82×10^{52}
GS231+38+003					
	4.1	0.2	6.5	2.62	3.85×10^{47}

Table 3.2: Summary of observations of apparently associated counterparts of H I shells. The column "Counterpart" contains type of the counterpart. The column "Observed" contains YES/NO meaning if there were observed any features, possibly associated to the studied H I shell. The column "Nature" contains the apparent nature of the features. See preface to the section 2.3$_{(40)}$ for explanation. The column "Position" contains apparent position with respect to the H I shell. Empty field (no value) means no data available.

H I shell	Counterpart	Observed	Nature	Position
GS016-09+011				
	Infrared	YES	condensations	around the central hole
			fragments	around the central hole
	Hα	YES	diffuse	around the central hole
	X-ray	NO		
	CO			
	YSOs	NO		
GS062-42+004				
	Infrared	YES	condensations	along the border
			fragments	along the border
	Hα	YES	compact	in the border
	X-ray	YES	diffuse	inside
	CO			
	YSOs	NO		

(continuing on the next page)

Table 3.2: (continued)

H I shell	Counterpart	Observed	Nature	Position
GS074-52-004				
	Infrared	YES	condensations	along the border
			filaments	along the border
	Hα	YES	diffuse	bordering
			compact	inside
	X-ray	YES	diffuse	inside
	CO	NO		
	YSOs	NO		
GS075-09-005				
	Infrared	YES	filament	along the border
	Hα	YES	condensation	inside
	X-ray	YES	condensation	inside
	CO	NO		
	YSOs	NO		
GS097-03-029				
	Infrared	YES	fragments	along the border
	Hα	YES	diffuse	penetrating inside
			condensations	outside
	X-ray	NO		
	CO	YES	fragments	along the border
	YSOs	NO		
GS116+02+006				
	Infrared	YES	condensatios	bordering
			fragments	inside, along the border
	Hα	YES	condensations	bordering, outside
	X-ray	NO		
	CO	YES	filaments	bordering
			fragments	along the border, inside
	YSOs	YES		along the border
GS133-66-013				
	Infrared	YES	condensation	along the border
			fragments	along the border
	Hα	YES	condensation	borderinging
	X-ray	YES	diffuse	inside
	CO			
	YSOs	NO		

(continuing on the next page)

Table 3.2: (continued)

H I shell	Counterpart	Observed	Nature	Position
GS134-01-028				
	Infrared	YES	condensation	in the border, outside
	Hα	YES	condensation	in the border, outside
	X-ray	NO		
	CO	YES	condensation	in the border
	YSOs	YES		in the border, outside
GS202+19-019				
	Infrared	YES	fragments	along the border
			condensations	bordering
	Hα	YES	diffuse	penetrating the shell
	X-ray	YES	diffuse	penetrating the shell
	CO			
	YSOs	NO		
GS206-17+013				
	Infrared	YES	condensations	around the border, outside
			filaments	along the border
	Hα	YES	condensation	inside
			compact	in the border
	X-ray	NO		
	CO	YES	condensation	in the border
	YSOs	YES		inside, in the border
GS218-05+031				
	Infrared	YES	condensations	along the border
			filaments	along the border
	Hα	NO	compact	around the border
			condensation	bordering
	X-ray	NO		
	CO	YES	filaments	along the border
			condensations	in the border
	YSOs	YES		along the border
GS231+38+003				
	Infrared	YES	condensations	bordering
			fragments	along the border
			diffuse	around the central hole
	Hα	YES	diffuse	pervading the border
	X-ray	YES	diffuse	inside
	CO			
	YSOs	NO		

3.2 Interpretation of Results

In all but one cases, the observed distinct H II regions are located outside the H I shells, often at their borders—see table **3.2**$_{(91)}$ and **3.1**$_{(90)}$ for a summary. Far-infrared loops and thermal dust emission have revealed a perfect correlation with H I emission, suggesting there are condensations of dust and gas at the borders of shells, potential precursors of molecular clouds and further star formation. Molecular clouds, observed via CO emission, are located predominantly at the borders of the studied H I shells.

Thus, the multiwavelength study of twelve H I shells shows that these shells are most likely connected to star-forming events. Especially, the study supports the theory of secondary star formation triggered by expanding H I shells. The star formation may be triggered either when a shock wave from an expanding shell hits some preexisting molecular cloud, or when the shell begins to gravitationally fragment as a consequence of the collect and collapse model. The collect and collapse model was originally proposed by Elmegreen & Lada (1977) for H II regions but it can act also on larger scales typical for H I shells—see Ehlerova et al. (1997).

Topologies of the studied H I shells—having generally almost fully enclosed borders—suggest that these shells were most likely created by processes connected to young massive stars rather than the interaction of high-velocity clouds with the Galactic disc.

This study can not proove or disproove the concept that H I shells are created by the same process as gamma-ray bursts. One reason is that there is no gamma-ray burst remnant described in the Milky Way. Considering the estimated gamma-ray bursts rate about 0.025 per Myr per bright galaxy (Wijers et al., 1998), it is unlikely to observe a gamma-ray burst in our galaxy during the whole span of Earth's occupation by humanity. Thus only indirect observations or statistical analysis can shed more light on the possible link between gamma-ray bursts and H I shells—their possible remnants.

Estimated energies embedded in the studied H I shells and their expansion velocities—see table table **3.1**$_{(90)}$ for a summary—also support the connection of H I shells with star formation. This implies that H I shells are most likely old relicts of previous formation of massive stars, that have inserted energy into the interstellar medium by stellar winds and supernovae explosions. H I shells can be considered as successors of expanding H II regions, as long-lasting footprints of star formation

The observed shadowing effect—background X-ray emission absorbed by foreground interstellar medium—supports the concept of the Galactic halo filled with hot gas.

Finally, I propose answers to the introductory questions:

Is it possible, with current instruments and data archives, to find counterparts of H I shells? Yes, but the surveys of the galactic neutral hydrogen covering large portions of the sky suffers from significantly lower resolution than all-sky surveys made in other wavelengths domains. For example the Leiden/Argentine/Bonn Galactic H I Survey has the angluar resolution of 0.5°, while IRAS has made images with resolution of $2'$ in the 100 μm band.

A study of H I shells based on data with higher resolution are today available only for a few shells. For example a study of the neighbourhood of the supershell GS061+00+51 by Ehlerová et al. (2001) has revealed several small expanding H I shells associates with H II regions. This suggests that there are much more expanding H I shells smaller that those already catalogued. These smaller shells are probably younger, therefore it could be possible to detect the exciting stars.

If we find some counterparts, what does they indicate about the origin of H I shells? Counterparts indicate that shells were probably created by actions of massive stars or OB associations and corresponding supernova explosions, rather than by an extreme violent event creating a gamma-ray burst.

Expansion velocities and energies of the studied twelve H I shells support this conclusion. (Based on the study of Efremov et al. (1999), showing that abrupt energy input—such as a GRB—would produce nearly static shell.)

Thus, it can be summarized that most H I shells with counterpart dust structure were created by stellar winds from OB stars in associations and their supernovae.

Are there any signs of star formation triggered by H I shells? Yes. In four cases—shells GS116+02+006, GS134-01-028, GS206-17+013 and GS218-05+031—catalogued young stellar objects were found to be apparently associated with shells. Generally, shells in most cases are negatively correlated with ionized hydrogen and in several cases, where there are CO data available, molecular condensations have been found at their borders.

Appendix A

Geometrical Relations

A.1 Haversine Formula

The relation of sides and angles of an arbitrary plane triangle is described by the *law of sines* and the *law of cosines*:

$$\frac{a}{\sin\alpha} = \frac{b}{\sin\beta} = \frac{c}{\sin\gamma}, \qquad c^2 = a^2 + b^2 - 2ab\cos\gamma, \tag{A.1}$$

where the symbols are as in the figure **A.1**(97). On a sphere, the laws take the form:

$$\frac{\sin a}{\sin\alpha} = \frac{\sin b}{\sin\beta} = \frac{\sin c}{\sin\gamma}, \qquad \cos\gamma = -\cos\alpha\cos\beta + \sin\alpha\sin\beta\cos c. \tag{A.2}$$

Assuming the spherical law of sines and consines given above, we can express the great-circle distance—$\Delta\sigma$—(the shortest distance) between two points on a sphere as

$$\Delta\sigma = \arccos\left(\sin b_1 \sin b_2 + cos b_1 cos b_2 cos\left(l_2 - l_1\right)\right), \tag{A.3}$$

where $l_1, b_1; l_2, b_2$ are the longitude and the latitude of the two points (e.g. galactic coordinates). For numerical computations, a more rounding-error robust solution is the *haversine*

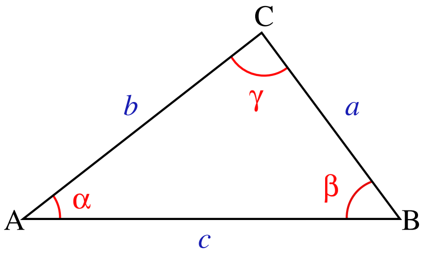

Figure A.1: Sketch of a triangle. (Wikimedia Commons, 2008; Pythagoras of Samos, c. 572–c. 490 BC) *formula*:

$$\Delta\sigma = 2 \arcsin \left(\sqrt{\sin^2 \left(\frac{b_2 - b_1}{2} \right) + \cos b_1 \cos b_2 \sin^2 \left(\frac{l_2 - l_1}{2} \right)} \right). \tag{A.4}$$

A.2 Parallax

The *parallax* is the measure of the change of angle caused by the change in relative position of the observer and the observed object. The relation between the parallax angle—p—and the distance of the observed object—d—for small angles (small for linear approximation of sine or tangent), is

$$d \text{ [pc]} = \frac{1}{p \text{ [arcsec]}}. \tag{A.5}$$

The relation of the distance error—δd—to the parallax error—δp—is

$$\delta d = \frac{\delta p}{p^2}. \tag{A.6}$$

A.3 Kinematical Distance

The relation of the kinematical distance to the radial velocity of an object can be expressed by the formula (Brand & Blitz, 1993)

$$V_{\text{lsr}} = \left(\frac{\Theta R_0}{R} - \Theta_0 \right) \sin l \cos b, \tag{A.7}$$

where V_{lsr} is the radial velocity of the object relative to the local standard of rest[1], Θ is the circular velocity of the object, R is the galactocentric distance of the object, Θ_0 is the circular velocity at the position of the Sun, R_0 is the galactocentric distance of the Sun, l is the galactic longitude, b is the galactic latitude.

The galactocentric distance of an object can be expressed—considering projection to the galactic plane and the law of sines (equation A.1$_{(97)}$)—by the formula

$$R = \left(d^2 \cos^2 b + R_0^2 - 2 R_0 d \cos b \cos l \right)^{1/2}, \tag{A.8}$$

where d is the heliocentric distance of the object.

Combining these equations (A.7$_{(98)}$ and A.8$_{(98)}$) and assuming the simple rotation ($\Theta = \Theta_0$), we can express the kinematical distance of an object by the formula

$$d_{1,2} = \frac{R_0}{\cos b} \left(\cos l \pm \sin l \sqrt{-1 + \left(\frac{\Theta_0 \cos b}{V_{\text{lsr}} + \Theta_0 \sin l \cos b} \right)^2} \right). \tag{A.9}$$

---

[1] local standard of rest (kinematical) = a point in the vicinity of the Sun with the circular velocity

Appendix B

Reprojection and Mosaicking

Because all multiwavelength images presented in this paper—especially in section 2.3$_{(40)}$—are in *equirectangular projection* with the galactic coordinates, reprojection of some original images was needed—see section 2.1$_{(21)}$.

The equirectangular projection—also called *plate carrée*—is a projection of a general two-dimensional surface from three dimensions to plane. When using the galactic coordinates, it is described by a simple affine transformation:

$$x = \mathrm{A}l + \mathrm{B}, \qquad y = \mathrm{C}b + \mathrm{D}, \tag{B.1}$$

where l, b are the galactic longitude and the galactic latitude; x, y are pixel coordinates and A, B, C, D are chosen constants. In this paper, B and D are zero. This means that centers of images correspond to the center of the Galaxy. Constants A and B scale the image.

The program Montage[1]was used for reprojection and mosaicking. The used FITS[2] header template is shown below. See papers of Greisen & Calabretta (2002); Calabretta & Greisen (2002) for detailed description of coordinates representations if FITS files. Note that the number of image pixels defined in the template (3601 × 1801) is derived from the size of the spatial part of the data cube from the Leiden/Argentine/Bonn Galactic H I Survey (721 × 361)—see section 2.1.1$_{(21)}$.

---

[1] Website: http://montage.ipac.caltech.edu/

[2] FITS = **F**lexible **I**mage **T**ransport **S**ystem—a digital file format used to store, transmit and manipulate scientific images. See website http://fits.gsfc.nasa.gov/.

FITS header template for the program Montage:

```
SIMPLE  = T
BITPIX  = -32
NAXIS   = 2
NAXIS1  = 3601
NAXIS2  = 1801
CTYPE1  = 'GLON-CAR'
CTYPE2  = 'GLAT-CAR'
CRVAL1  =    0.000000000
CRVAL2  =    0.000000000
CDELT1  =   -0.100000000
CDELT2  =    0.100000000
CRPIX1  =  1801
CRPIX2  =   901
CROTA2  =    0.000000000
END
```

Appendix C

Repaired FITS Headers

The FITS files from the data release "12' Maps of the Soft X-ray Diffuse Background" by Snowden et al. (1997)—see section 2.1.5(27)—contain wrong astrometric records in their headers. All files, even though each covers a different part of the sky, contain the same astrometric header records:

```
...
CRVAL1 =       0
CRPIX1 = 256.500
...
CRVAL2 =      90
CRPIX2 = 256.500
...
```

Repaired records for all files from the second band are given below.

```
g000m90r2b120pm.fits
  CRVAL1 =       0
  CRPIX1 = 256.500
  CRVAL2 =     -90
  CRPIX2 = 256.500

g000p00r2b120pm.fits
  CRVAL1 =       0
  CRPIX1 = 256.500
  CRVAL2 =       0
  CRPIX2 = 256.500

g000p90r2b120pm.fits
  CRVAL1 =       0
  CRPIX1 = 256.500
  CRVAL2 =      90
  CRPIX2 = 256.500
```

```
g090p00r2b120pm.fits
  CRVAL1 =      90
  CRPIX1 = 256.500
  CRVAL2 =       0
  CRPIX2 = 256.500
```

```
g180p00r2b120pm.fits
  CRVAL1 =     180
  CRPIX1 = 256.500
  CRVAL2 =       0
  CRPIX2 = 256.500
```

```
g270p00r2b120pm.fits
  CRVAL1 =     270
  CRPIX1 = 256.500
  CRVAL2 =       0
  CRPIX2 = 256.500
```

Appendix D

List of Physical Constants

Fundamental Constants

The following list of fundamental physical constants (table **D.1**$_{(103)}$) is a subset of the list published by Mohr et al. (2007).

Table D.1: List of fundamental physical constants.

Quantity	Symbol	Numerical value	Unit
speed of light in vacuum	c	$299\,792\,458$	$\mathrm{m\,s^{-1}}$
magnetic constant	μ_0	$4\pi \times 10^{-7}$	$\mathrm{N\,A^{-2}}$
		$= 12.566\,370\,614\ldots \times 10^{-7}$	$\mathrm{N\,A^{-2}}$
electric constant $1/(\mu_0 c^2)$	ε_0	$8.854\,187\,817\ldots \times 10^{-12}$	$\mathrm{F\,m^{-1}}$
Newtonian constant of gravitation	G	$6.674\,28(67) \times 10^{-11}$	$\mathrm{m^3\,kg^{-1}\,s^{-2}}$
Planck constant	h	$6.626\,068\,96(33) \times 10^{-34}$	$\mathrm{J\,s}$
$h/2\pi$	$\hbar$	$1.054\,571\,628(53) \times 10^{-34}$	$\mathrm{J\,s}$
elementary charge	e	$1.602\,176\,487(40) \times 10^{-19}$	C
electron mass	m_e	$9.109\,382\,15(45) \times 10^{-31}$	kg
proton mass	m_p	$1.672\,621\,637(83) \times 10^{-27}$	kg
proton-electron mass ratio	$m_\mathrm{p}/m_\mathrm{e}$	$1836.152\,672\,47(80)$	
Avogadro constant	N_A, L	$6.022\,141\,79(30) \times 10^{23}$	$\mathrm{mol^{-1}}$
molar gas constant	R	$8.314\,472(15)$	$\mathrm{J\,mol^{-1}\,K^{-1}}$
Boltzmann constant R/N_A	k	$1.380\,6504(24) \times 10^{-23}$	$\mathrm{J\,K^{-1}}$
electron volt: (e/C) J	eV	$1.602\,176\,487(40) \times 10^{-19}$	J
Stefan-Boltzmann constant $(\pi^2/60)k^4/(\hbar^3 c^2)$	σ	$5.670\,400(40) \times 10^{-8}$	$\mathrm{W\,m^{-2}\,K^{-4}}$

Astronomical Constants and Units

The following list of astronomical constants (table **D.2**$_{(104)}$) and units is adopted from IAU (1987).

Table D.2: List of astronomical constants and units.

Quantity	Symbol	Numerical value	Unit
astronomical unit	au	0.149 598	Tm
parsec	pc	30.857	Pm
solar mass	$M_\odot$	1.9891×10^{30}	kg
jansky	Jy	10^{-26}	$\mathrm{W\,m^{-2}\,Hz^{-1}}$
erg	erg	10^{-7}	J

References

Arnal, E. M., Bajaja, E., Larrarte, J. J., Morras, R., & Pöppel, W. G. L. 2000, A&AS, 142, 35

Bajaja, E., Arnal, E. M., Larrarte, J. J., Morras, R., Pöppel, W. G. L., & Kalberla, P. M. W. 2005, A&A, 440, 767

Bernard, J. P., Boulanger, F., Desert, F. X., Giard, M., Helou, G., & Puget, J. L. 1994, A&A, 291, L5

Blair, W. P., Sankrit, R., Raymond, J. C., & Long, K. S. 1999, AJ, 118, 942

Bodenheimer, P., Yorke, H. W., & Tenorio-Tagle, G. 1984, A&A, 138, 215

Bonnarel, F., Fernique, P., Bienaymé, O., Egret, D., Genova, F., Louys, M., Ochsenbein, F., Wenger, M., & Bartlett, J. G. 2000, A&AS, 143, 33

Bonnor, W. B. 1957, MNRAS, 117, 104

Boulanger, F. 1999, in Astronomical Society of the Pacific Conference Series, Vol. 168, New Perspectives on the Interstellar Medium, ed. A. R. Taylor, T. L. Landecker, & G. Joncas, 173–+

Boulanger, F., Abergel, A., Bernard, J.-P., Burton, W. B., Desert, F.-X., Hartmann, D., Lagache, G., & Puget, J.-L. 1996a, A&A, 312, 256

Boulanger, F., Reach, W. T., Abergel, A., Bernard, J. P., Cesarsky, C. J., Cesarsky, D., Desert, F. X., Falgarone, E., Lequeux, J., Metcalfe, L., Perault, M., Puget, J. L., Rouan, D., Sauvage, M., Tran, D., & Vigroux, L. 1996b, A&A, 315, L325

Brand, J., & Blitz, L. 1993, A&A, 275, 67

Burningham, B., Naylor, T., Littlefair, S. P., & Jeffries, R. D. 2005, MNRAS, 356, 1583

Calabretta, M. R., & Greisen, E. W. 2002, A&A, 395, 1077

Chevalier, R. A. 1974, ApJ, 188, 501

Cox, D. P., & Reynolds, R. J. 1987, ARA&A, 25, 303

Daigle, A., Joncas, G., Parizeau, M., & Miville-Deschênes, M.-A. 2003, PASP, 115, 662

Dale, J. E., Bonnell, I. A., & Whitworth, A. P. 2007, MNRAS, 375, 1291

Dame, T. M., Hartmann, D., & Thaddeus, P. 2001, ApJ, 547, 792

de Boer, K. S. 2007, Physics and The Interstellar Medium—Lecture Notes (Argelander Institut für Astronomie of the Universität Bonn)

Deharveng, L., Zavagno, A., Lefloch, B., Caplan, J., & Pomarès, M. 2007, in IAU Symposium, Vol. 237, IAU Symposium, ed. B. G. Elmegreen & J. Palouš, 212–216

Efremov, Y. N., Ehlerová, S., & Palouš, J. 1999, A&A, 350, 457

Efremov, Y. N., Elmegreen, B. G., & Hodge, P. W. 1998, ApJ, 501, L163+

Ehlerova, S., Palous, J., Theis, C., & Hensler, G. 1997, A&A, 328, 121

Ehlerová, S., & Palouš, J. 1996, A&A, 313, 478

—. 2002, MNRAS, 330, 1022

—. 2005, A&A, 437, 101

Ehlerová, S., Palouš, J., & Huchtmeier, W. K. 2001, A&A, 374, 682

Eisenhauer, F., Genzel, R., Alexander, T., Abuter, R., Paumard, T., Ott, T., Gilbert, A., Gillessen, S., Horrobin, M., Trippe, S., Bonnet, H., Dumas, C., Hubin, N., Kaufer, A., Kissler-Patig, M., Monnet, G., Ströbele, S., Szeifert, T., Eckart, A., Schödel, R., & Zucker, S. 2005, ApJ, 628, 246

Eisenhauer, F., Schödel, R., Genzel, R., Ott, T., Tecza, M., Abuter, R., Eckart, A., & Alexander, T. 2003, ApJ, 597, L121

Elmegreen, B. G. 1994, ApJ, 427, 384

Elmegreen, B. G. 1998, in Astronomical Society of the Pacific Conference Series, Vol. 148, Origins, ed. C. E. Woodward, J. M. Shull, & H. A. Thronson, Jr., 150–+

Elmegreen, B. G., & Lada, C. J. 1977, ApJ, 214, 725

Ewen, H. I., & Purcell, E. M. 1951, Nature, 168, 356

Finkbeiner, D. P. 2003, ApJS, 146, 407

Fomalont, E. B., & Weliachew, L. 1973, ApJ, 181, 781

Forbrich, J., Schreyer, K., Posselt, B., Klein, R., & Henning, T. 2004, ApJ, 602, 843

Frail, D. A., Kulkarni, S. R., Sari, R., Djorgovski, S. G., Bloom, J. S., Galama, T. J., Reichart, D. E., Berger, E., Harrison, F. A., Price, P. A., Yost, S. A., Diercks, A., Goodrich, R. W., & Chaffee, F. 2001, ApJ, 562, L55

Gaustad, J. E., McCullough, P. R., Rosing, W., & Van Buren, D. 2001, PASP, 113, 1326

Giard, M., Lamarre, J. M., Pajot, F., & Serra, G. 1994, A&A, 286, 203

Giovanelli, R. 1980, ApJ, 238, 554

Greisen, E. W., & Calabretta, M. R. 2002, A&A, 395, 1061

Hachisuka, K., Brunthaler, A., Menten, K. M., Reid, M. J., Imai, H., Hagiwara, Y., Miyoshi, M., Horiuchi, S., & Sasao, T. 2006, ApJ, 645, 337

Haffner, L. M., Reynolds, R. J., Tufte, S. L., Madsen, G. J., Jaehnig, K. P., & Percival, J. W. 2003, ApJS, 149, 405

Haislip, J. B., Nysewander, M. C., Reichart, D. E., Levan, A., Tanvir, N., Cenko, S. B., Fox, D. B., Price, P. A., Castro-Tirado, A. J., Gorosabel, J., Evans, C. R., Figueredo, E., MacLeod, C. L., Kirschbrown, J. R., Jelinek, M., Guziy, S., Postigo, A. D. U., Cypriano, E. S., Lacluyze, A., Graham, J., Priddey, R., Chapman, R., Rhoads, J., Fruchter, A. S., Lamb, D. Q., Kouveliotou, C., Wijers, R. A. M. J., Bayliss, M. B., Schmidt, B. P., Soderberg, A. M., Kulkarni, S. R., Harrison, F. A., Moon, D. S., Gal-Yam, A., Kasliwal, M. M., Hudec, R., Vitek, S., Kubanek, P., Crain, J. A., Foster, A. C., Clemens, J. C., Bartelme, J. W., Canterna, R., Hartmann, D. H., Henden, A. A., Klose, S., Park, H.-S., Williams, G. G., Rol, E., O'Brien, P., Bersier, D., Prada, F., Pizarro, S., Maturana, D., Ugarte, P., Alvarez, A., Fernandez, A. J. M., Jarvis, M. J., Moles, M., Alfaro, E., Ivarsen, K. M., Kumar, N. D., Mack, C. E., Zdarowicz, C. M., Gehrels, N., Barthelmy, S., & Burrows, D. N. 2006, Nature, 440, 181

Hartmann, D., & Burton, W. B. 1997, Atlas of Galactic Neutral Hydrogen (Atlas of Galactic Neutral Hydrogen, by Dap Hartmann and W. Butler Burton, pp. 243. ISBN 0521471117. Cambridge, UK: Cambridge University Press, February 1997.)

Heiles, C. 1976, ApJ, 208, L137

—. 1979, ApJ, 229, 533

—. 1984, ApJS, 55, 585

Hosokawa, T., & Inutsuka, S.-i. 2005, ApJ, 623, 917

—. 2006, ApJ, 646, 240

—. 2007, ApJ, 664, 363

Hu, E. M. 1981, ApJ, 248, 119

Hulsbosch, A. N. M. 1975, A&A, 40, 1

Hulsbosch, A. N. M., & Raimond, E. 1966, Bull. Astron. Inst. Netherlands, 18, 413

IAU. 1987, Recommendations concerning Units, [Online; accessed 13-April-2008]

Joye, W. A., & Mandel, E. 2003, in Astronomical Society of the Pacific Conference Series, Vol. 295, Astronomical Data Analysis Software and Systems XII, ed. H. E. Payne, R. I. Jedrzejewski, & R. N. Hook, 489–+

Kalberla, P. M. W., Burton, W. B., Hartmann, D., Arnal, E. M., Bajaja, E., Morras, R., & Pöppel, W. G. L. 2005, A&A, 440, 775

Karr, J. L., & Martin, P. G. 2003, ApJ, 595, 900

Katgert, P. 1969, A&A, 1, 54

Kenyon, M. J., Jeffries, R. D., Naylor, T., Oliveira, J. M., & Maxted, P. F. L. 2005, MNRAS, 356, 89

Kiss, C., Moór, A., & Tóth, L. V. 2004, A&A, 418, 131

Klebesadel, R. W., Strong, I. B., & Olson, R. A. 1973, ApJ, 182, L85+

Könyves, V., Kiss, C., Moór, A., Kiss, Z. T., & Tóth, L. V. 2007, A&A, 463, 1227

Lada, C. J., Elmegreen, B. G., Cong, H.-I., & Thaddeus, P. 1978, ApJ, 226, L39

Lamb, D. Q. 1995, PASP, 107, 1152

Loeb, A., & Perna, R. 1998, ApJ, 503, L35+

Maheswar, G., Sharma, S., Biman, J. M., Pandey, A. K., & Bhatt, H. C. 2007, MNRAS, 379, 1237

Menten, K. M., Reid, M. J., Forbrich, J., & Brunthaler, A. 2007, A&A, 474, 515

Merrifield, M. R. 1992, AJ, 103, 1552

Metzger, M. R., Caldwell, J. A. R., & Schechter, P. L. 1998, AJ, 115, 635

Minkowski, R. 1958, Reviews of Modern Physics, 30, 1048

Miville-Deschênes, M.-A., & Lagache, G. 2005, ApJS, 157, 302

Mohr, P. J., Taylor, B. N., & Newell, D. B. 2007, CODATA Recommended Values of the Fundamental Physical Constants: 2006, Tech. rep., National Institute of Standard and Technology, USA

Muller, C. A., & Oort, J. H. 1951, Nature, 168, 357

Muzerolle, J., Hillenbrand, L., Calvet, N., Briceño, C., & Hartmann, L. 2003, ApJ, 592, 266

Paczynski, B. 1995, PASP, 107, 1167

Palouš, J., & Ehlerová, S. 2002, in Revista Mexicana de Astronomia y Astrofisica Conference Series, Vol. 12, Revista Mexicana de Astronomia y Astrofisica Conference Series, ed. W. J. Henney, J. Franco, & M. Martos, 35–36

Palouš, J. 2008, [palous@ig.cas.cz]

Perryman, M. A. C., Lindegren, L., Kovalevsky, J., Hoeg, E., Bastian, U., Bernacca, P. L., Crézé, M., Donati, F., Grenon, M., van Leeuwen, F., van der Marel, H., Mignard, F., Murray, C. A., Le Poole, R. S., Schrijver, H., Turon, C., Arenou, F., Froeschlé, M., & Petersen, C. S. 1997, A&A, 323, L49

Pythagoras of Samos. c. 572–c. 490 BC, The Triangle

Reid, M. J. 1993, ARA&A, 31, 345

Sauvage, M. 1997, in Astrophysics and Space Science Library, Vol. 161, Astrophysics and Space Science Library, 1–31

Shapiro, P. R., & Field, G. B. 1976, ApJ, 205, 762

Snowden, S. L., Egger, R., Freyberg, M. J., McCammon, D., Plucinsky, P. P., Sanders, W. T., Schmitt, J. H. M. M., Truemper, J., & Voges, W. 1997, ApJ, 485, 125

Stanimirovic, S., Staveley-Smith, L., Dickey, J. M., Sault, R. J., & Snowden, S. L. 1999, MNRAS, 302, 417

Tenorio-Tagle, G. 1980, A&A, 88, 61

—. 1981, A&A, 94, 338

Tenorio-Tagle, G., & Bodenheimer, P. 1988, ARA&A, 26, 145

Tenorio-Tagle, G., Bodenheimer, P., Rozyczka, M., & Franco, J. 1986, A&A, 170, 107

Tenorio-Tagle, G., Franco, J., Bodenheimer, P., & Rozyczka, M. 1987, A&A, 179, 219

Thilker, D. A., Braun, R., & Walterbos, R. M. 1998, A&A, 332, 429

Verschuur, G. L. 1975, ARA&A, 13, 257

Walter, F., & Brinks, E. 1999, AJ, 118, 273

Waxman, E. 1997, ApJ, 489, L33+

Whitworth, A. P., Bhattal, A. S., Chapman, S. J., Disney, M. J., & Turner, J. A. 1994, MNRAS, 268, 291

Wijers, R. A. M. J., Bloom, J. S., Bagla, J. S., & Natarajan, P. 1998, MNRAS, 294, L13

Wikimedia Commons. 2008, Image:Triangle with notations 2.svg, [Online; accessed 31-March-2008]

Williams, J. P., & Maddalena, R. J. 1996, ApJ, 464, 247

Wouterloot, J. G. A., Brand, J., & Fiegle, K. 1993, A&AS, 98, 589

Xu, Y., Reid, M. J., Zheng, X. W., & Menten, K. M. 2006, Science, 311, 54

Zapatero Osorio, M. R., Béjar, V. J. S., Pavlenko, Y., Rebolo, R., Allende Prieto, C., Martín, E. L., & García López, R. J. 2002, A&A, 384, 937

Zavagno, A., Pomarès, M., Deharveng, L., Hosokawa, T., Russeil, D., & Caplan, J. 2007, A&A, 472, 835

Index

This research has made use of the following software:

Linux

Mandriva Linux

Kubuntu

GIMP

gnuplot

Montage

This research has made use of NASA's Astrophysics Data System.

This research has made use of Montage, funded by the National Aeronautics and Space Administration's Earth Science Technology Office, Computation Technologies Project, under Cooperative Agreement Number NCC5-626 between NASA and the California Institute of Technology. Montage is maintained by the NASA/IPAC Infrared Science Archive.

This research has made use of the SIMBAD database, operated at CDS, Strasbourg, France.

This research has made use of Aladin (Bonnarel et al., 2000).

This research has made use of SAOImage DS9, developed by Smithsonian Astrophysical Observatory (Joye & Mandel, 2003).

This document was typeset with $\TeX/\LaTeX\,2_{\varepsilon}$.

Date of compilation: April 16, 2008.